DISS. ETH NO. 20467

Transport properties of three-terminal graphene devices

A dissertation submitted to

ETH ZÜRICH

for the degree of

Doctor of Sciences

presented by

ARNHILD JACOBSEN

Master of Science,
Norwegian University of Science and Technology,
2008

born on March 4th, 1983

citizen of Norway

accepted on the recommendation of

Prof. Dr. Klaus Ensslin, examiner
Prof. Dr. Wendelin Stark, co-examiner
Prof. Dr. Thomas Ihn, co-examiner

2012

Summary

Theoretically, graphene, a two-dimensional carbon crystal, has been known for a long time. However, its predicted fascinating electronic properties could not be measured before 2004 when high quality graphene was deposited on an isolating substrate for the first time. In the following years this intriguing material, which also has impressing mechanical and thermal properties, has attracted a lot of interest among scientists from different fields including physics, chemistry, mechanical engineering and electrical engineering.

In this thesis we present transport experiments on different graphene nanostructures from cryogenic temperatures up to room temperature. All structures are made by the conventional technology where single layer graphene flakes are first deposited onto a Si/SiO_2 substrate and afterwards etched into the desired structure.

The experimental part of the thesis is divided into three parts. In the first part we present transport properties of graphene devices chemically modified by diazonium chemistry. In the second part different transport properties of a three-terminal graphene junction are investigated and in the third part a three-terminal quantum dot in the Coulomb blockaded transport regime is studied.

Part I

Chemical functionalization of graphene modifies the local carbon-carbon bond structure and thus the electronic properties of graphene. Measuring these changes allow for a better understanding of the influence of functionalization on the graphene lattice. However, not only chemistry, in this case diazonium chemistry, has an effect on electronic transport in graphene. The latter is also influenced by defects and dopants resulting from the different processing steps. Here we show that solvents used in the chemical reaction process additionally influence the electronic properties of graphene and that these effects might be difficult to distinguish from the effect of the chemical functionalization itself. In more detail, we treat the graphene devices with isopropanol and observe an increased amount of p-dopants and an asymmetry between electron and hole transport. These two effects are similar to the observed effects of functionalization when only few defects are created. We therefore develop an experimental procedure, based on a combination of isopropanol treatment and heating, that allows us to control the influence of solvents on electronic transport.

In further experiments we present detailed Raman spectroscopy and electronic transport measurements of step-wise functionalized graphene Hall bars. The functionalization results in a strong p-doping of the graphene samples, but only slightly lower mobilities. By comparing Raman and transport data after each functionalization step, we conclude that two preferential reactions take place on the graphene surface. In the beginning a few nitrobenzene molecules are directly attached to the graphene lattice, thus creating defects. Afterwards these act as seeds for a polymer like growth not directly connected to the graphene lattice.

Part II

Due to its high charge carrier mobilities graphene is a promising material for ballistic electronics. One class of novel graphene-based devices with potential for applications is ballistic switches and rectifiers that can operate at ultrahigh frequencies. Here we present measurements of the nonlinear electrical properties of a graphene three-terminal junction. We apply a bias voltage in a symmetric push-pull fashion with $V_{\mathrm{L}} = V_0$ and $\mathrm{V_L}$=-V_0, where V_{L} is the bias voltage applied to the left branch and V_{R} is the bias voltage applied to the right branch, and the voltage at the center branch V_{C} is measured. The central branch voltage V_{C} is shown to exhibit nonlinear rectifying behavior as a function of the applied bias voltage $\mathrm{V_0}$ and the sign and the efficiency of the rectification can be tuned by a gate. As a general trend V_{C} bends "down" as a function of V_0 in the regime of electron transport, and bends "up" in the regime of hole transport. This trend is observed from 4.2 K up to room temperature. At 4.2 K we observe in addition switching events between bending "up" and bending "down" behavior for $V_0 < 10\,\mathrm{mV}$. This we attribute to universal conductance fluctuations.

Furthermore this device is used to study phase-coherent transport in graphene. The gate voltage and temperature dependence of both the weak localization effect and universal conductance fluctuations are investigated. The resistivity peak attributed to the weak localization effect is found to broaden and decrease in amplitude with increasing temperature, corresponding to the expected decrease in the phase coherence length of the charge carriers for increasing temperature. In addition a possible transition form weak localization to weak antilocalization is observed for high temperatures and low charge carrier densities. The amplitude of the universal conductance fluctuations decreases exponential with increasing temperature and no gate dependence of the amplitude is observed.

Finally, we use this special three-terminal structure to qualitatively probe the disorder potential of bulk graphene. Here we find the disorder potential due to electron and hole puddles to be on the order of 100 meV and the size of single puddles to be between 50 and 60 nm.

Part III

The conductance through a standard two-terminal quantum dot is determined by the average coupling of the dot wave function with the wave functions of both leads. Thus, the individual coupling strengths between the dot and each lead cannot be accessed by such an experiment. However, if the quantum dot is connected to three or more leads the individual coupling strengths between the dot and each lead can be determined from measurements of the complete conductance matrix of the system. Here we present measurements of a three-terminal graphene quantum dot in the multilevel transport regime. All nine elements of the conductance matrix are independently measured and the individual conductances of each lead are determined. Surprisingly, accurate measurements of single conductance resonances in the Coulomb blockaded regime reveal slightly different resonance energies depending on which pair of leads is used for probing. We show that this effect is due to different single particle dot levels that couple with different strengths to the three leads. Thus, these measurements give qualitatively insight into the spatial distribution of the quantum dot wave functions and are an important step towards a better understanding of the internal energy level structure of graphene quantum dots.

Finite bias spectroscopy measurements of the three-terminal quantum dot reveal regular Coulomb diamonds with pronounced lines of enhanced differential conductance parallel to the edges of the diamonds outside the Coulomb blockaded regime. These features are partly aligned with features of enhanced differential conductance inside the diamonds. We speculate that both these features originates either from transport through excited states or from a modulation of the density of states in the leads or from a combination of both.

Zusammenfassung

Graphen, ein zweidimensionaler Kristall aus Kohlenstoff, ist in der Theorie seit langem bekannt. Dennoch konnten die vorhergesagten erstaunlichen elektronischen Eigenschaften erst 2004 gemessen werden, als hochwertiges Graphen erstmals auf einem nichtleitenden Substrat isoliert werden konnte. In den darauffolgenden Jahren hat dieses faszinierende Material, das zusätzlich auch beeindruckende mechanische und thermische Eigenschaften aufweist, das Interesse von Wissenschaftlern in verschiedensten Bereichen geweckt. Darunter sind Physik, Chemie, Maschinenbau sowie Elektroingenieurwesen.

In der vorliegenden Arbeit präsentieren wir Transportexperimente mit verschiedenen Nanostrukturen aus Graphen gemessen im Bereich kryogenischer bis hin zu Raumtemperaturen. Wie allgemein üblich wurden für sämtliche Proben die Graphenflakes zunächst auf Si/SiO_2-Substrat aufgebracht und dann in die gewünschte Struktur geätzt.

Der experimentelle Teil dieser Arbeit ist in drei Teile geteilt. Im ersten Teil zeigen wir Transporteigenschaften von Graphenproben die mittels Diazonium-Gruppen chemisch modifiziert wurden. Im zweiten Teil werden die elektronischen Charakteristika von Drei-Terminal-Gabelungen gemessen und im dritten Teil wird ein Drei-Terminal-Quantenpunkt im Regime der Coulombblockade untersucht.

Teil I

Chemische Funktionalisierung verändert lokal die Bindungsstruktur zwischen den Kohlenstoffatomen und damit auch die elektrischen Eigenschaften von Graphen. Durch Messungen dieser Veränderungen gewinnt man ein besseres Verständnis der Auswirkung der Funktionalisierung auf das Graphengitter. Jedoch beinflusst nicht nur die Chemie, hier Diazonium-Chemie, den elektrischen Transport in Graphen. Dieser wird auch durch Defekte und Dotierung, die während der Prozessierung eingebracht werden, verändert. Wir zeigen, dass Lösungsmittel, die während der chemischen Reaktion zum Einsatz kommen, die elektrischen Eigenschaften zusätzlich beeinflussen und dass es schwierig ist, diese Effekte von der eigentlichen Funktionalisierung zu unterscheiden. Wir behandeln die Proben mit Isopropanol und beobachten sowohl eine erhöhte p-Dotierung als auch eine Asymmetrie zwischen dem Transport im Elektronen- und Löcherbereich. Diese sind vergleichbar mit den Effekten, die durch das Einbringen weniger Defekte bei einer Funktionalisierung, erzeugt werden. Deshalb haben wir ein experimentelles Vorgehen entwickelt, bei welchem wir Isopropanolbehandlung und Ausheizen abwechseln. Dies erlaubt uns den Einfluss von Lösungsmitteln auf den elektrischen Transport zu kontrollieren.

In weiteren Versuchen präsentieren wir detaillierte Ramanspektroskopiestudien und Transportmessungen an schrittweise funktionalisierten Graphen-Hallbars. Die Funktionalisierung führt zu einer starken p-Dotierung der Graphenproben, aber nur zu einer kaum niedrigeren Ladungsträgermobilität. Aus dem Vergleich der Raman- und Transportdaten nach jedem Funktionalsierungsschritt schliessen wir, dass vorrangig zwei Reaktionen an der Graphenoberfläche stattfinden. Zu Beginn lagern sich einige Nitrobenzolmoleküle direkt an das Graphengitter wodurch Defekte eingebracht werden. Anschliessend wirken diese als Keime für ein polymerartiges Wachstum das nicht direkt an den Graphenatomen stattfindet.

Teil II

Aufgrund seiner hohen Ladungsträgermobilität ist Graphen ein vielversprechendes Material für ballistische Elektronik. Eine Gruppe von neuartigen Bauteilen aus Graphen, die Potential zur Anwendung haben, sind ballistische Schalter und Gleichrichter, die bei ultrahohen Frequenzen betrieben werden können. In diesem Teil der Arbeit zeigen wir Messungen der nichtlinearen elektrischen Eigenschaften einer Drei-Terminal-Gabelung. Wir legen eine Vorspannung nach dem "Drück-Zieh"-Verfahren mit $V_{\mathrm{L}} = V_0$ und $V_{\mathrm{R}} = -V_0$ an, wobei V_{L} die Vorspannung am linken Arm und V_{R} die Vorspannung am rechten Arm ist. Die Spannung am mittleren Arm V_{C} wird gemessen. Diese Spannung V_{C} weist in Abhängigkeit der angelegeten Vorspannung V_0 ein nichtlineares Gleichrichterverhalten auf. Das Vorzeichen und die Effizienz dieser Gleichrichtung können durch ein Gate abgestimmt werden. Als Funktion von V_0 neigt die Spannung V_{C} für den Elektronenbereich im Allgemeinen nach unten und für den Löcherbereich nach oben ab. Dieses Verhalten ist von 4.2 K bis Raumtemperatur zu beobachten. Zusätzlich beobachten wir, dass das Signal für V_0 <10 mV zwischen aufwärts- und abwärtsbiegend hin- und herschaltet. Dies führen wir auf Leitwertfluktuationen zurück.

Ausserdem verwenden wir diese Probe um phasenkohärenten Transport in Graphen zu untersuchen. Sowohl die Spannungs- als auch die Temperaturabhängigkeit der schwachen Lokalisierung und der Leitwertfluktuationen werden gemessen. Der Widerstandspeak der schwachen Lokalisierung wird mit zunehmender Temperatur breiter und schrumpft, was mit der abnehmenden Kohärenzlänge der Ladungsträger bei erhöhter Temperatur zusammenhängt. Zusätzlich beobachten wir bei tiefen Temperaturen und niedrigen Ladungsträgerdichten möglicherweise einen Übergang von schwacher Lokalisierung zu schwacher Antilokalisierung. Die Amplitude der Leitwertfluktuationen nimmt exponentiell mit der Temperatur ab und wir sehen keine Gateabhängigkeit der Amplitude.

Schliesslich verwenden wir diese aussergewöhnliche Drei-Terminal-Struktur, um das Unordnungspotential in Graphen qualitativ zu messen. Wir erhalten für das Unordnungspotential aufgrund von Elektron-Loch-Puddles etwa 100 meV und für die Grösse der einzelnen Puddles Werte zwischen 50 und 60 nm.

Teil III

Der Leitwert eines herkömmlichen Zwei-Terminal-Quantenpunkts ist durch die mittlere Kopplung der Quantenpunktwellenfunktion zu den Wellenfunktionen beider Zuleitungen gegeben. Daher können die einzelnen Kopplungsstärken zwischen dem Quantenpunkt und jeder einzelnen Zuleitung in solch einem Experiment nicht ermittelt werden. Jedoch können die einzelnen Kopplungsstärken in einem Quantenpunkt, der drei oder mehr Zuleitungen besitzt, über die Messung der kompletten Leitwertmatrix des Systems bestimmt werden. Hier präsentieren wir Messungen an einem Drei-Terminal-Quantenpunkt im Multileveltransportregime. Alle neun Elemente der Leitwertmatrix wurden einzeln gemessen und der Leitwert jeder einzelnen Zuleitung wurde bestimmt. Überraschenderweise zeigen sorgfältige Messungen einzelner Leitwertresonanzen im Coulombblockaderegime, dass die Resonanzen bei leicht unterschiedlichen Energiewerten sitzen, abhängig davon, welches Zuleitungspaar zur Messung verwendet wird. Wir zeigen, dass dieser Effekt auf verschiedene Energieniveaus des Anregunsspektrums im Quantenpunkt zurückzuführen ist, die unterschiedlich stark zu den drei Zuleitungen koppeln. Daher geben diese Messungen einen qualitativen Einblick in die laterale Verteilung der Wellenfunktionen im Quantenpunkt und sind ein wichtiger Schritt zu einem besseren Verständnis der Anordnung der Energieniveaus in Graphenquantenpunkten.

Messungen des Drei-Terminal-Quantenpunkts als Funktion der Vorspannung, zeigen gleichmässige Coulombdiamanten mit ausgeprägten Linien erhöhten differentiellen Leitwerts parallel zur Kante der Diamanten ausserhalb der Coulomblockade. Diese Strukturen grenzen teilweise an Linien erhöhten differentiellen Leitwerts innerhalb der Diamanten. Wir vermuten, dass beide Strukturen vom Transport durch angeregte Zustände oder von einer veränderten Zustandsdichte in den Zuleitungen oder einer Kombination dieser

beiden Effekte verursacht werden.

Contents

Lists of symbols

physical constants	explanation
-e<0	electron charge
ϵ	dielectric permittivity
ϵ_o	vacuum dielectric constant
$h = 2\pi\hbar$	Planck's constant
k_B	Boltzmann constant

Abbreviation	Explanation
2DEG	two dimensional electron gas
AC	alternating current
BG	backgate
CNP	Charge neutrality point
DC	direct current
DOS	density of states
ebl	Electron beam lithography
FIRST	frontiers in research, space and time or simply our clean room
FWHM	full width at half maximum
LL	Landau level
NBD	4-nitrobenzene-diazonium-tetrafluorborate
PG	plungergate
PMMA	Poly(methyl methacrylate)
QD	quantum dot
SdH	Shubnikov de Haas
SFM	scanning force microscope
UCF	Universal conductance fluctuations
WL	Weak localization
WAL	Weak antilocalization

Symbol	Explanation
L,W	system size (length, width)
B	magnetic field
E_{C}	constant interaction energy
α_{G}	gate lever arm
ε_N	single particle energy of the Nth level
Δ_N	single particle level spacing
E_{F}	Fermi energy
Q	charge
I	current
V	voltage
G	conductance
ρ	resistance
Γ	tunnel coupling
v_{F}	Fermi velocity
k_{F}	Fermi wavenumber
λ_{F}	Fermi wavelength
ℓ_e	elastic mean free path
ℓ_Φ	phase coherence length
τ_{tr}	transport scattering time
τ_q	quantum life time
μ_e	electron mobility
μ_h	hole mobility
ν	filling factor
ω_c	cyclotron frequency
r_c	cyclotron radius
T	temperature
n	charge carrier density

Background

Chapter 1

Introduction

Carbon is one of the most common elements on earth. One of its most frequent allotropes, graphite, has been known and used for thousands of years. It consist of planes of carbon-atoms arranged in a honeycomb structure that are weakly bonded together. To isolate one of these sheets of carbon atoms and keeping it from rolling itself up was for a long time considered impossible [1]. However, in 2004 researches from the University of Manchester, A. Geim and K. Novoselov, achived exactly this [2]. They used a surprisingly simple method, commonly referred to as the "scotch tape method", to gently peel the single atomic layers of carbon atoms in graphite apart. This way, graphene, a new and strictly two-dimensional material was born. From that moment on the interest in graphene has boomed, and already in 2010 the discoverers were awarded the Nobel prize in physics for their groundbreaking reaserch.

The crystal lattice of graphene gives rise to astonishing mechanical, thermal and electronic properties. Not only has the material charge carriers that move as if they had no mass. The material also has a mobility, which is a measure for how easy the charge carriers can move through the material without scattering, an order of magnitude higher than any other material. Furthermore, graphene is the strongest material ever measured [3], hundred times stronger than steel. At the same time it is both brittle and ductile [4]. Its thermal conductivity is one of the highest measured and the atoms are so densely packed that not even a helium atom can pass through it [5].

One property that graphene doesn't have is a bandgap. As a result graphene absorbs the same amount of light, about 2.3% [6], across the whole spectrum from ultraviolet to far infrared light. For optical application this is an advantage and therefore graphene is expected to have a great potential in photonics and optoelectronics [7]. However, in terms of conventional electronics the lack of a bandgap is a drawback. The presence of a bandgap in silicon is the crucial property that allows the current to be turned on and off in silicon transistors, which is the basic for all standard digital computer chips. Thus, a lot of effort is made in order to find ways to induce a bandgap in graphene.

A further challenge that has to be overcome in order to bring any graphene product to the market is the large scale production of high quality graphene. Peeling graphene with scotch tape is a cumbersome work with a relatively low yield that usually only creates very

small flakes. This method is therefore only useful for research. In order to exploit graphene for any industrial applications growth methods to create wafer scale pieces are required. Despite the intense research on the growth of graphene, the quality of this graphene is still not comparable to the peeled one. However, it is most likely only a question of time before high-quality graphene can be reproducibly grown.

Chemistry on graphene

The physical properties of graphene immediately attracted a lot of interest. However, the chemical properties of graphene also deserve attention. By taking advantage of the chemistry of graphene new materials with appealing properties can be created. One example that has been created recently is an activated microwave-expanded graphite oxide that is a porous material with a remarkably high surface area and thus a promising material for ultrafast supercapacitors [8].

In terms of transport measurements on graphene, chemistry is interesting from several points of view. First of all functionalization of graphene is proposed as one possible route to engineer a bandgap in graphene [9], thus overcome one of them main challenges in order to use graphene for conventional transistors. Another motivation to chemically modify graphene is to achieve controlled doping. The possibility to control the type and furthermore the density of charge carriers via chemical doping could give access to new physics that is not observable at low charge carrier densities [10].

Another appealing possibility that might be offered by chemical functionalization is specific edge functionalization [11]. To obtain control over the graphene edges is one of the main challenges when it comes to graphene nanostructures.

Finally, chemistry on graphene offers the possibility to controllably introduce different defects into the graphene lattice that can be studied in transport. There has already been several such studies on fluorinated graphene [12, 13] and on ozone treated graphene [14] where the effect of defects on transport has been analyzed. Furthermore, when creating enough defects and thereby making the graphene insulating, chemical modification can provide an alternative to etching for the creating of nanostructures where it might even be possible to design the edges of nanostructures to some extent.

Graphene nanostructures

The continuous miniaturization of electronic circuits over the last fifty years has allowed us to fit more and more electronic components within a computer chip. As a result we have witnessed a steady increase in computer power. Now, as the working horses of the electronic industry, the silicon transistors are reaching their limits for miniaturization, new materials and solutions for further progress are sought. One candidate that has been suggested to replace silicon is graphene. However, the lack of a band gap makes it difficult to obtain large on-off ratio for graphene transistors. In fact, conventional design of transistors might not be feasible with graphene. In this context a novel class of nano-scale devices, three-terminal ballistic junctions, might offer a solution. The high mobility of graphene, persisting up to room temperature[15], makes graphene an excellent candidate for such devices. In addition, the possibility to tune graphene devices from

electron transport to hole transport offers further flexibility of such devices.

With a further decrease in device sizes the area where quantum effects start to play a role will be entered. This could lead to problems for conventional devices like for instance current leakage due to quantum tunneling. As a result a new research field which is not trying to circumvent the quantum mechanical effects, but is trying to exploit them, has developed over the last decade. This is the research field of quantum bits, usually simply called qubits. By processing information using qubits instead of classical bits problems such as integer factorization could be solved much faster than by any classical computer. Many different areas of physics work towards the realization of qubits and system of qubits. One of these is the field of semiconductor nanostructures. So far most progress towards semiconductor qubits has been made using GaAs-based quantum dots to realize qubits based on spin. The main problem with the GaAs-based spin qubits are the relative short spin-coherence times due to strong hyperfine interaction and spin-orbit coupling. Here graphene again comes into play. In carbon based materials both hyperfine interaction and spin-orbit coupling are expected to be significantly suppressed. This makes graphene an interesting material for spin qubits.

Even though a lot of progress has been made over the last couple of years in terms of fabricating and understanding transport through more and more advanced graphene nanostructures, there are still many challenges to overcome before the first high-mobility graphene device is on the market or the first qubit operation using a graphene based system is realized.

Structure of the thesis

This thesis starts with a brief introduction to the general electronic properties of graphene followed by a discussion of the standard sample fabrication used in this thesis to create graphene nanostructures on a SiO_2 substrate.

The experimental part of the thesis is divided into three main parts. In the first part we discuss several attempts to chemical functionalize graphene with diazonium chemistry with the goal to create defects in the graphene lattice that later can be investigated by transport measurements. We show that one of the main effects of functionalization is doping, and that in order to analyze this doping effect the doping effect of solvents involved in the functionization process has to be understood first. Furthermore, it is observed that under our present reaction conditions only few defects are introduced to the graphene lattice and a polymerization of the diazonium molecules are the preferred reaction.

In the second part transport in a three-terminal graphene junction is investigated. First the non-linear electronic properties of the device are probed at different temperatures from 4 K up to room temperature where a rectifying behaviour is observed to persist up to room temperature. Afterwards diffusive, phase-coherent transport including investigation of weak localization and universal conductance fluctuations are discussed. At the very end we briefly discuss the possibility to use this special three-terminal structure to probe the disorder potential of bulk graphene.

In the third and last experimental part of this thesis transport in a three-terminal graphene quantum dot is investigated. A shift in energy of Coulomb peaks measured at

the different leads are observed. This is interpreted as a signature of different couplings between the dot states and the different lead states. Furthermore finite bias measurements of Coulomb diamonds are discussed.

The thesis ends with a general conclusion and outlook.

Chapter 2

Basic concepts

Since its first experimental realization in 2004 [2] graphene has attracted a huge amount of interest in different research communities. In order to shed some light on this enthusiasm, especially the interest in the community of electronic transport in two-dimensional systems, we will here briefly discuss the very basic properties of graphene. First the crystal structure will be introduced, before the band structure with its implications will be discussed. For a more thorough description of these concepts see Ref. [16]

Subsequently transport properties of bulk graphene, which are frequently used to characterize graphene samples and therefore relevant throughout this thesis, are introduced. Finally, we introduce the Coulomb blockade effect in quantum dots, a phenomenon that will be further discussed in part III of this thesis.

2.1 Graphene

2.1.1 Crystal structure

Graphene is a single sheet of carbon atoms arranged in a honeycomb structure as shown in Fig. 2.1(a). The lattice can be seen as made out of two interpenetrating sublattices A (white atoms) and B (black atoms). The unit cell of the lattice (filled grey area) contain two atoms, one from each sublattice. The reciprocal lattice, which is obtained by rotating the real lattice by 90° is shown in Fig. 2.1(b). The grey hexagon represents the first Brillouin zone and K, K', M and Γ are important symmetry point of the reciprocal lattice. Especially the K and K' point will be discussed further below.

Each carbon atom has four valence electrons which occupy the 2s, $2p_x$, $2p_y$ and $2p_z$ orbitals. Since the 2s, and 2p orbitals have very similar energies they can mix to form different hybrid orbitals. In graphene the 2s, $2p_x$ and $2p_y$ orbitals mix to form three equal sp^2 hybrid orbitals. By overlapping the sp^2 orbitals from neighbouring carbon atoms, strong covalent σ-bonds are formed in the xy-plane, which result in the hexagonal structure seen in Fig. 2.1(a).

The $2p_z$-orbital is located perpendicular to the plane of the sp^2-orbitals and is un-

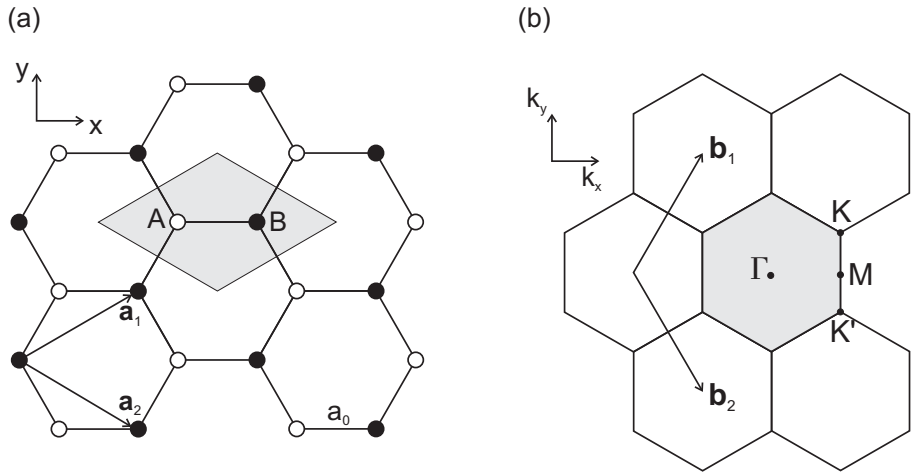

Fig. 2.1 — (a) The characteristic honeycomb lattice of graphene with the unit cell highlighted in grey. The lattice can be seen as made up of two interpenetrating triangular lattices (black atoms and white atoms). Thus, the unit cell contains one atom from each sublattice. The lattice vectors $\mathbf{a}_1$ and $\mathbf{a}_2$ and the carbon-carbon nearest neighbour distance a_0 are indicated. (b) The reciprocal lattice with the Brillouin zone colored grey. $\mathbf{b}_1$ and $\mathbf{b}_2$ are the reciprocal lattice vectors and Γ, M, K and K' are important symmetry points of the reciprocal lattice.

affected by the formation of the σ-bonds. The $2p_z$-orbitals from neighbouring atoms overlap in a sideway manner to from distributed π-bonds above and below the plane of the σ-bonds. This system of delocalized, loosely bonded π-electrons is responsible for the electrical conductivity of graphene. Hence, only the π-electrons have to be considered in the derivation of the electronic band structure of graphene.

2.1.2 Band structure

The band structure of graphene was first calculated by Wallace in 1947 [17] using the so called "tight-binding" approach where it is assumed that the atomic wave functions are well localized on their respective atoms. The final dispersion relation resulting from this calculation when only considering nearest neighbour interaction can be written as

$$E(k_x, k_y) = \pm t\sqrt{1 + 4\cos\left(\frac{\sqrt{3}k_x a_0}{2}\right)\cos\left(\frac{k_y a_0}{2}\right) + 4\cos^2\left(\frac{k_y a_0}{2}\right)} \tag{2.1}$$

where t is the nearest neighbour hopping energy and a_0 is the carbon-carbon nearest neighbour distance (see Fig. 2.1(a)). The plus sign in Eq. 2.1 corresponds to the upper π-band (conduction band) and the minus sign to the lower π^*-band (valence band).

The band structure obtained from Eq. 2.1 is plotted in Fig. 2.2. In transport experiments we are mainly interested in the low energy region emphasized by the zoom in Fig. 2.2. In this region the valence band and the conduction band form the characteristic cones that meet at the K and K' points of the Brillouin zone. The absence of a band gap have important practical implications for transport experiments in graphene, and will be discussed throughout this thesis.

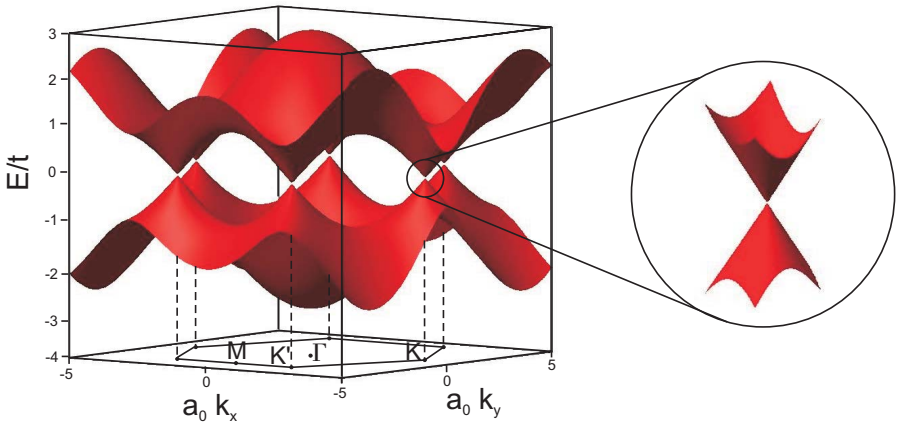

Fig. 2.2 — The band structure of graphene calculated with the tight-binding model. The relation between the band structure and the reciprocal lattice is illustrated as a projection of important symmetry points. The cones formed at low energies are emphasized by the zoom.

The low energy properties of graphene can be well described by making a linear expansion of the band structure around K and K' [17, 16, 18]. The final result of such an expansion can be written as

$$E(\mathbf{k}) = \pm\hbar v_{\mathrm{F}}|\mathbf{k}| \tag{2.2}$$

where $v_{\mathrm{F}} \approx 1{\cdot}10^6$m/s is the Fermi velocity. This linear energy dispersion relation resembles the one of massless relativistic particles. As a result the charge carriers in graphene are described by the 2D Dirac equation and actually behave as if they were massless relativistic particles where the role of the speed of light is played by the Fermi velocity. This is an important difference from a conventional 2D electron gas system which has a parabolic dispersion relation and therefore is described by the 2D Schrödinger equation.

2.1.3 Charge carriers in graphene as Dirac fermions

Let us now have a look at the implications of the linear dispersion relation for transport in graphene. Close to the K and K' points the charge carriers in graphene can be described by a two component wave function $\psi(\mathbf{r})$ which obeys the 2D Dirac equation [16]

$$-iv_{\mathrm{F}}\sigma \cdot \nabla\psi(\mathbf{r}) = E\psi(\mathbf{r}) \tag{2.3}$$

where σ are the 2D Pauli spin matrices. This two-component wavefunction resembles the spinor wavefunction of quantum electro dynamics (QED). Corresponding to the spin of particles in QED, the charge carriers of graphene can therefore be attributed a so-called pseudospin σ. It should be pointed out that the pseudospin has nothing to do with the real spin of the electrons, but is a direct result of the two different carbon sublattices [19]. The pseudospin index corresponds to bonding and antibonding combinations of the two sublattices, not to the real spin of the electrons.

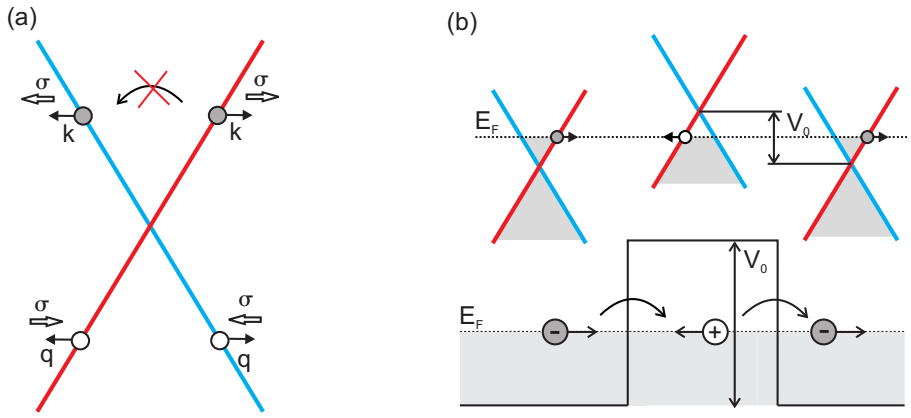

Fig. 2.3 — (a) Sketch of the energy dispersion around the K point. The red curve corresponds to the antibonding state and the blue curve to the bonding state. The conservation of pseudospin σ suppress backscattering. (b) Klein tunneling through an npn barrier.

The pseudospin of the charge carriers can have two values, either in the direction of or against the momentum. As a result the electrons and holes close to the K and K' points in graphene have a well defined helicity. Fig. 2.3(a) shows a sketch of the energy dispersion around the K point. Quantum mechanical hopping between the two sublattices leads to an antibonding state (red branch) and a bonding state (blue branch) [20]. It can be seen that an electron with energy E travelling in the positive direction originates from the same branch as a hole with energy -E travelling in the negative direction. As a result the electrons and holes from the same branch have the same pseudospin. Two important implication that follows from this is suppressed backscattering and so-called Klein tunnling.

It can be seen from Fig. 2.3(a) that a backscattering process requires the pseudospin to flip. This is only possible in the presence of short range scatterers that act differently on the two sublattices. For long range scatterers backscattering is expected to be completely suppressed [21]. As a result high mobilities, persisting up to room temperature, are possible in graphene [15].

Klein tunnling is another important result of the helicity of the charge carriers in graphene [20]. In classical physics an electron hitting a potential barrier as shown in Fig. 2.3(b) is reflected with 100% certainty. In non-relativistic quantum mechanics the electron can tunnel thorough the barrier, but the probability of tunneling exponentially decays with increasing height and width of the barrier. In relativistic quantum mechanics, however, the barrier gets perfectly transparent, even in the limit of infinite barrier height. This situation is known as the Klein paradox. The Klein paradox is normally understood in terms of electron-positron pair creation. In graphene it can be understood in terms of electrons and holes. A barrier which is repulsive for electrons will be attractive for holes. Since there are hole states inside the barrier with the same energy as the electrons outside, an electron arriving at the barrier can tunnel through it as a hole before leaving again as an electron. An important implication of Klein tunnling for transport in graphene is that the charge carriers cannot be confined by potential barriers. Klein tunneling in graphene

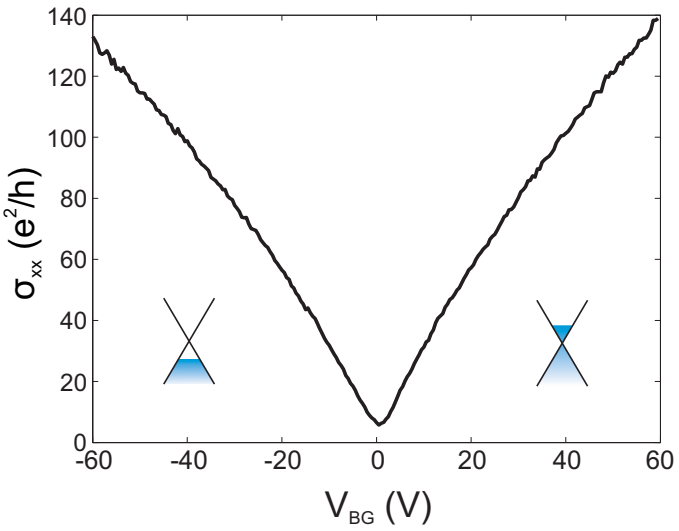

Fig. 2.4 Electric field effect in graphene. Conductivity σ as a function of backgate voltage V_{BG} for a large backgate voltage range measured by applying a constant current of 10 nA to a graphene Hall bar at a temperature of 4 K. The minimum of conductivity mark the so-called charge neutrality point (CNP). To the left of the CNP the transport is governed by holes, while to the right transport is carried out by electrons. This is illustrated with the corresponding schematics of the low energy dispersion relation with the Fermi level in the situation of hole transport and electron transport.

was early predicted [20] and has also recently been experimentally observed [22, 23].

2.2 Transport in bulk graphene

2.2.1 Electric field effect

All modern electronics are based on the ability to control the electronic properties of a material by applying an external voltage. This is done by the so-called electric field effect where an applied gate voltage changes the carrier concentration of the material and consequently its conductivity. The electric field effect in graphene, which was fist reported by Novoselov et al. in 2004 [2], is widely used as a characterization tool in transport measurement.

A typical measurement of the electric field effect in graphene on a SiO_2 substrate is shown in Fig. 2.4. By changing the backgate voltage the charge carrier density of the device is tuned from hole-transport, via the point of minimum conductivity (the charge neutrality point CNP), to electron-transport. The induced charge carrier density can be estimated from a parallel plate capacitor model as

$$n = \frac{\epsilon\epsilon_0}{ed}\Delta V_{\mathrm{BG}} = \alpha V_{\mathrm{BG}} \tag{2.4}$$

where ϵ_0 is the permittivity of vacuum, $\epsilon = 3.9$ the permittivity of SiO_2, d is the thickness of the oxide layer and ΔV_{BG} is the backgate voltage applied relative to the CNP. An oxide thickness of 300 nm thus gives $\alpha = 7.2 \cdot 10^{10}\mathrm{cm}^{-2}/\mathrm{V}$.

For small charge carrier densities the conductivity in Fig.2.4 is seen to increase linearly with applied backgate voltage away from the charge neutrality point. This is a signature of charged impurity scattering [24–26], which is considered to be the main scattering mechanism limiting the mobility of graphene devices on SiO_2. For a linear relationship

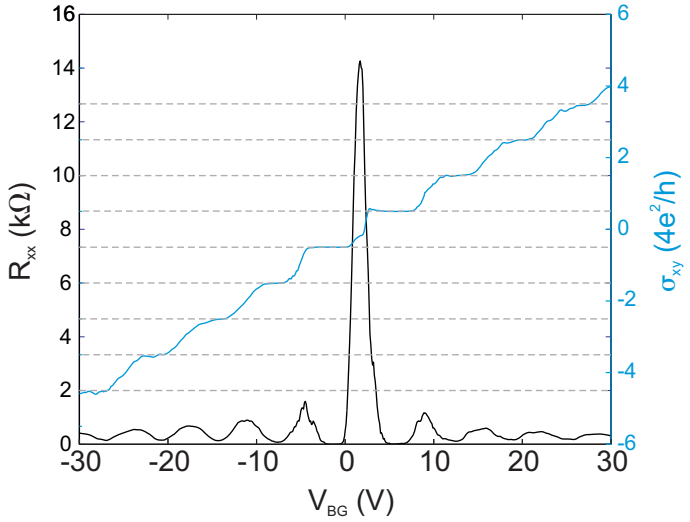

Fig. 2.5 Longitudional resistance and Hall conductivity σ_{xy} as a function of backgate voltage measured on a graphene Hall bar at a magnetic field of 5 T and a temperature of 4 K. The measured plateaus in the Hall conductivity coincide nicely with the theoretical expected values, marked by grey dashed lines.

between the conductivity and the charge carrier density n and the mobility μ can be extracted using the normal Drude formula $\sigma = ne\mu$.

For larger charge carrier densities a slight sublinear behaviour associated with short-range scatterers is observed [24–27]. It has been shown that using self-consistent Boltzmann theory combining scattering from long and short-range sources one obtain the following (slightly more complicated than the Drude formula) expression for the conductivity

$$\frac{1}{\sigma} = \frac{1}{\sigma_{\text{long}}} + \rho_{\text{short}} = \frac{1}{ne\mu + \sigma_{\text{res}}} + \rho_{\text{short}} \tag{2.5}$$

where the first term is due to long range scatterers (charged impurity scatteres) giving the linear realationship between conductivity and charge carrier density as described above, σ_{res} is the residual conductivity at the CNP [26] and ρ_{short} is the density independent contribution from short range scatterers that leads to the sublinear behaviour at higher densities. For mobilities below 5000 cm^2/Vs the transport is completely dominated by charge impurity scattering and no sublinearities are observed. However, for higher mobilities, where the amount of charged impurity scatteres are lower, the contribution from short-range scatterers start to play a role and the sublinearites can be observed.

2.2.2 Quantum Hall effect in graphene

When a sufficiently high perpendicular magnetic field is applied to a two-dimensional material its energy spectrum gets quantized [28]. For a conventional 2D electron gas with a parabolic dispersion relation the energies of these quantized states are given by $E_n = \hbar\omega_c(n + 1/2)$ where $\omega_x = |e|B/m^*$ is the cyclotron frequency and n is an integer [18]. These states are known as *Landau levels* and can be visualized as broadened delta peaks in the density of states of the charge carriers. This quantization of the energy spectrum can be observed as oscillations in the longitudional magnetoresistance, known as *Schubnikov de Haas (SdH) oscillations*, when either the magnetic field strength of the charge carrier density is changed. Correspondingly steps can be observed in the transverse Hall resistance which is known as the quantum Hall effect.

As a direct consequence of the linear dispersion relation near the K and K' points in graphene the above expression for the energy of the Landau levels does not hold for graphene. The graphene Landau levels are instead given by [29]

$$E_n = \mathrm{sgn}(n)\sqrt{2e\hbar v_{\mathrm{F}}^2|n|B}, \quad n \in \mathbb{Z} \tag{2.6}$$

where $n > 0$ represent electron-like Landau levels and $n < 0$ represent hole-like Landau levels. In addition a Landau level with $n = 0$ at zero energy which is shared between electrons and holes is present. This leads to the striking shift of the quantum Hall plateaus to half integer filling factors. The values of the quantum Hall plateaus are thus given by

$$\sigma_{xy} = \pm 4\frac{e^2}{h}(n - \frac{1}{2}) \tag{2.7}$$

where n is a non-negative integer and $\pm$ corresponds to electrons and holes, respectively. The factor 4 is due to the fourfold degeneracy of each Landau level. Each Landau level can be occupied by two opposite spins and two opposite valleys.

A typical measurement of the quantum Hall effect in graphene is depicted in Fig. 2.5 where the longitudional resistance R_{xx} and the transverse conductivity σ_{xy} are plotted as a function of backgate voltage at a constant magnetic field of 5 T. When the Fermi energy is situated between two Landau levels a plateau is seen in the Hall conductivity and the corresponding longitudional resistance is zero. The grey dashed lines indicate the expected values for the Hall plateaus according to Eq. 2.7 and the measured plateaus fit nicely to the expected values.

2.3 Coulomb blockade effect in quantum dots

As an introduction to chapter 9 a very brief description of the most important properties of quantum dots will be given in this section. For a more thoroughly description of transport in quantum dots we refer to Ref. [30, 31].

A quantum dot consist of an conductive island weakly coupled to source and drain via tunnel coupling as depicted in Fig. 2.6(a). Additionally a capacitively coupled plungergate which can be used to tune the energy levels of the dot is situated next to the dot.

When the transport through a quantum dot is dominated by Coulomb interaction between electrons the so-called Coulomb blockade effect, which is one of the fundamental transport phenomena in quantum dots, can be observed. The basic idea is that in order to add an additional electron to the island a finite energy is needed to overcome the Coulomb repulsion between electrons. The Coulomb blockade effect can be intuitively understood by looking at the energy level diagram of a quantum dot system drawn in Fig. 2.6(c) and (d). The electronic levels of the source and drain contacts are filled with electrons up to their chemical potentials μ_S and μ_D respectively. By applying a bias voltage V_{bias} between source and drain a difference between μ_{S} and μ_{D} is created. This difference is called the "bias window" and is given by eV_{bias}. For the island containing N electrons we define the electrochemical potential μ_{N}. This electrochemical potential describes the energy necessary to add an electron to the dot, given that it is initially and after the

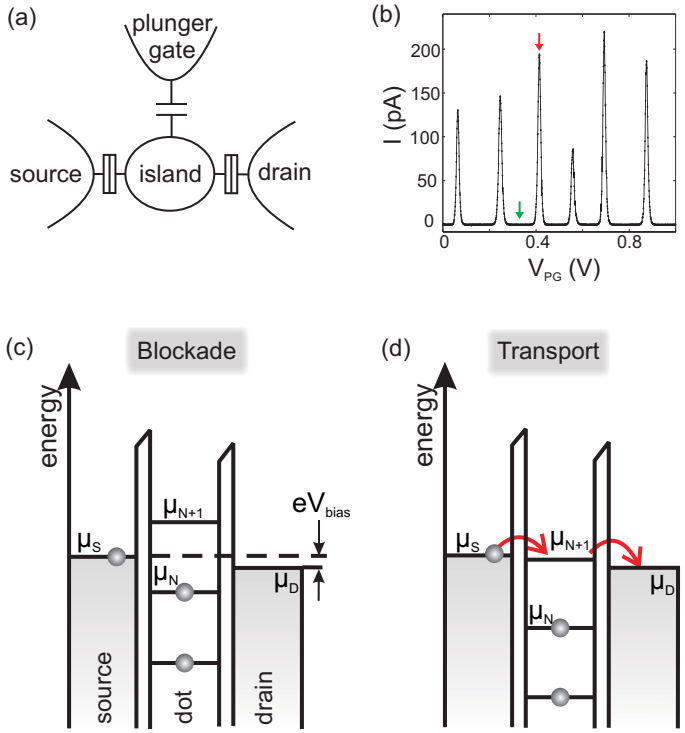

Fig. 2.6 — (a) Schematic drawing of a quantum dot with a capacitively coupled plungergate. (b) Energy diagram of the of the quantum dot system in the situation of Coulomb blockade. (c) Energy diagram of the quantum dot system in the situation of transport through the dot. (d) Measurement of characteristic Coulomb resonances.

addition in its ground state [30]. Thus, for the case with N electrons on the dot, μ_{N+1} is the energy needed to add an additional electron to the dot. In the situation showed in Fig. 2.6(c) $\mu_{N+1} > \mu_S$. In this case the electron in the source does not have enough energy to tunnel onto the island and the transport is blocked.

If now the capacitively coupled plunger gate is used to lower the energy levels of the dot, at one point the situation depicted in Fig. 2.6(c) will be reached. Here $\mu_S > \mu_{N+1} > \mu_D$ and transport through the dot is possible. Since the energy to add a second electron to the dot μ_{N+2} is much larger than μ_{N+1} only one electron can tunnel through the dot at a time. Thus, the transport is referred to as sequential single electron tunneling.

When measuring the current through a quantum dot as a function of plungergate voltage a peak in the current is seen every time a new energy level of the island enter the bias window and transport is allowed. This is shown in Fig. 2.6(d). The green arrow mark the situation of blocked transport corresponding to Fig. 2.6(c), while the red arrow mark the situation of transport corresponding to the situation in Fig. 2.6(d).

When the bias voltage applied between source and drain is increased, the region in plunger gate voltage of the current carrying situation will increase. By measuring the current as a function of both plunger gate voltage and the bias voltage diamond shaped regions of suppressed current can be observed. These are the so-called Coulomb diamonds.

Chapter 3

Sample fabrication

Graphene is the basic building block for all the other members of the family of graphitic carbon allotropes. It can be stacked into 3D graphite, rolled up to 1D carbon nanotubes or shaped into 0D fullerenes. On paper, graphene has therefore existed for a long time as a theoretical building block for other graphitic materials. However, it was predicted, and therefore for a long time believed, that a 2D crystal like graphene could not be stable at room temperature [1].

Sill various attempts to separate graphite into single layers was made during the years. One chemical approach was to intercalate graphite with other molecules in order to cleave graphite into graphene [32–34]. Other attempts have been made by using a so-called 'nano pencil' where small graphite pieces mounted on an SFM tip are cleaved into few layer graphene samples by dragging the tip along a surface [35] or by manipulating on-chip graphite pillars with an SFM tip [36]. Despite all these different efforts, graphene was not experimentally realized before 2004 when A. Geim and coworkers at the Univeristy of Manchester introduced the so-called 'scotch-tape method' where graphite is simply cleaved into graphene using a sticky tape [2]. Even though a lot of effort has been made during the last couple of years in order to grow graphene epitaxially, the quality of such graphene is still significantly lower than the one obtained by the "scotch-tape method". Therefore the relative cumbersome cleaving of graphite using a sticky tape is still the preferred method for obtaining graphene for transport experiments.

In the following a overview of the most important step of the sample fabrication from the exfoliation of the graphene flakes to the final etching and contacting of the structure will be given. Detailed process parameters can be found in Appendix C.

3.1 Exfoliation and deposition

As a substrate we use highly doped silicon wafers with a thermally grown silicon dioxide (Si_2) layer of 295 nm on top (supplier: Nova Electronics).[1]. Before graphene deposition

[1] In order to minimize substrate-induced disorder the last samples studied in this thesis are deposited on highly doped silicon wafers with chlorinated silicon dioxide on top [37]

the whole 4 inch wafers are patterned with bond pads and alignment markers by electron beam lithography (ebl) followed by the evaporation of 5 nm Ti and 45 nm Au. Afterwards the wafers are diced into 7x7 mm chips suitable for graphene deposition.

The scotch tape technique is surprisingly simple. No expensive or hazardous equipment is needed, only some adhesive tape and graphite. Consequently, high quality single layer graphene can be produced in any lab, at any high school or even in your own kitchen. This has been an important contributing factor to the boom of graphene research.

The idea behind the technique is to overcome the weak attractive forces between the atomic layers of graphite by gently pulling them apart using adhesive tape. First a large piece of natural graphite is gently pressed onto the tape and carefully removed again. This leaves a layer of graphite on the tape which is the starting point for further exfoliation. The tape is then folded several times in order to cleave the graphite additionally. It is crucial to fold the tape gently. If the tape is pressed hard together, the graphite is crunched into powder and only very small graphene flakes are obtained. The natural graphite is exfoliated using either scotch tape or a blue clean room tape which is normally used for wafer dicing. The scotch tape is more adhesive than the clean room tape, resulting in more and larger flakes, however, the clean room tape leaves less glue residues on the chips and the flakes. When a thin layer of evenly distributed graphite covers the tape the graphene is deposited onto the substrate by evenly pressing the chip onto the tape and carefully removing it again.

3.2 Characterization

The three main methods used to characterize graphene flakes are light microscopy, Raman spectroscopy and scanning force microscopy (SFM). In the following the advantages and the limitation of these different characterization tools will be discussed. In addition, a detailed statistical comparison between light microscopy and Raman spectroscopy for determining the number of graphene layers on a Si/SiO_2 substrate can be found in appendix A.

3.2.1 Light microscopy

After deposition the Si/SiO_2 chip is covered with graphite pieces of different thicknesses, ranging from single-layer graphene to thick chunks of graphite. In order to find single or few layer graphene flakes among the large amount of graphite pieces, it is crucial with a fast and simple searching method. Different modern microscope techniques with high resolution like SFM or scanning electron microscopy (SEM) are not suitable due to low speed and the absence of a clear signature of the number of layers respectively [1]. The solution came with the realization that single layer graphene is visible by eye if put on a Si substrate covered by a carefully chosen thickness of SiO_2. This discovery allowed for a fast search for graphene flakes and was just as essential for the first demonstration of graphene as the scotch tape method itself. As already mentioned above a SiO_2 thickness of 295 nm, which gives a good visibility of graphene in white light [2], is used in this work. Fig. 3.1 shows a light microscope image of a single layer flake (marked with the dotted

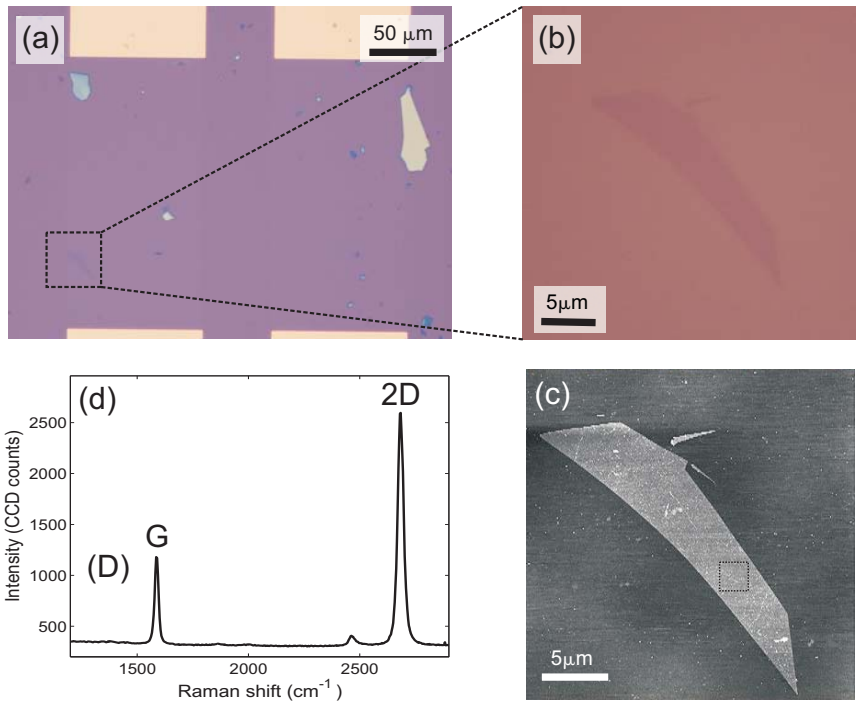

Fig. 3.1 — (a) Light microscopy image of a graphene flake deposited on a Si/SiO_2 chip. The large metal squares used as bond pads and the small metal crossed used as ebl markers that are patterend on the chips before deposition can be seen. In addition graphite pieces of different thicknesses ranging from pink (a few layers) to blue (30-50 nm) to grey can be seen. (b) A zoom of the single layer flake from (a). This is the flake that is later processed into sample AJ 54. (c) Corresonding SFM image. within the marked square the roughness of the flake is $R_q = 0.3\,\text{nm}$. (d) A typical Raman spectrum for single layer graphene. The G and the 2D line can be clearly seen, while the D line is absent.

box) surrounded by thicker graphite pieces. The large golden squares are bond pads which are patterned on the chip before graphene deposition. In Fig. 3.1(b) a zoom of the single layer flake can be seen.

In principle the single layer nature of the flake can be confirmed from the optical contrast alone. However, since the optical contrast depends on several set-up specific parameters it needs to be calibrated in order to use it for determination of the number of graphene layers. In appendix A such a calibration is shown where one can unambiguously determine the number of layers up to 5 layers. It is further shown that for more than two layers light microscopy is actually the superior tool for determining the number of layers.

3.2.2 Raman spectroscopy

Raman spectroscopy has been an important tool for characterizing graphitic materials for many years [38] and lately it has also become a widely used and powerful tool to characterize single and bilayer graphene. [39, 40] Fig. 3.1 (c) shows a typical Raman

spectrum of single layer graphene. Two characteristic peaks, the G peak at around 1580 cm^{-1} and the 2D peak at around 2700 cm^{-1}, can be seen. In the case of a disordered sample or at the graphene edge the so-called disorder-induced D-peak around 1350 cm^{-1} is also present[38].

The G-peak is associated with the doubly degenerate phonon mode at the Brillouin zone center and is the only peak in the Raman spectrum of graphene which originates form a normal first order Raman scattering process. The D and 2D peaks originate from a second order process involving two phonons near the K-point at the edge of the Brillouin zone for the 2D peak and one phonon and one defect for the D-peak. They can be understood within the framework of double resonant Raman processes[41] which links the phonon wave vectors to the electronic band structure of graphene[39]. As a result, for single layer graphene, with its single valence and conduction band, only one transition is allowed giving a single 2D peak. For bilayer graphene the valence and conduction bands are split into two, therefore allowing 4 transitions, splitting the 2D peak of bilayer graphene into four components. Consequently, the width of the 2D peak can be used to unambiguously identify single and bilayer graphene. For three and more layers the number of allowed transitions increases and the corresponding width of the 2D peak increases, however, as shown in appendix A the exact number of layers cannot be uniquely determined.

In addition to the identification of single and bilayer graphene Raman spectroscopy is also widely used to study the quality of graphene. The intensity of the D-line is commonly used as a direct measure of the amount of defects in graphene[42, 11, 43, 27, 44–46]. Furthermore, the position of the G-line[47, 48] and the intensity ratio between the G-line and the 2D-line are sensitive to doping. This will be further discussed in chapter 4 and 5 of this thesis where Raman spectroscopy is used togther with transport experiments to probe the influence of chemical modification on graphene.

3.2.3 Scanning force microscopy

In a final characterization step the surface of the graphene flakes are investigated by scanning force microscopy. Glue residues remaining on the graphene surface after exfoliation, wrinkles and other inperfections of the surface, which are not visible in the optical microscope, can be detected by SFM. To obtain low contact resistances and minimize the doping of the processed devices only flakes which looks sufficiently clean and flat in the SFM scans is considered for further processing.

Fig. 3.1(d) shows the SFM image corresponding to the optical image in Fig. 3.1(b). Some glue residues can be seen as white spots on the graphene flake (and on the surrounding substrate). However, within the area marked with a dotted square (where the device is later defined) the graphene is clean with a surface roughness measured to be 0.3 nm, which is close to the intrinsic roughness of the SiO_2 (0.2 nm).

The height of the flake is measured to be 2 nm. Typically single graphene flakes are found to have heights between 0.6 and 2.5 nm when measured by SFM. The large measured heights compared to the intralayer distance of graphene sheets in graphite (≈ 0.34 nm), and the large variation of the heights is most likely due to a combination of water adsorbed underneath the flake and glue residues from the exfoliation residing below the flake. As a result AFM is not a suitable tool to distinguish between single, bilayer and few layer

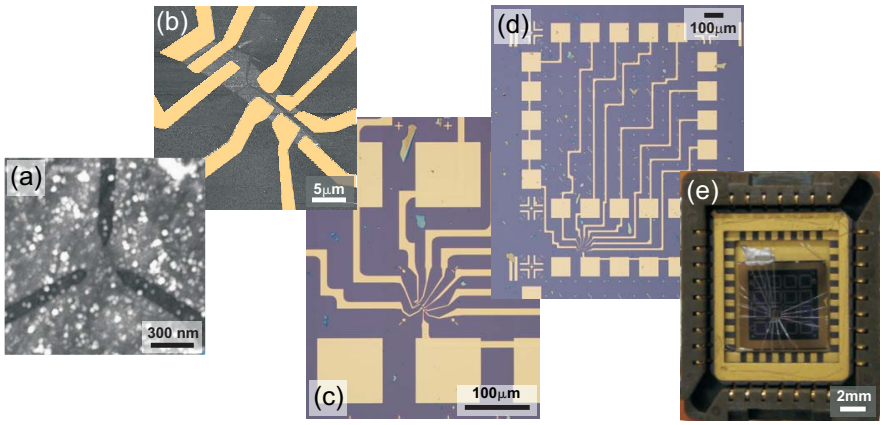

Fig. 3.2 — A finished graphene device. (a) A scanning force micrograph image of the center of the device where the three trenches etched into the graphene flake are nicely visible. (b)-(d) A scanning force micrograph image and light microscopy images showing how the device is contacted. (e) The chip is glued into the chip carrier, bonded and fixed into the sample holder.

graphene.

3.3 Processing

The characterized graphene flakes are structured and contacted using electron beam lithography (ebl). In a first ebl step the contacts are defined. To achieve as low contact resistances as possible two different layers of Polymethylmethacrylate (PMMA) resist is used. For the upper layer we use PMMA 950K while for the lower layer we use PMMA 50K. (950K and 50K represents the molecular weight of the PMMA chains.) The short PMMA chains of PMMA 50K are easier to remove from the chip than the longer PMMA 950K chains, consequently leaving less residues on the graphene after development and improving the contact resistances. After ebeam exposure and development 5 nm Ti or Cr, followed by 45 nm of Au is evaporated.

In a second ebl step the structures are patterend using one thin layer of PMMA 950K as resist. By using a 45 nm thick resist layer reproducible single pixel lines (SPL) of 25 to 30 nm are obtained. These are then etched with reactive ion etching (RIE) with argon and oxygen plasma.

Since the etching of the structure is the most critical part of the device processing the two ebl steps are sometimes interchanged at the cost of slightly incresaed contact resistances.

Fig. 3.2 shows a finished graphene device. Fig. 3.2(a) shows the center part of the device where three lines are etched into the graphene flake. In (b)-(d) it can be seen how the flake is contacted and in (e) the chip (glued into the chip carrier and bonded) is fixed into the sample holder and ready to be measured.

Part I

Chemical modification of graphene

Chapter 4

Towards chemical modification of graphene: Focus on solvent effects

The interest in chemical functionalization of graphene is increasing. One important motivation is the possibility that chemistry can be used to tune the electronic properties of graphene and create a bandgap if desired. This, together with the potential of controlled doping and selective edge functionalization, makes chemical modification of graphene highly interesting for electronic transport experiments.

Here, we study graphene modified by diazonium chemistry where aryl groups are covalently attached to the graphene lattice. Diazonium chemistry has previously been widely used to modify a variety of sp^2-hybridized carbon materials like HOPG [49], glassy carbon [49, 50] and carbon nanotubes [51, 52]. Very recently, also the successful grafting of aryl groups to the graphene surface has been shown [11, 45, 53, 54]. Still, detailed studies of the influence of the attached functionalized group on electronic transport in graphene are rare.

In order to investigate the influence of functionalization on transport in graphene it is important to be aware of the fact that not only chemistry has an effect on electron transport, it is well known that transport is also influenced by defects and dopants resulting from the different processing step. However, what has not been so clear up to now is how for instance organic solvents used in standard chemical reactions influence the transport. And to which extent any changes due to solvents can be distinguished from the effects of functionalization itself.

In this chapter we first introduce the reaction of diazonium molecules with the graphene lattice. Then a first attempt to functionalize graphene is presented. The last part focuses on how organic solvents frequently used in chemical reaction processes change the transport properties of graphene devices in a manner that might be difficult to distinguish from the effect of functionalization itself. Finally, it is shown how one can can get rid of unwanted solvent effects when analyzing transport data of functionalized graphene.

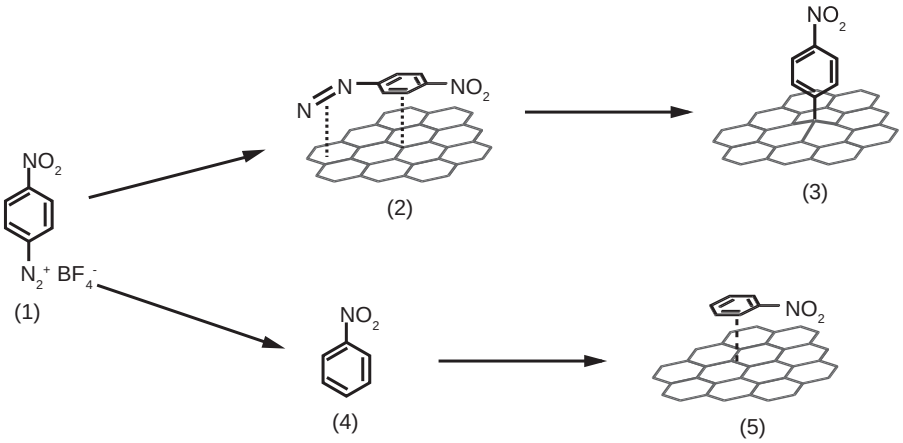

Fig. 4.1 — Schematic representation of possible reaction pathways on graphene. In the preferred reaction the diazonium reagent (1) adsorbs on graphene (2) and decomposes in a second step to form a covalently bonded nitrobenzene moiety on the graphene surface (3). In another possible reaction the diazonium reagent (1) decays to nitrobenzene (4) which is purely adsorbed on the graphene surface (5). In the latter case no reaction between the diazonium reactant and the graphene surface takes place. (Figure adapted from Ref. [45].)

4.1 Diazonium chemistry on graphene

Diazonium compounds are a group of organic compounds that have the molecular structure R-N_2^+ X-, where R is an organic residue, typically an alkyl or aryl group, and X is an inorganic or organic anion such as a halogen. One common way to isolate diazonium compounds is as tetrafluorborate salts, which are stable at room temperature. In this work we investigate the functionalization of graphene with 4-nitrobenzene-diazonium-tetrafluorborate (NBD)(supplier: Sigma Aldrich). The possibility of exchanging the nitro group (NO_2) with another substituent offer important tunability of the physical and especially the chemical properties of the functionalized graphene.

Fig. 4.1 shows two possible reaction pathways for NBD in contact with graphene. The upper part shows the desired grafting reaction where the diazonium ion react with a carbon atom of the graphene lattice. In a first step (2), the diazonium ion is brought in close proximity to the graphene lattice. As a result the electron withdrawing N_2^+ group withdraws an electron from the π electron cloud of the graphene lattice and forms a sigma bond between a graphene carbon atom and the diazonium molecule with the release of N_2 gas. The result is a covalently bonded nitrobenzene group perpendicular to the graphene plane (3). In addition to to this reaction, the reaction depicted in the lower part of Fig. 4.1 is also possible. Here the diazonium ion decomposes into nitrobenzene (4), before interacting with the graphene lattice. This compound and also the starting compound (1) may absorb on graphene (5).

In a previous related work it has been shown that these two reaction pathways can be distinguished by Raman spectroscopy where the covalent bonding of diazonium moieties to the graphene lattice leads to a pronounced D-line (defect line) in the graphene Raman specturm, while no D-line is observed after the adsorption of nitrobenzene [45]. In the

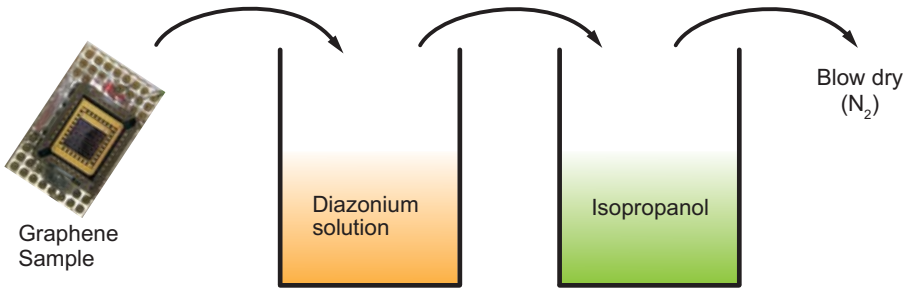

Fig. 4.2 — Schematics drawing of the functionalization procedure. The bonded graphene device is mounted in a shorted chip carrier which is first immersed into the diazonium solution. Subsequently it is immersed into isopropanol to remove all unreacted species, before it is carefully blown dry with nitrogen gas.

case of adsorption only shift of the G-line, known as a doping effect [48, 47], is observed.

4.2 Functionalization procedure

Contacted and etched graphene devices are step-wise functionalized and investigated by electronic transport experiments between each step. In order to prevent damage of the device due to electrostatic discharge, the graphene device is mounted in a chip socket where all pins are shorted onto a metallic plate during the complete functionalization process.

The functionalization is carried out in a diazonium solution which is prepared by dissolving NBD in water. The general functionalization procedure is shown in Fig. 4.2. In a first step the shorted sample is immersed into the diazonium solution for a chosen reaction time, typically between 1 minute and 20 hours. Afterwards the sample is immediately immersed into isopropanol where it is thoroughly cleaned to remove any unreacted diazonium species. Finally the sample is carefully blown dry with nitrogen gas and put back into the measurement setup.

4.3 A first functionalization attempt

In a first functionalization attempt a contacted graphene flake is functionalized in a 4 mmol l^{-1} diazonium solution at 0°C. In Fig. 4.3 (a) room temperature measurements of the conductance (G) as a function of backgate voltage (V_{BG}) are shown for (i) an unfunctionalized sample (only heated in order to remove dopants from the surface), (ii) after 5 minutes of functionalization and (iii) after 100 minutes of functionalization. These are two-terminal measurements on an unpatterned graphene flake (see the light microscope image of the measured device in the inset in Fig. 4.3). From Fig. 4.3 (a) it can clearly be seen how the functionalization shifts the point of minimum conductance (the charge neutrality point CNP, V_{CNP}), to the left, corresponding to an increased p-doping of the graphene flake. Before functionalization the CNP is located at +9 V in backgate. Af-

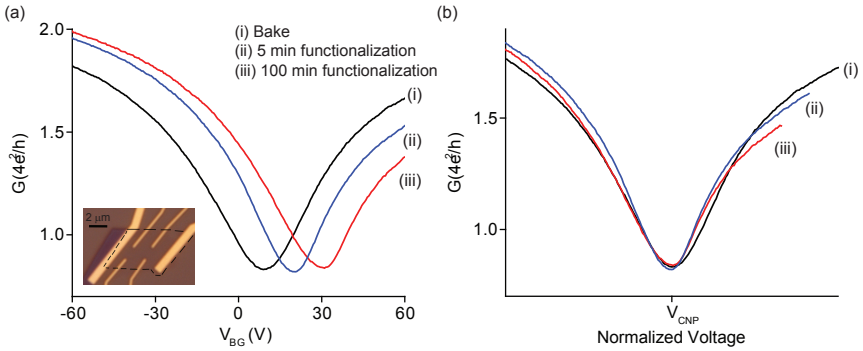

Fig. 4.3 — a) Room temperature measurement of the two-terminal conductance as a function of backgate voltage (i) after baking the sample, (ii) after 5 minutes functionalization and (iii) after 100 minutes functionalization. (b) The curves in (a) laterally shifted and normalized with respect to the charge neutrality point (V_{CNP}) The inset in (a) shows a light microscope image of the investigated sample where the dotted line indicates the contour of the graphene flake.

ter 5 minutes of functionalization the CNP is shifted to +21 V and after 100 minutes of functionalization the CNP is at +31 V. In Fig. 4.3 (b), where the backgate traces are normalized with respect to V_{CNP}, it can be seen that the functionalization introduces a small asymmetry between electron and hole transport. However, this asymmetry is much weaker than the asymmetry observed by Farmer et al. in a similar experiment [55]. From Fig. 4.3 (b) it can be additionally seen that the mobility (slope of G versus voltage) of the graphene flake is not significantly changed after functionalization. As will be discussed in the following sections of this chapter, these observations can all be explained by a combination of few bonded diazonium moieties due to the low reaction temperature (0°C) and uncompensated solvent effects.

4.4 Solvent effects

In the functionalization process described section 4.2 the graphene flake is first immersed in water containing the reactive diazonium ions and afterwards in isopropanol to remove unreacted species and improve the drying step. In order to analyze the influence only of the chemical functionalization on the electronic transport properties of graphene it is important to first know the effect of the involved solvents. In the following we will therefore investigate the influence of isopropanol and baking on graphene's transport properties.

To investigate the influence of isopropanol and heating we use the Hall bar shown in the inset in Fig. 4.4 (b). The width of the Hall bar is 1 μm and the length between two voltage probes is 2 μm. All the following measurements are four-terminal measurements. For the isopropanol treatment the chip with the Hall bar is immersed in isopropanol for 5 minutes and afterwards blown dry with nitrogen gas. The heating of the sample is done in the sample holder while the vacuum is constantly pumped. In order to monitor changes in the conductivity of the sample during the heating process a constant current of 10 nA is applied to the Hall bar and the four-terminal resistance is measured at $V_{\mathrm{BG}} = 0$ V. The sample is always heated at around 100°C until the measured resistance is stable. This

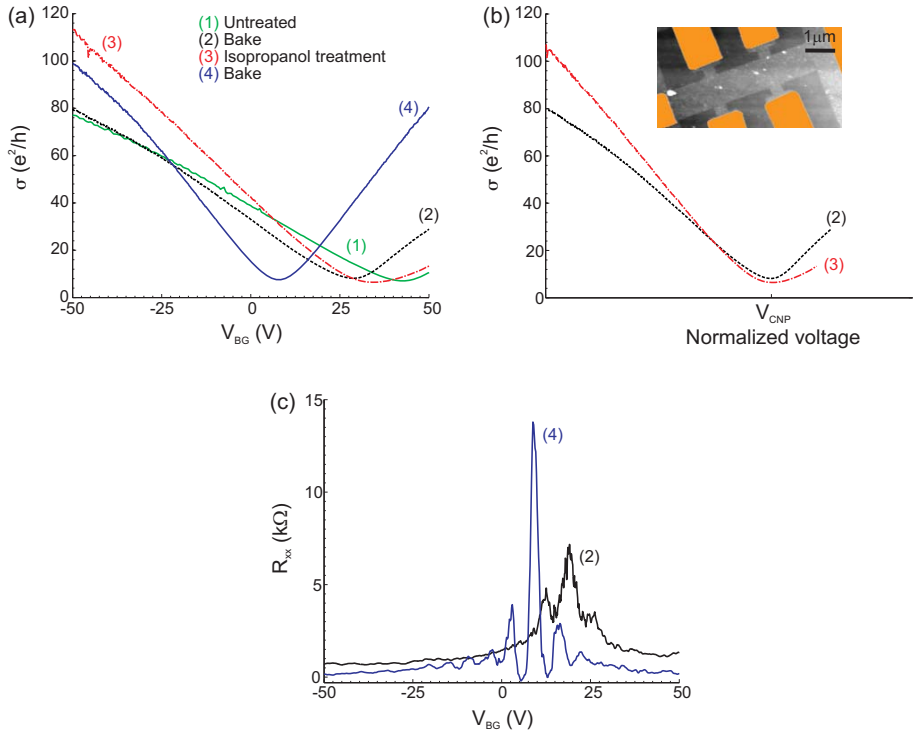

Fig. 4.4 — (a) Room temperature measurement of the four-terminal conductivity as a function of backgate voltage for an untreated Hall bar, after heating, after isopropanol treatment and after a second heating. (b) The curves after baking and isopropanol treatment from (a) normalized with respect to the Dirac point (V_{CNP}). (c) The 4-point longitudional resistance as a function of backgate voltage at 4K after heating and isopropanol treatment combined with heating measured at a magnetic field $B = 5\,\mathrm{T}$. The inset in (b) shows a scanning force micrograph (SFM) image of the measured Hall bar where the contacts hare highlighted in orange for clarity.

typically takes two days.

4.4.1 Room temperature transport experiments

In Fig. 4.4 (a) the conductivity (σ) of the Hall bar as a function of applied $\mathrm{V_{BG}}$ for the untreated sample (1), after only heating the sample (2), after treating the sample with isopropanol (3) and after heating the sample again (4) is plotted. It can be seen that both the mobility and the position of the CNP are changed significantly after the different treatments.

For the untreated sample the CNP is located at $+43\,\mathrm{V}$. The extensive doping of the pristine sample is probably due to water absorbed on the graphene surface and a combination of resist residues and other dopants accumulated during the processing steps. In order to remove as much as possible of these dopants we always bake our samples in vacuum in the sample holder before starting any transport measurements (as we also did before the functionalization in the previous section). Here it can be seen that after the initial baking of the sample the CNP has moved to $+26\,\mathrm{V}$. The corresponding change in mobility will be

discussed below. As a next step we immerse the sample in isopropanol. Fig. 4.4 (a) shows that the CNP is shifted from +29 V to +34 V in backgate after the isopropanol treatment, which demonstrates that isopropanol significantly p-dopes graphene. This doping effect is very similar to the doping effect of functionalization seen in the previous section.

From Fig.4.4(b), where the traces before and after isopropanol treatment from Fig. 4.4(a) are normalized with respect to V_{CNP}, it can in addition be seen that the isopropanol introduces a strong asymmetry between the electron and hole conductivities. The observed asymmetry after isopropanol treatment is larger than observed after the above functionalization (Fig. 4.3(b)). However, it is similar to the asymmetry found by Farmer et. al after chemically modifying the graphene lattice with diazonium chemistry where a slight reduction in mobility was also only found for one type of carriers [55]. The qualitative similarities between the changes in the conductivity of graphene after isopropanol treatment and the changes observed after functionalization suggest that with the functionalization procedure described above it might be difficult to separate the effects of the diazonium salt and the effects of isopropanol.

In the final step we heat the sample a second time in order to see if we can remove the dopants introduced by the isopropanol treatment. Surprisingly the Dirac point does not only shift back to +29 V where it was located before the isopropanol treatment, it shifts much further to +8 V. Not only are the dopants introduced by the isopropanol treatment removed, also additional dopants from previous processing steps are removed. Furthermore, the shift in the CNP towards zero backgate voltage is accompanied with a significant increase in the mobility. This suggests that treating the graphene only with isopropanol followed by heating has a "cleaning effect" on the graphene, resulting in an improved electronic quality. For measurement (1) and (3) (Fig. 4.4) it is difficult to extract the electron mobilities and thus only the hole mobilities will be compared in the following. For the untreated graphene flake (1) the hole mobility is determined to be 2100 cm^2/Vs. After the first heating step (2) the mobility has increased to 2700 cm^2/Vs. The following isopropanol treatment (3) increases the mobility further to 3600 cm^2/Vs and after the last heating (4) the mobility reaches 4700 cm^2/Vs. Generally we expect the introduction/removal of dopants to decrease/increase the mobility. Here, after the isopropanol treatment, an increase in hole mobility is observed together with an increased doping. This unexpected increase in mobility might be due to the removal of some dopants and the introduction of a different kind of dopants.

The fact that annealing the sample removes dopants and improves the mobility is generally accepted. Therefore baking is normally a part of standard processing procedures for graphene. However, that a subsequent treatment with isopropanol followed by annealing removes even more dopants has to our knowledge not been noted so far. The mechanisms behind this improvement is not completely clear. We speculate that chemical cleaning and heating remove different dopants with different efficiencies. In that case one can imaging that the first heating step removes a layer of dopants sensitive to heating. As a result dopants easily removed isopropanol will accessible for the solvent at the graphene surface. The removal of these dopants will then make dopants sensitive to heating beeing unprotected on the graphene surface. In such a scenario the alternating heating process and isopropanol treatment "peel off" different layers of dopants successively from the graphene surface.

In addition to the observed increase in sample quality after the combination of isopropanol treatment and heating the effect of the isopropanol treatment alone should also be pointed out. Isopropanol treatment alone leads to an increased p-doping and electron-hole asymmetry. These two effects are partly seen after chemical functionalization as well. Therefore it is important to be very careful when assigning shifts of the Dirac point and changes in electron-hole symmetry solely to the introduction of the modifying species.

4.4.2 Low temperature transport experiments

The quantum Hall effect and the corresponding magnetooscillations of the longitudional resistance is found in two-dimensional systems of high quality and at low temperatures. The quality of the quantum Hall effect is a direct measure for the quality of the electronic system. Therefore, in order to further investigate the influence of the isopropanol treatment and confirm the improvement of the electronic quality of the graphene, we perform transport measurements in a magnetic field at $T = 4\,\mathrm{K}$.

Fig. 4.4 (c) shows the four-point longitudional resistance (R_{xx}) of the flake as a function of V_{BG} at fixed magnetic field $B = 5\,\mathrm{T}$ after the first time heated (2) and after isopropanol treatment followed by the second heating (4). Before the isopropanol treatment R_{xx} does not go to zero in the quantum Hall states and only a weak splitting of the main resistance peak is observed. In contrast, after the isopropanol treatment and heating R_{xx} is clearly close to zero for filling factor $\nu = 2$. In addition several more oscillations in R_{xx} are visible.

These measurements show that the electronic quality of the graphene flake has indeed improved after treating it with isopropanol and heating it.

4.4.3 How clean can it get?

In the previous sections it has been shown that isopropanol treatment leads to a p-doping of the graphene similar to p-doping observed after functionalization. In addition a combination of isopropanol treatment and heating seems to remove dopants and increase the mobility of the device beyond the what is achieved with the initial heating step. From these two observations two important questions arise. How can the influence of solvents be controlled in future transport characterization experiments of functionalized graphene? And how much can the quality of the graphene devices be improved by a combination of isopropanol treatment and heating?

By repeating the isopropanol treatment followed by heating the shift of the CNP towards zero back gate voltage and the increase in mobility saturates. At this point a "stable state" is achieved where an isopropanol treatment will p-dope the grapehene and lower its mobility, but the following heating step will shift the CNP back to its original position before the isopropanol treatment and restore the mobility. Consequently, for further functionalization experiments this will be used as a starting conditions for the functionalization process. In addition each functionalization step will be followed by a heating step that should remove all dopants originating from the solvents. As a result we can assume that the observed doping and decrease in mobility when following this procedure should be caused only by diazonium moieties, either covalently bonded to the graphene lattice or adsorbed on the graphene surface, and not by any solvents involved in the reaction.

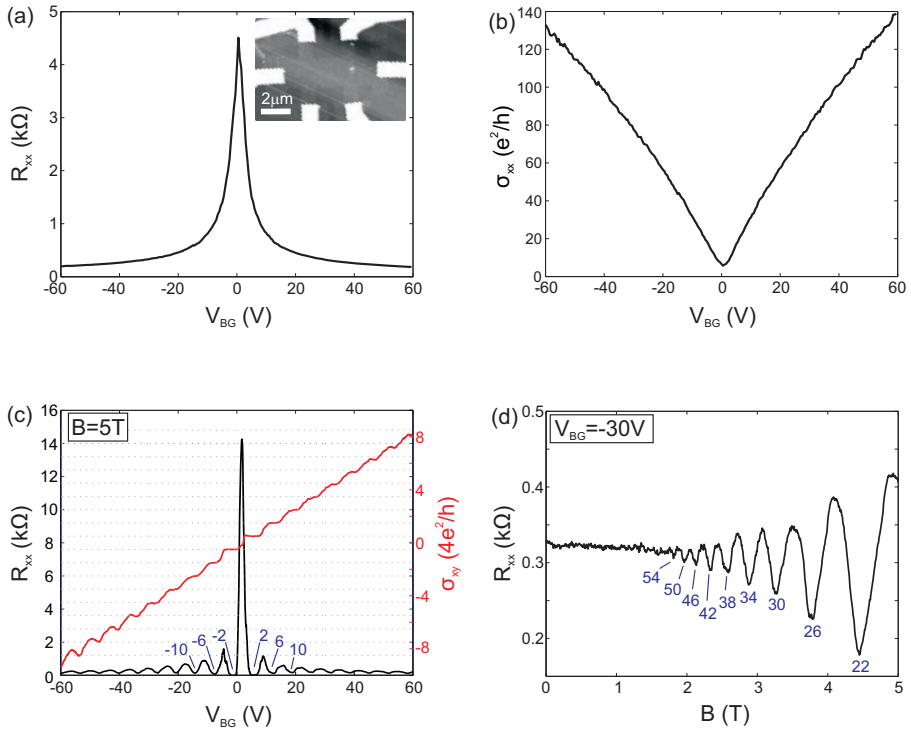

Fig. 4.5 — Transport measurements at 4 K of a Hall bar that is cleaned to the "steady state" condition suitable as a starting point for functionalization. (a) R_{xx} as a function of V_{BG} at zero magnetic field shows a sharp symmetric peak at +2 V in backgate. (b) The corresponding conductivity σ as a function of V_{BG}. (c) R_{xx} (black) and the Hall conductivity σ_{xy} (red) as a function of V_{BG} at a constant magnetic field of 5 T. The plateaus in σ_{xx} coincide nicely with the theoretically expected values marked with grey dashed horizontal lines. The first filling factors are indicated in blue. (d) R_{xx} as a function of magnetic field at a constant backgate voltage of 30 V. Nice Shubnikov-de Haas oscillations up to filling factor 54 are visible.

It should be noted the number of treatments needed to reach a "stable state" varies a lot from sample to sample. The dirtier the sample is initially, the more treatments are needed. If the sample is particularly clean, no isopropanol treatment is necessary, the heating alone will be sufficient.

For the devices investigated during this thesis we generally obtained a "stable state" with the CNP between -5 and 5 V in backgate voltage and a mobility of $\approx 10\,000\,\mathrm{cm}^2/\mathrm{Vs}$. A typical example of measurements of a Hall bar at a temperature of 4 K after reaching the "stable state" is shown in Fig. 4.5. In (a) the 4-point longitudional resistance R_{xx} as a function of V_{BG} can be seen. It shows a sharp, symmetric peak centered around the CNP which is located at +2 V in backgate. The inset depicts a SFM scan of the measured Hall bar. In Fig. 4.5 (b) the corresponding conductivity σ_{xx} is plotted. The minimum of conductivity has a value of $\sigma_{min} \approx 1.4\frac{4e^2}{h}$, which is close to the expected σ_{min} value of $\frac{4e^2}{h}$ for good quality graphene on SiO_2 [19]. From the Drude-Boltzmann expression for the conductivity at zero magnetic field $\sigma_{xx} = ne\mu$ the mobility is determined to be $9000\,\mathrm{cm}^2/\mathrm{Vs}$ at a density $n = \alpha V_{BG} = 1.5 \times 10^{12}\,\mathrm{cm}^{-2}$ where α is determined to be

$7.4 \times 10^10\,\mathrm{cm}^{-2}/\mathrm{V}$ from magneto transport measurements.

In Fig. 4.5 (c) R_{xx} (black) and the Hall conductivity σ_{xy} (red) as a function of V_{BG} at a magnetic field of 5 T are shown. The dotted, horizontal, grey lines mark the expected values for the quantum Hall plateaus for single layer graphene where $\sigma_{xy} = \pm 4(\nu + 1/2)e^2/h$ with filling factors $\nu = \pm 2, 6, 10, ...$ (marked in blue). The measured plateaus coincide nicely with the expected values. Furthermore, each minimum in R_{xx} corresponds well to a plateau in σ_{xy}. In Fig. 4.5 (d) R_{xx} as a function of magnetic field B is shown at a constant backgate voltage of -30 V. Nice Schubnikov-de Haas (SdH) oscillations up to filling factor 54 are visible, again demonstrating the high electronic quality of the device.

4.5 Summary

In this chapter first transport measurements of chemically modified graphene are shown. No significant change of mobility upon exposure to the diazonium reagent is observed, only a shift of the CNP to more positive backgate voltages, corresponding to an increased p-doping of the device. When treating the the device only with isopropanol, the solvent used to clean the sample after functionalization, a similar p-doping as for the functionalization itself is seen. These observations makes it clear that in order to study the influence on transport of the chemical functionalization, one first has to understand and control the influence of all solvents involved in the functionalization process.

Further systematic investigations of solvent effects shows that successive treatments with isopropanol followed by heating reproducibly remove dopants introduced by the solvents. This results in a "stable state" which is suitable as a starting point for functionalization. Furthermore, the ability to remove dopants from solvents by heating should be used after each functionalization step to make sure that the measured changes observed in doping and mobility of the device is only due to functionalization and not to solvent effects. The temperature used to remove doping from the solvents is not high enough to modify the functionalization itself.

Finally, the successive treatments with isopropanol followed by heating do not only result in a stable starting point for functionalization, they also generally "clean" the device to a reproducible good electronic quality.

Chapter 5

Functionalization of graphene Hall bars

In the previous chapter we focused on determining and controlling the effects of solvents, used in standard sample processing and standard chemical reactions, on the electronic properties of graphene. In this chapter a further step towards successful chemical modification of the graphene lattice is made. Graphene Hall bars are step-wise functionalized at room temperature and thoroughly characterized by electronic transport experiments and Raman spectroscopy measurements. From these complementary measurements information about the induced defect density and doping density is extracted and compared.

5.1 Experimental method

The devices are functionalized at room temperature by immersing the whole chip into a $20\,\mathrm{mmol\,l^{-1}}$ solution of water-soluble nitrobenzene diazonium salt (4-nitrobenzene diazonium tetrafluorborate) as discussed in section 4.2. Afterwards the chip is cleaned in isopropanol and blown dry with nitrogen. In the first functionalization step the chip is immersed for 1 minute. In the following 5 functionalization steps the immersion time is increased to 5, 20, 40 and 100 minutes respectively. Note that in the following we will refer to the total functionalization time which is then 1, 6, 26, 66 and 166 minutes respectively.

In the previous chapter it was shown that immersing a chip in pure water and isopropanol leads to a doping effect similar to the one expected from the functionalization itself. As discussed in chapter 4 we therefore first treat the graphene device only with isopropanol in combination with heating (around 100°C for approximately two days in vacuum). The Hall bars investigated here had a high initial quality with a mobility of $\approx 6000\,\mathrm{cm^2/Vs}$ already before any heating or isopropanol treatment. Therefore, already after the first heating step a mobility of $\approx 9000\,\mathrm{cm^2/Vs}$ and a charge neutrality point (CNP) at $\approx 0\mathrm{V}$ was obtained. The following isopropanol treatment lead to a p-doping that was removed by heating. However, no further increase in mobility beyond $9000\,\mathrm{cm^2/Vs}$ is observed. Another repetition of the isopropanol treatment followed by heating in vacuum did also not change the transport characteristics further. Consequently, a good starting point for functionalization is reached.

After each functionalization step the sample is heated in the sample holder in vacuum.

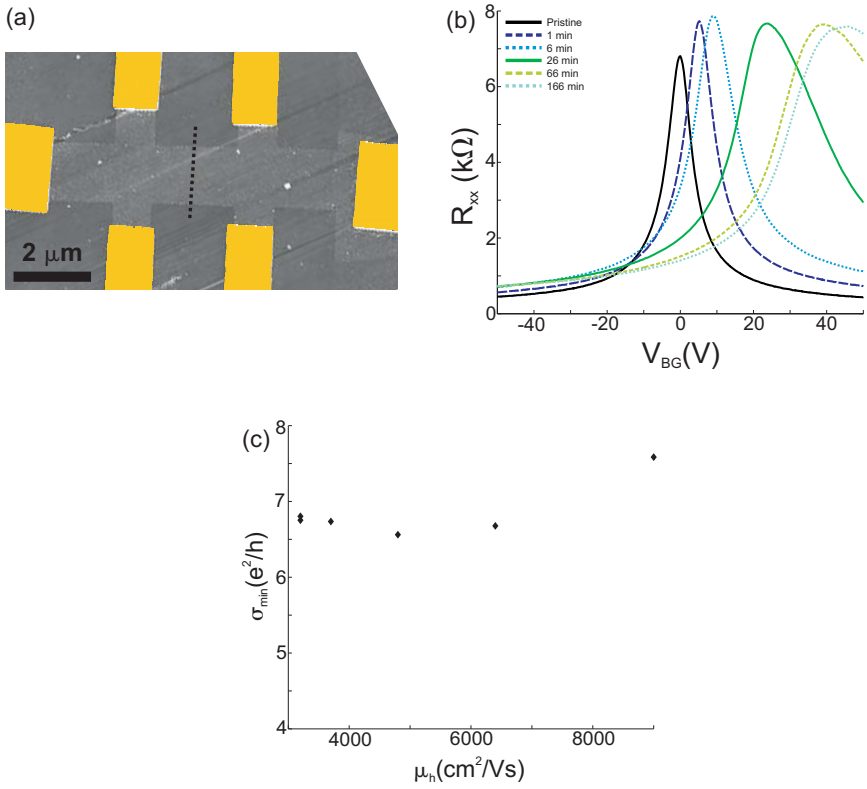

Fig. 5.1 — Room temperature measurements of functionalized graphene. (a) Processed single layer graphene flake with Hall bar shape and metal contacts (highlighted in yellow) (b) Backgate sweeps of the device in (a) after each functionalization step. (c) Minimum of conductivity versus mobility for the functionalization process.

The transport measurements are performed right afterwards without breaking the vacuum. From the discussion in chapter 4 we therefore assume that the doping observed in the following data is not due to solvent effects, but only due to diazonium moieties, either covalently bonded to or absorbed on the graphene surface. To complement the transport data the Hall bars were also thoroughly investigated by Raman spectroscopy after each functionalization step. The Raman spectroscopy measurements were always performed after the transport measurements and at ambient conditions. Consequently, some additional dopants, like water adsorbed from the air, might be present in the Raman data. The laser power was kept below 2 mW to avoid heating and laser induced defects.

Two Hall bars were measured in parallel in this study and the results obtained are qualitatively the same. In the following the measurements obtained from the Hall bar depicted in the inset in Fig. 5.1 (a) will be presented.

5.2 Transport measurements at room temperature

The transport measurements are performed by applying a constant current of 10 nA through the Hall bar while measuring the 4-point longitudional resistance (R_{xx}) and transverse resistance (R_{xy}). In Fig. 5.1(b) R_{xx} is shown as a function of applied backgate voltage (V_{BG}) after the different functionalizaton steps. For the untreated Hall bar the charge neutrality point (CNP) is at 0 V in backgate and the hole mobility μ_h is determined to be 9000 cm^2/Vs at a density of $1.6 \times 10^{12}\,cm^{-2}$, indicating low initial doping and high quality (similar to the Hall bar presented in section 4.4.3). Since the electron mobility cannot be reliably determined for long functionalization times, only hole mobilities will be considered in the following. For each functionalization step the CNP moves to more positive backgate voltages and the mobility decreases, as can be seen by the increased width of the resistance peak. After 166 minutes of functionalization the CNP is at 45 V and the mobility is decreased to 3200 cm^2/Vs. It is worth noticing already at this point that this is comparable to normally observed mobilites for untreated devices with the CNP at similar back gate voltages due to unremoved dopants from the fabrication steps.

The observed shift of the CNP can be explained by the functional group either attached to or adsorbed on the graphene structure. In both cases the functional group acts as a hole dopant. The nitro-benzene group is an electron acceptor, removing electrons from graphene [56], therefore shifting the CNP to more positive backgate potentials. The doping contribution of one perpendicularly oriented nitrobenzene molecule to graphene can be roughly estimated by the dipole moment (4-Nitrobenzene $\sim$ 4.5 D (Debye)) and the assumption of a distance between the graphene plane and the chemical group ($d \sim 0.5 - 1$ nm). This evaluation leads to a removal of around 0.05 to 0.2 electrons/nitrobenzene molecule from the graphene plane. In case of adsorbed species an estimation of the electrons/nitrobenezene removed is harder, as the final conformation is generally unknown and multilayer adsorption is possible. In general the adsorbed species are closer to the surface and can build charge transfer complexes, therefore more electrons/molecule can be removed from graphene than in the covalently attached case.

The observed change in mobility can also be a result of both induced defects and of charged impurities close to the graphene surface acting purely as dopants. This has been shown in several previous reports dealing with potassium atoms as dopants [25], defects through ion irradiation [27], polymers as dopants [55] or defects through covalently bound molecules [55, 57] on the surface of graphene.

To further understand the measurements presented in Fig. 5.1(b) and to differentiate between the effect of the functional groups as defects or as dopants we plot the minimum conductivity (σ_{min}) as a function of mobility for all the functionalization steps. Previously it has been shown by Chen et. al in [27] that σ_{min} decreases with decreasing μ when defects are induced in the graphene lattice. However, when only dopants are introduced the σ_{min} stays constant. Here it can be seen that σ_{min} decreases slightly from pristine graphene (high mobility) to after the first functionalization step. After further functionalization steps it hardly changes anymore. Following the results of Chen et al. a significant number of defects are only introduced to the graphene lattice during the first functionalization step. And the continuous decrease in mobility observed after each functionalization step is mainly du to doping.

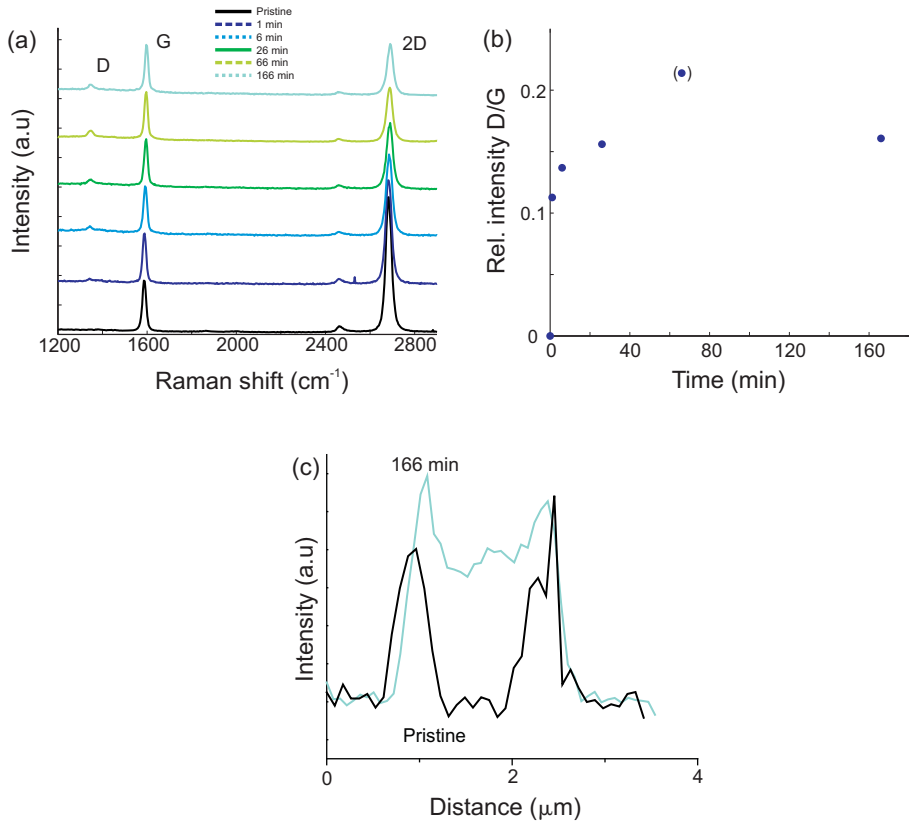

Fig. 5.2 — (a) Raman spectra of the graphene device after each functionalization step. (b) The intensity of the D line relative to the intensity of the G line as a function of functionalization time. (The measurement point after 66 min of functionalization was carried out with a different measurement setup than the other points and is therefore not considered.)(c) Raman line scans over the cross section of the Hall bar device (See dotted line in Fig. 5.1(a)) showing the D peak area as a function of spatial location for the pristine device and after the last functionalization step.

5.3 Raman spectroscopy

In addition to electronic transport experiments also Raman spectroscopy is used to investigate the changes of the graphene during functionalization. Fig. 5.2(a) shows the Raman spectra of the Hall bar after each functionalization step. Three main peaks can be seen, the D-peak (due to defects), the G-peak and the 2D-peak [38]. For pristine graphene no D-peak is observed. After functionalization a small D-peak occurs, showing that some defects in the graphene lattice are indeed created. However, as can be seen more clearly in Fig. 5.2 (b) where the intensity of the D peak realtive to the intensity of the G peak as a function of functionalization time is plotted, the D peak intensity only increases until 26 minutes functionalization time and then it saturates, confirming that defects are only induced in the first functionalization steps. The measurement point after 66 minutes of functionalization shown in Fig. 5.2 (b) is not considered due to a different measurement setup.

In addition to the appearance of the D-peak, a continuous shift of the G-peak to higher wavenumbers and a decrease in G/2D ratio is observed for increased functionalization times, both known effects of doping [48, 47]. These doping effects increase until the last functionalization step, thereby demonstrating that the amount of dopants on the graphene continues to increase after no additional defects are created. This agrees with the previous understanding of the transport data where doping is the dominant effect seen from the functionalization.

From the ratio of the D-peak and the G-peak a rough estimate of the distance between the attached functional groups and hence their density can made by the empirical formula $L_a(\text{nm}) = (2.4 \times 10^{-10})\lambda^4(I_D/I_G)^{-1}$ [42]. Lucchese et al. reported a slightly modified formula, where $(1/L_a)^2 \sim I_D/I_G$, for small I_D/I_G ratios both formulas yield similar L_a values [44]. After 166 minutes of functionalization we calculate L_a to be $\sim 30\,\text{nm}$. This corresponds to a defect density of $\sim 10^{11}\,\text{cm}^{-2}$. From the position of the CNP after 166 minutes of functionalization we estimate a doping density of $\sim 10^{12}\,\text{cm}^{-2}$, which is one order of magnitude larger than the estimated defect density.

Previous Raman spectroscopy studies of graphene functionalized with diazonium salt has shown a large reactivity of the graphene sheet towards the diazonium reagent [11, 45, 54]. In this study a rather small reactivity is observed, however, a large doping effect is seen. One likely explanation for this is the formation of dendritic polymers [58]. These polymers may have one or few monomers covalently attached to the graphene plane, therefore showing only a small D peak. However, the whole polymer may contribute to the doping, as it can adsorb to the graphene surface. The adsorption of nitrobenzene groups has previously been shown to p-dope without establishing a D peak [45]. In addition the adsorbed species may remove more electrons/functional group as they can interact by π-stacking, resulting in charge transfer complexes on the graphene surface. The observed doping can also be a result of diazonium species adsorbed on the surface without being part of a polymer structure. However, this is not very likely due to the thoroughly rinsing of the chip in isopropanol after the functionalization followed by heating it in vacuum for two days as described before.

Earlier reports have also shown a significantly larger reactivity of graphene edges compared to bulk towards diazonium chemistry [11, 45]. This is in strong contrast to the functionalized and measured devices here. In Fig. 5.2(c) line scans of the D-line intensity are shown over the cross section of the Hall bar devices (See dotted line in Fig. 5.1(a)). From these scans no preferential differences between edge and bulk are observed at any time during the functionalization, beside the naturally occurring D-line between edge and bulk graphene, due to symmetry breaking at the edge. This observed difference between previous studies and this study is most likely due to differences of the edges of unprocessed graphene and etched graphene structures. In the previous Raman studies unpatterned graphene flakes were investigated, while we functionalize contacted and patterned Hall bars. The reactive ion etching which is used to define the Hall bars results in chemically undefined graphene edges which can differ from the edges of unprocessed graphene and may lead to a lower reactivity.

The low induced defect density and high doping in this study could be an indication that the reaction conditions favored building polymeric structures on the graphene surface rather than binding directly to the surface. However, it should be noted that the

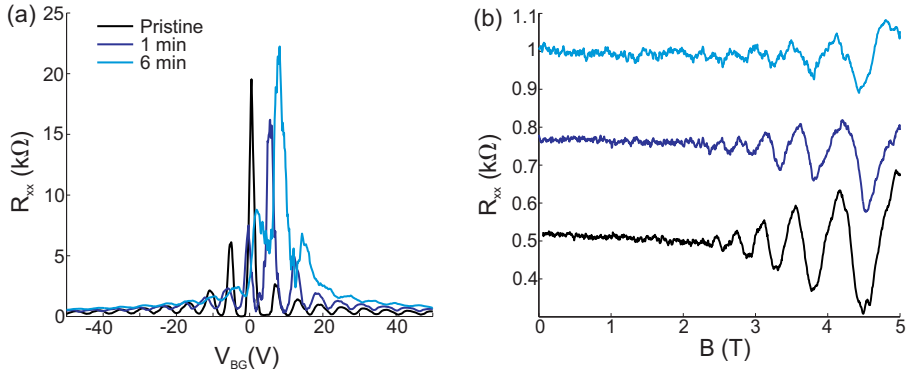

Fig. 5.3 — (a) R_{xx} as a function of V_{BG} at $B = 5\,\mathrm{T}$ for the untreated graphene and the two first functionalization steps. (b) B-field dependence of R_{xx} at $\Delta V_{BG} = -30\,\mathrm{V}$.

low defect density might also be related to resist and other residues partly covering the graphene sheet after contacting and pattering the Hall bars reducing the area available for functionalization. So far a high reactivity towards the diazonium chemistry has primarily been shown on non-processed graphene flakes [11, 45]. On contacted graphene flakes also a previous study has shown mainly doping effects in the bulk [55]. Only recently Zhang et al. showed on contacted (not etched by reactive ions) graphene samples that the addition of tetrabutylammonium hexafluorophosphate during the functionalization increases the reactivity towards the graphene surface, allowing to create more defects in the graphene plane [54]. However, the dopant concentration due to functionalization is significantly lower than what is observed in this work.

5.4 Transport measurements at 4K

To further investigate the influence of chemical functionalization on electronic transport we also performed transport measurements at a temperature of 4 K and a magnetic field up to 5 T. In Fig. 5.3(a) R_{xx} as a function of V_{BG} at 5 T is shown for the pristine device and after the first two functionalization steps. For the pristine device clear magnetooscillations can be seen, confirming the high quality of the untreated device. For increasing functionalization time the oscillations are washed out. After the third functionalization step the mobility is lowered to $3700\,\mathrm{cm}^2/\mathrm{Vs}$ (see Fig. 5.1(c)) and no oscillations are visible anymore. This is consistent with previous measurements of untreated devices of different mobilites.

In Fig. 5.3(b) the corresponding Schubnikov-de Haas oscillations measured at a density of $2.4 \times 10^{12}\,\mathrm{cm}^{-1}$ can be seen. The oscillations can be described by

$$\rho_{xx} = \frac{m}{ne^2\tau_D}[1 - 2e^{-\pi/\omega_c\tau_q}\frac{2\pi^2 k_B T/\hbar\omega_c}{\sinh(2\pi^2 k_B T/\hbar\omega_c)}\cos(\frac{j\pi hn}{2eB} - \phi)] - aB - bB^2 \qquad (5.1)$$

where $\omega_c = eB/m$ is the cyclotron frequency, $m = \hbar k_F/v_F$ is the cyclotron mass, and the two last terms describe the slightly decreasing background [59]. For graphene the

phase ϕ is π and $j = 1$ [60]. By fitting the measurements shown in Fig. 5.3 (b) with Eq. 5.1 the quantum scattering times τ_q and the Drude scattering times τ_D for the different functionalization steps are extracted. For the untreated graphene Hall bar we find $\tau_D = 181\,\text{fs}$, $\tau_q = 67\,\text{fs}$ and $\tau_D/\tau_q = 2.7$. Correspondingly we find $\tau_D = 120\,\text{fs}$, $\tau_q = 47\,\text{fs}$ and $\tau_D/\tau_q = 2.55$ after 1 min functionalization and $\tau_D = 95\,\text{fs}$, $\tau_q = 38\,\text{fs}$ and $\tau_D/\tau_q = 2.5$ after 6 min functionalization. From the fit a statistical uncertainity of ± 0.1 for τ_D/τ_q is obtained. In addition, a significant systematic error is present, however, the trends extracted are not affected by this. Both τ_D and τ_q decrease significantly with increasing functionalization time while their ratio τ_D/τ_q decreases only slightly. From τ_D/τ_q the nature of the induced scattering, long range or short range, can be extracted. A large ratio means that scattering is mainly in the forward direction, a result of long range scatterers, while $\tau_D/\tau_q \approx 2$ is a signature of short-range scatterers [61]. The τ_D/τ_q ratios reported here are comparable to previously found ratios [60, 62] and suggest that charged impurities close to the graphene sheet contribute most dominantly to scattering [63]. The fact that the individual scattering times τ_D and τ_q decrease significantly with functionalization while their ratio hardly changes, and the fact that the ratio obtained here is comparable to other pristine devices, is again an indication that the here performed functionalization introduces scatterers for transport similar to dopants present from normal processing of samples.

5.5 Summary

Step-wise functionalized graphene Hall bars were thoroughly characterized by both Raman spectroscopy and transport measurements at room temperature and 4 K. The Raman spectroscopy data show that only few defects are introduced to the graphene structure. In addition, from both Raman spectroscopy measurements and transport measurements a clear doping effect, exceeding the number of covalently bound moieties by one to two orders of magnitude, is seen. This suggests that the chemical reaction results in few covalently bounded species, which then serve as seeds for a polymer like growth using the diazonium ions as monomers.

It is not quite clear why only few defects are created in this study. One explanation might be that the graphene device was partly covered with resist residues from the processing steps that we were not able to remove, resulting in a small effective area available for functionalization. Hence, it would be desirable to have even cleaner graphene as a starting point for future functionalization experiments. Furthermore, patterning and contacting a device allows for less flexibility of the graphene lattice, something which might lower the reactivity compared to a bare flake on a substrate. Finally, it has been suggested in a similar study that surfactants that help bringing the cationic diazonium compounds close to the highly hydrophobic graphene structure are needed to obtain a high reactivity[54]. However, a systematic study of the influence of surfactants are still needed.

Part II

Transport in three-terminal graphene junctions

Chapter 6

Rectification in three-terminal graphene junctions

One important reason why graphene has attracted such a huge interest during the last couple of years is its high mobility. The high mobility persists all the way up to room temperature [15], making graphene an excellent candidate for the next generation of electronic devices. However, the lack of a band gap make it difficult to realize conventional graphene transistors. One alternative solution is to exploit the novel electronic properties of a new class of nano-scale devices, three-terminal junctions. The main property of these junctions are a nonlinear rectifying behaviour [64–66]. When a symmetric bias is applied to two of the leads a finite voltage is measured at the third lead. This is in contrast two an ideal ohmic device where the voltage measured at the central branch is half the voltage-difference between the two biased branches, which in a case of a symmetric bias would be zero.

This non-linear rectifying behaviour has recently been observed in a wide variety of material systems ranging from III-V semiconductor heterostructures [65, 67, 68] to InAs nanowires [69] and carbon nanotubes [70]. Furthermore, a number of operational devices, such as frequency multipliers [71], logic gates [72, 73], set-reset latch device [74] half and full adders [75, 76], has recently been demonstrated based on nonlinear electrical properties of three-terminal ballistic junctions. The operation speed of such devices is predicted to be in the THz range [77].

Ballistic switches and rectifiers in graphene represent another fascinating possibility to realize high quality electronic nanostructures. In addition to the previously mentioned high charge carrier mobilities which make graphene promising for ballistic electronics, the possibility to electrically or environmentally tune graphene from p- to n-type and vice versa [78] offers the opportunity to design adaptive electronic devices [79]. Although theoretical proposals have been made for building blocks for integrated graphene circuits [80], none of the nanodevices mentioned above has been realized in graphene so far.

In this chapter we will present the first realization of a three-terminal graphene junction and investigates its nonlinear electrical properties.

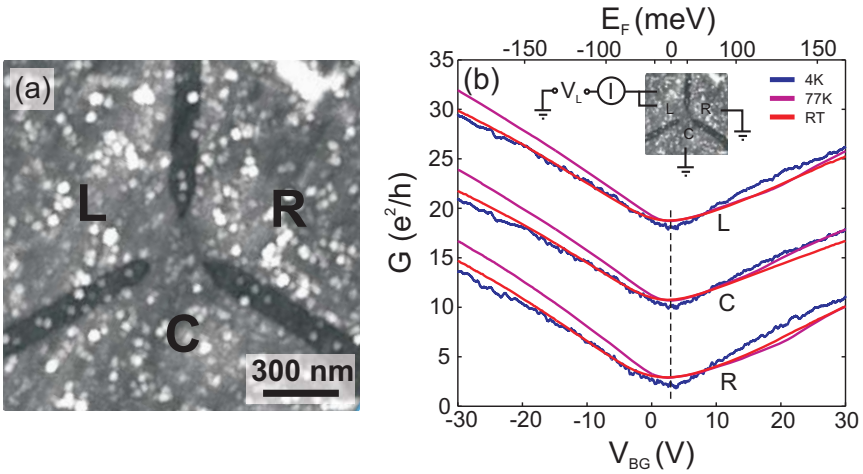

Fig. 6.1 — (a) Scanning force micrograph (SFM) of the center part of the three terminal junction. The three constrictions, labeled L, R and C, separating the center part of the junction from the leads are all $\approx 200\,\mathrm{nm}$ wide. (b) Conductance of each of the three constrictions (other two branches grounded) as a function of backgate voltage measured at 4 K (blue), 77 K (pink) and room temperature (red). The curves of the different constrictions are vertically offset by $8e^2/h$ for clarity. The electrical measurement configuration is shown in the inset.

6.1 Sample

In Fig. 6.1(a) a SFM image of the center part of the investigated three-terminal junction is depicted. The leads, labeled L (left), R (right) and C (center) are separated by three $\approx 200\,\mathrm{nm}$ wide constrictions. The angle between each branch of the junction is approximately 120 degrees. Thus, the device rotationally symmetric and can be measured in three comparable configurations in the non-linear transport regime (see measurement configuration below). To characterize the junction the conductance (G) of each constriction is measured as a function of the applied backgate voltage (V_{BG})at 4 K, 77 K and room temperature in the linear response regime as shown in Fig. 6.1(b). The electrical measurement configuration corresponding to the measurement of the conductance of the left constriction is shown in the inset. The Fermi energy calculated from the backgate voltage by assuming a density of states linear in energy is plotted as the upper horizontal axis. The point of minimum conductance, the charge neutrality point CNP, is located at approximately +3V in backgate (see the dashed line in Fig. 6.1(b)) and the Fermi energy is set to be zero at this point. To the left of the CNP the charge carriers are holes and to the right we have electron transport. Thus, by changing V_{BG} we can tune the device from p-type to n-type. At 4 K reproducible universal conductance fluctuations (UCF) are visible. At 77 K and room temperature the UCF are smeared out and the conductance curves are smooth. The conductance of each of the constrictions is similar suggesting that the device is close to symmetric. From the conductance curves we estimate the mobility of the junction to be $\approx 4000\ \mathrm{cm}^2/\mathrm{Vs}$ and the corresponding mean free path to be $\approx 70\,\mathrm{nm}$. Thus, the device can be considered to be diffusive.

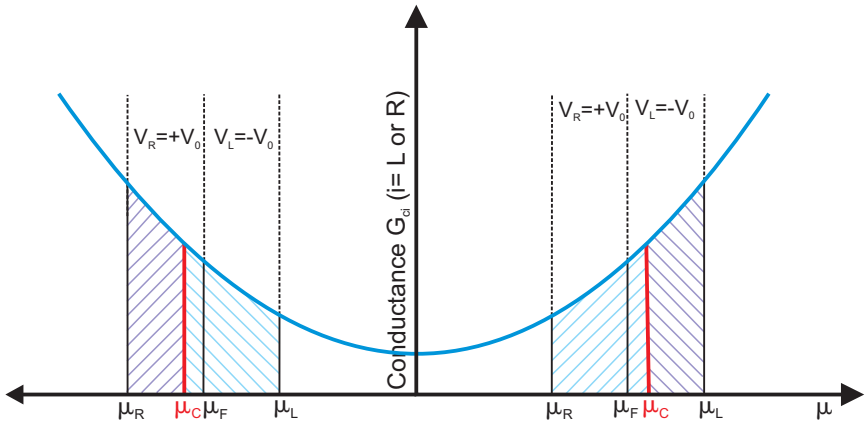

Fig. 6.2 — A schematic picture which explains how the finite center voltage arise when a push-pull bias ($V_\mathrm{L} = -V_\mathrm{R} = V_0$) is applied to the device. The change of sign of the voltage rectification when changing from electron transport to hole transport is also illustrated. The sign of V_C is independent of the relative signs of V_L and V_R.

6.2 Model

In previous measurements and calculations it has been shown that for a symmetric III-V-based three-terminal ballistic junction in the non-linear regime the voltage on the center branch (V_C) is always negative when the bias voltages at the left and the right branches are applied in a push-pull fashion with $V_\mathrm{L} = -V_\mathrm{R} = V_0$ [64, 65, 67]. For a graphene three-terminal junction we expect the voltage on the center branch to always be negative for electron transport and always be positive for hole transport, independent of the relative signs of V_L and V_R. This is schematically explained in Fig. 6.2. The conductance from the left branch to the central branch and the conductance from the central branch to the right branch increase with increasing chemical potential μ. When a push-pull bias is applied the chemical potential of the right branch is $\mu_\mathrm{R} = \mu_\mathrm{F} - eV_0$ and the chemical potential of the left branch is $\mu_\mathrm{L} = \mu_\mathrm{F} + eV_0$. For electron transport the area A_L under the conductance curve between μ_C and μ_L represents the electron flow from the left branch into the central branch and correspondingly the area A_R between μ_R and μ_C represents the electron flow from the central branch to the right branch. Since the current flowing into the junction has to be equal to the current flowing out, and there is no net current flowing into or out of the central branch, A_L and A_R have to be equal. As a result the voltage at the center branch will always be negative. Correspondingly it can be seen that for holes the voltage at the center branch will always be positive. Following the same arguments we expect V_C as a function of applied push-pull voltage V_0 to bend down for electrons and up for holes. It should be noted that in this model the rectification effect is a result of the change in conductance of the device when the Fermi energy is changed. Therefore we expect the rectification to be visible in graphene also for diffusive transport.

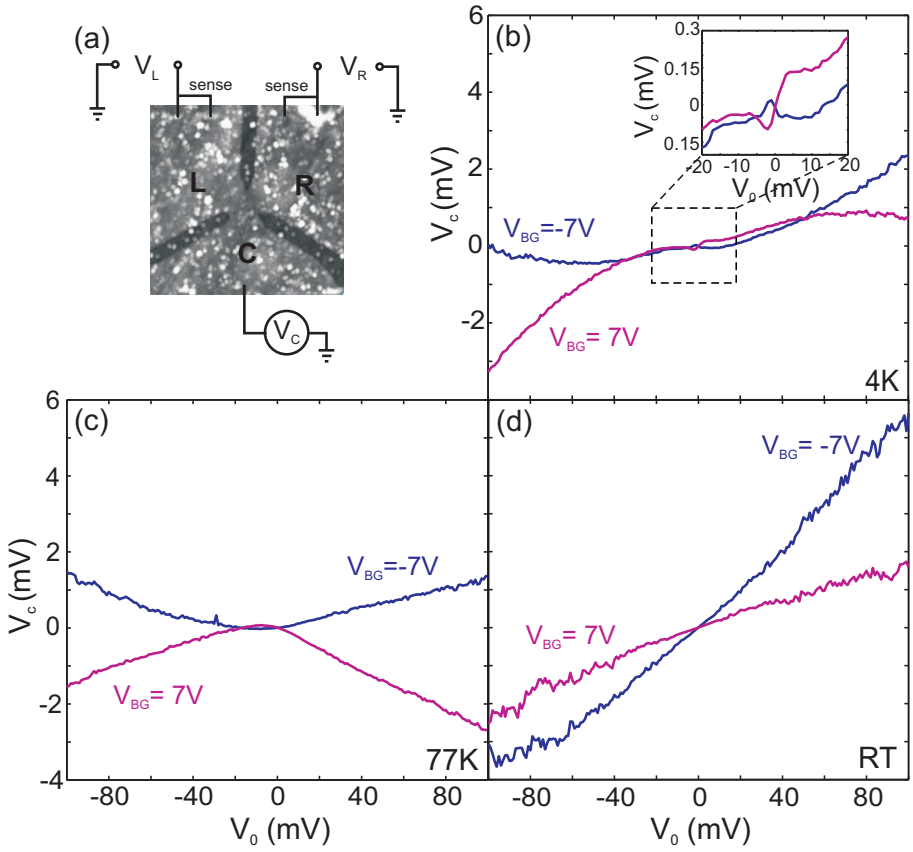

Fig. 6.3 — (a) The electrical measurement setup used in the non-linear regime. A push-pull bias voltage is applied to the left and the right branch while the voltage at the center branch V_C is measured. (b)-(d) V_C as a function of V_0 for $V_{BG} = +7\,V$ and $V_{BG} = -7\,V$ at 4 K, 77 K and room temperature respectively. A clear bending up for hole transport and bending down for electron transport is observed up to room temperature.

6.3 Rectification

The measurement circuit used to investigate the voltage rectification properties of the three-terminal junction in the non-linear response regime is shown in Fig. 6.3(a). In order to avoid the effects of contact resistances and to ensure that the bias voltage is always applied symmetrically to the device we have two contacts at each branch of the junction and use the sense function of the DC voltage source to monitor the potential at one contact and apply the potential at the second contact. The V_0 voltages plotted in Figs. 6.3(b)-(d) are the measured voltages and not the applied voltages, which are larger since they partially drop across the contacts. With this setup we also eliminate possible non-linearities of the contacts themselves. When the push-pull bias voltages are applied to the left and the right branches without using using the second pair of contacts to make sure that the voltage drop over the junction is symmetric, random nonlinearities in the center voltage were observed. These non-linearities, which we assume arise from the non-perfect contacts, were generally stronger than the nonlinearities later observed with the

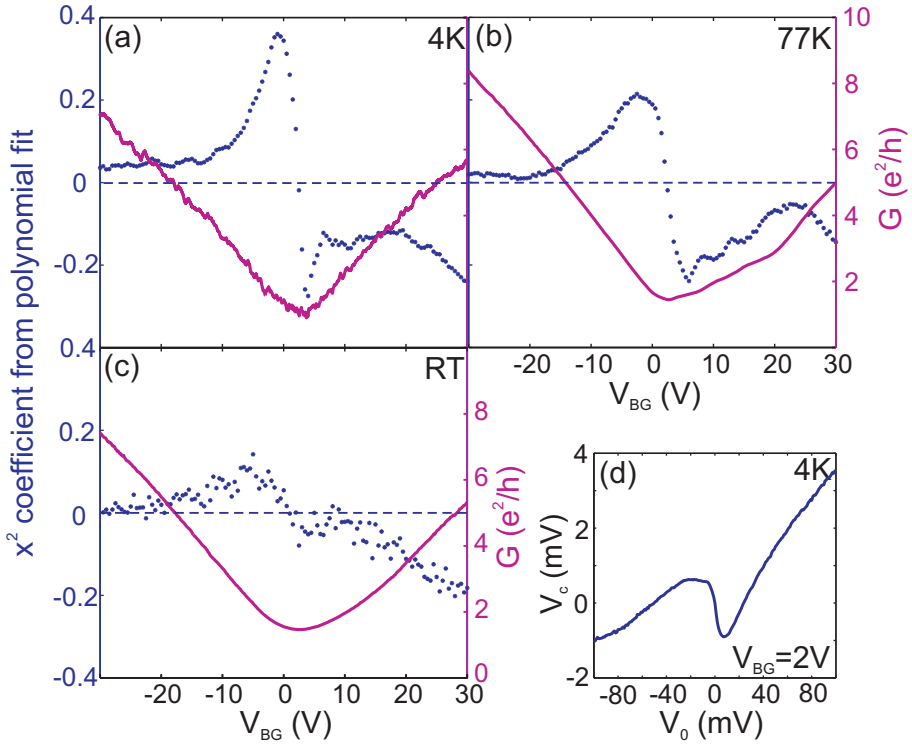

Fig. 6.4 — (a)-(c) The second-order coefficients obtained from fitting V_C vs V_0 with a third order polynomial (blue dots) and conductance from left to right (pink line) as a function of V_{BG} at 4 K, 77 K and room temperature respectively. (d) V_c vs V_0 close to the Dirac point.

sense-method. Thus, in a crude two-terminal measurement such non-linearities will mask any nonlinearity of the device. Therefore, in order to observe the real nonlinearities of the three-terminal junction a measurement setup as described above is essential.

Figs. 6.3(b)-(d) show the measurement of V_C as a function of V_0 for backgate voltages +7 V (electrons) and -7 V (holes) at 4 K, 77 K and room temperature, respectively. As a general trend we see that V_C as a function of V_0 always bends down for $V_{BG} = +7\,V$ and always bends up for $V_{BG} = -7\,V$. At 4 K additional kinks can be seen in the curves for $|V_0| < 20\,mV$ (see the inset in Fig. 6.3 (b)). This is most likely a result of universal conductance fluctuations (UCF) as theoretically predicted [81]. The linear part of V_C as a function of V_0 is due to the asymmetry of the device, which strongly depends on V_{BG}.

6.3.1 Backgate dependence

In the following we will have a closer look at the backgate dependence of the rectification signal. From the simple model shown in Fig. 6.2 it is expected that the V_C vs V_0 curves always bend down for electrons and bend up for holes as confirmed in Figs. 6.3(b)-(d). However, it is also expected that the magnitude of curvature will decrease with increasing Fermi energy. The further the device is tuned away from the CNP the weaker the curvature is since the relative difference between the conductances left and right of the junction

gets smaller compared to the overall conductance. In Figs. 6.4(a)-(c) the magnitude of curvature (blue dots) and the conductance from the left lead to the right lead (pink curve) are plotted as a function of V_{BG} at 4 K, 77 K and room temperature, respectively. Here we have defined the magnitude of curvature as the second-order coefficient obtained from fitting the V_C vs V_0 curve with a third order polynomial. It can be clearly seen that for holes the curvature is positive and for electrons it is negative, in agreement with the individual measurements shown in Figs. 6.3(b)-(d). Measuring the device in any of the two other possible measurement configurations gives qualitatively the same results. For holes it can be seen that the magnitude of curvature decreases while going to higher charge carrier densities as expected, however for electrons the curvature first decreases and then increases with increasing charge carrier density. We attribute this to inhomogenities in the sample leading to different charge neutrality points at different locations in the sample and therefore a mixture of electron and hole transport. This is supported by the kinks seen in the G vs V_{BG} curves, for instance the kink at approximately +20 V backgate in Fig. 6.4(b). In addition it can be seen that as a general trend the magnitude of curvature decreases with increasing temperature, which is due to thermal smearing around the Fermi energy. Close to the Dirac point the V_C vs V_0 curves cannot be fitted well. This is presumably because of electron-hole puddles and strong disorder (see the example depicted in Fig. 6.4(d)) [82].

6.4 Summary

We have observed voltage rectification up to room temperature in a diffusive three-terminal graphene junction when operated in the non-linear transport regime. Tuning the device from electron to hole transport the sign of rectification is switched.

For the measurements presented here a voltage rectification of a few percent is obtained. According to our model the amount of rectification increases when the Fermi energy decreases and the difference in relative conductance between the left and the right constriction increases. To improve the rectification properties of the nanojunctions one possibility is therefore to make the devices smaller in order to open a transport gap and then tune the Fermi energy to a point close to the gap.

Chapter 7

Weak localization, universal conductance fluctuations and mapping of the disorder potential in graphene

In the previous chapter non-linear electrical properties of graphene three-terminal junctions were investigated where voltage rectification with potential for electronic applications was observed up to room temperature. In this chapter the device introduced in the previous chapter will be further used to investigate universal conductance fluctuations (UCF) and weak localization (WL) in graphene. These are well known interference effects that have become important tools to investigate electron dephasing in mesoscopic devices. Furthermore, at the end of the chapter, the special three-terminal structure will be used to probe the disorder potential of the graphene device.

7.1 Weak localization

7.1.1 Introduction

Quantum interference corrections to the classical Drude resistivity have been extensively studied in conventional 2DEGs for decades [83]. Lately also the first studies of interference effects in graphene have been performed [84–88]. Two prominent examples of such effects are weak localization and universal conductance fluctuations. Here we will first consider WL and UCF will be discussed in the next section.

Weak localization is the result of enhanced backscattering due to the constructive interference of time-reversed electron paths. In a diffusive system an electron will not move along a straight line, its trajectory will constantly change direction due to random scattering off several scattering sites. Fig. 7.1 shows the special situation of two electron waves propagating in opposite directions along the same trajectory and interfering at the point of intersection. Since the two paths are identical, the two waves will have acquired the same phase along the trajectory and the interference will be constructive. This increased backscattering probability leads to an increase in the resistance of the sample, which is

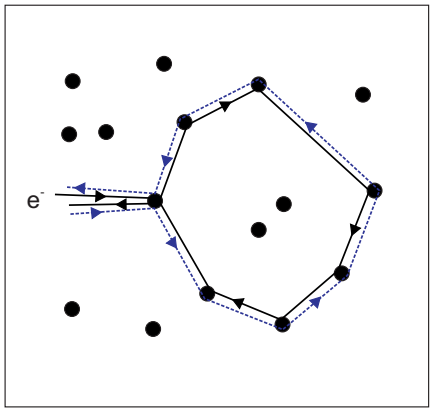

Fig. 7.1 A two-dimensional diffusive sample where electrons scatter off scattering sites (black dots) while moving through the sample. The weak localization effect arises due to time-reverse paths which interfere constructively and therefore lead to enhanced backscattering as illustrated by the black solid path and the blue dashed path.

known as the weak localization effect. Experimentally the most convenient way to detect this increased backscattering is by applying a small perpendicular magnetic field which induces a phase difference between the two electron waves and thus destroys the interference.

In conventional two-dimensional systems WL is controlled only by inelastic electron scattering or scattering by magnetic impurities [86]. For graphene this is not the case. The chirality of the charge carriers in graphene, a direct result of the honeycomb lattice structure, leads to WL that is not only sensitive to inelastic phase breaking scattering processes (characterized by the phase coherence length L_ϕ), but also to different elastic scattering processes [89]. The graphene band structure has two valleys, and there are two types of so-called *intravalley* elastic scattering processes (described by the intravalley scattering length L_*) that suppress the interference within one valley. First, scattering on defects with the size of the lattice spacing break the chirality of the charge carriers, thus suppressing interference. Second scattering on dislocations and ripples produce an effective random magnetic field that also destroys the interference [90]. In addition *intervalley* elastic scattering processes (described by the intervalley scattering length L_i) have to be taken into account. These scattering processes, originating from the scattering off sharp defects (like for instance the edges of the sample), actually restore the suppressed interference originating from the intravalley scattering processes by mixing the two valleys.

From these considerations it follows that the magnetroresistance correction of single layer graphene $\Delta\rho(B) = \rho(B) - \rho(B = 0)$ is given by [89]

$$\Delta\rho(B) = -\frac{e^2\rho^2}{\pi h}\left[F\left(\frac{B}{B_\phi}\right) - F\left(\frac{B}{B_\phi + 2B_i}\right) - 2F\left(\frac{B}{B_\phi + B_i + B_*}\right)\right] \tag{7.1}$$

where $F(z) = \ln z + \psi(0.5 + 1/z)$, $B_{\phi,i,*} = \hbar/4eL^2_{\phi,i,*}$. It can be seen from Eq. 7.1 that depending on the relationship between L_ϕ, L_i and L_* both the conventional positive correction to the magnetoresistance, weak localization, and a negative correction to the magnetoresistance, weak antilocalization (WAL), can be observed [89]. It should be noted that the WAL expected in graphene is very different from the WAL that has been observed in two-dimensional systems with strong spin-orbit coupling where spin-flips due to the scattering on impurities destroy the interference [91, 92].

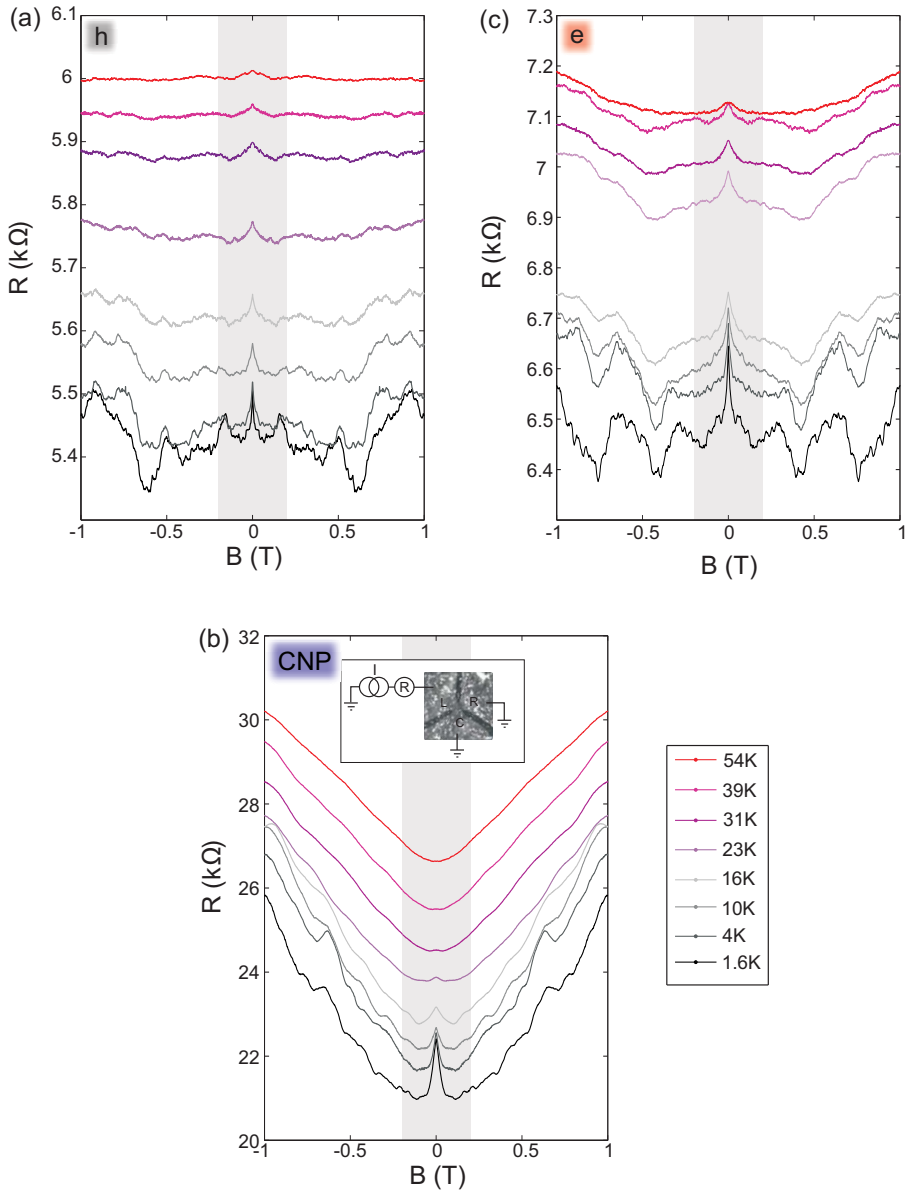

Fig. 7.2 — Resistance as a function of magnetic field for different temperatures from 1.6K̇ to 54 K in (a) a region of hole transport, (b) close to the CNP and (c) in a region of electron transport. All traces are symmetrized and averaged over 1 V in backgate voltage. (In (a) V_{BG} is -39 to -40 V, in (b) V_{BG} is 4 to 5 V and in (c) V_{BG} is 49 to 50 V.) For better visibility the curves at different temperatures are offset by 100 Ω ((a) and (c)) and 1 kΩ (b). The inset in (b) shows the measurement setup where a constant current of 100 nA is applied between the left terminal and the two other terminals. The total resistance is measured.)

7.1.2 Measurements

The presence of WL in graphene has been shown in several previous studies on both mechanical exfoliated graphene [84, 86, 90, 87] and epitaxial graphene [85]. In an early report

by Morozov et al. it is shown how low quality due to for instance ripples of the graphene sheet leads to a strong suppression of WL, while for higher quality graphene WL is recovered [84]. Later studies have systematically investigated WL as a function of both charge carrier density and temperature and the origin of the different scattering mechanisms have been discussed [86, 87]. The expected transition from WL to WAL has also been recently observed experimentally in a study by Tikhonenko et.al [90]. All previous studies have been performed on large (W and L $> 2\,\mu$m) or rectangular shaped samples. Here we investigate WL in a very special graphene structure, a three-terminal junction where the constrictions defining the center of the junction are only about 200 nm wide. The small size might lead to slightly different relationships between the different scattering rates of the system, which should influence the WL effect. For instance, enhanced scattering at the edges is expected to decrease intervalley scattering.

The magnetoresistance of the three-terminal junction is measured as shown in the inset in Fig. 7.2(b). A 100 nA constant current is applied between the left terminal and the two other terminals and the total resistance is measured. At low temperatures reproducible UCF (which will be discussed in detail in the next section) are present as a function of magnetic field in addition to WL. In order to study the magnetoresistance arising only from WL we measure the resistance R as a function magnetic field B for five different of backgate voltages within a backgate voltage range of 1 V and average. In Fig. 7.2 the symmetrized and averaged resistance R is plotted as a function of B for different temperatures and different charge carrier densities. The charge neutrality point (CNP) of the sample is located around 3 V in backgate (see Fig. 6.1 in the previous chapter) In (a) the backgate voltage range is between -39 and -40 V which is at high carrier densities in the hole regime, in (b) the backgate voltage range is between 4 and 5 V which is close to the CNP and in (c) the backgate voltage range is between 49 and 50 V which is at high carrier densities in the electron regime. For temperatures below 31 K a nice symmetric WL peak centered around $B = 0$ T which broadens and decreases in amplitude for increasing temperature can be seen in all three charge carrier density regions. In the two regions of high charge carrier density, (a) and (c), this trend persist until 54 K. For low densities and high temperatures a transition from WL to WAL is expected [90], and indeed, close to the CNP the WL peak completely disappears above 31 K and a transition to WAL might be present. At large magnetic fields away from the WL peak the resistance increases with magnetic field. This positive magnetoresistance is temperature-independent and can be explained by standard classical effects due to the presence of two types of charge carriers [84]. This classical magnetoresistance is most pronounced close to the CNP and fades away with increasing charge carrier density in agreement with previous studies [84, 87].

In order to further analyze WL in the three-terminal junction we plot $\Delta R = \langle R(V_{\mathrm{BG}}, B) - R(V_{\mathrm{BG}}, 0)\rangle_{\Delta V_{\mathrm{BG}}}$ as a function of B for small magnetic fields (corresponding to a zoom in in Fig. 7.2 as marked by grey shaded areas) and fit the curves with Eq. 7.1 (solid lines). Three free fitting parameters L_ϕ, L_i and L_* are used and it can be seen that the theory fits the data very well.

In Fig. 7.3 the trends of decreasing peak heights and broadening peak widths with increasing temperature seen already in Fig. 7.2 are even more pronounced. From Eq. 7.1 it is clear that for low temperatures the width of the WL peak for small B-fields are mainly controlled by L_ϕ, while the bending of the curves at lager B-fields is controlled by L_i and

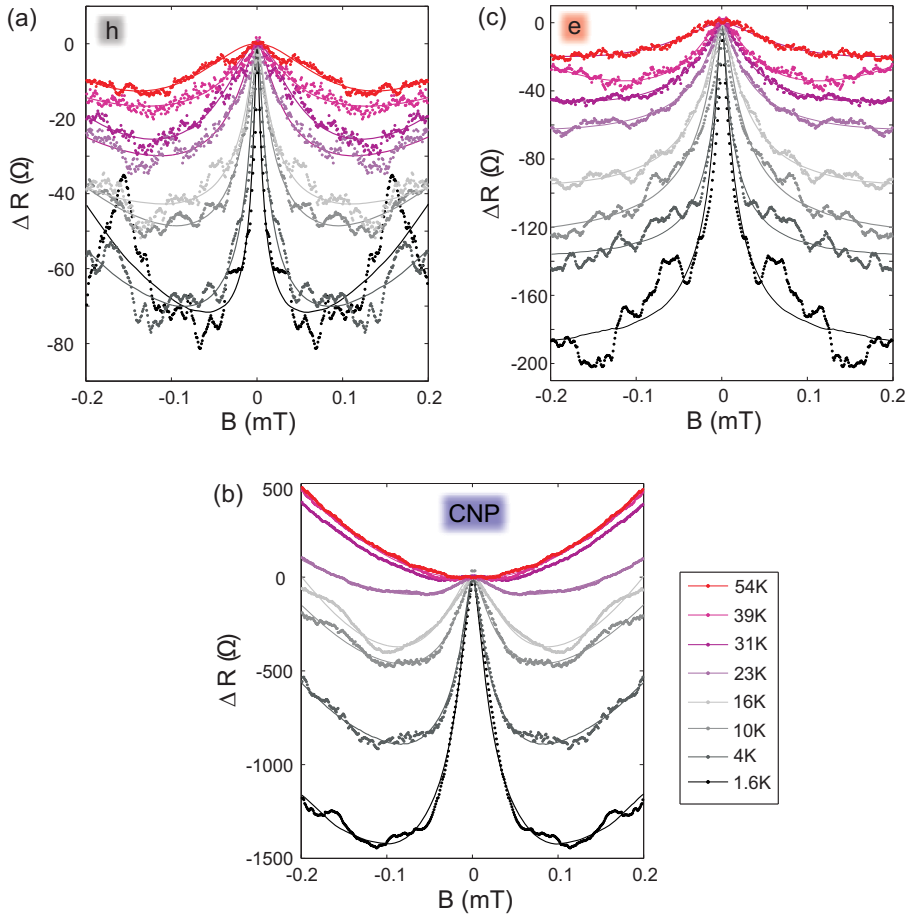

Fig. 7.3 — Evolution of the magnetoresistance with increasing temperature from 1.6 K to 54 K for three different charge carrier density regions (zoom corresponding to the grey shaded area in Fig. 7.2). (a) Region of hole transport, (b) close to the CNP and (c) region of electron transport. All traces are symmetrized and averaged over 1 V in backgate voltage. (In (a) V_{BG} is -39 to -40 V, in (b) V_{BG} is 4 to 5 V and in (c) V_{BG} is 49 to 50 V.) The solid lines are fits to Eq. 7.1

L_*. Thus, already from the raw data the expected trend of decreasing L_ϕ for increasing temperature is evident.

The resulting fit parameters L_ϕ, L_i and L_* extracted from the fits shown in Fig. 7.3 are plotted as a function of temperature for the three different charge carrier densities in Fig. 7.4. (The dashed lines are guides to the eye.) In the region close to the CNP hardly any UCFs are visible after averaging, while for higher densities some signatures of UCFs are still visible after averaging for low temperatures. This leads to a larger error in the fitting of the tails of the WL peak as will be further discussed later. In addition it should be pointed out that the geometry of our device is not trivial. Therefore, in the absence of any reliable method for an accurate determination of the geometry factor W/L, we here assume $W/L = 1$ such that $\Delta R = \Delta\rho$. Consequently the absolute values of the extracted fit parameters must be treated with care and we will in the following focus on the trends.

In all three measured charge carrier density regimes L_ϕ decreases monotonically with

increasing temperature. This is consistent with previous studies [86, 87] and has been explained by electron-electron interactions [86]. In addition L_ϕ is slightly shorter close to the CNP than at higher densities, something which has been related to the formation of electron-hole puddles close to the CNP [86]. The intervalley scattering length L_i is in these measurements always longer than L_ϕ. This is in contradiction to previous reports where L_i is always shorter or comparable to L_ϕ. The reason for this discrepancy is not clear. Naively one might expect L_i to be shorter for the narrow junction studied here compared to a larger rectangular sample due to increased scattering off the edges. However, the area of the junction is very small compared to the total distance of $\approx 4\,\mu$m between the current contacts. Outside the junction area the sample is between 2 and 5 μm wide. Thus, only a very short part of the total electron path takes place within the junction, the main part is travelled outside the junction where the graphene flake is wide. The width of the device outside the junction is however comparable to previous studies and cannot explain the longer L_is. Here it is important to note that the relationship between L_i and L_ϕ is not independent of the choice of geometry factor used to convert R to ρ. Consequently, it is possible that L_i is artificially large in the analysis done here due to a wrongly chosen geometry factor and that our results are indeed in agreement with previous studies.

Furthermore, L_i is expected to be temperature independent. This is observed in the electron regime (Fig. 7.4(c)), to some extent in the hole regime (Fig. 7.4(a)), but certainly not close to the CNP (Fig. 7.4(b)) where L_i seems to increase as the regime of WAL might be entered. The physical reason for this trend is also not clear. However, it should be noted that the fitting procedure is difficult in this range of temperature and charge carrier density. Finally, the intravalley scattering time L_* is found to be generally independent of temperature and significantly shorter than L_ϕ and L_i. These observations are again both consistent with previous studies [86, 87], however the reason for the short L_* is currently not known. Speculations involving crystal defects, ripples and scattering off charged impurities on the graphene surface could all not explain the observed L_* [86].

7.2 Universal conductance fluctuations

Reproducible Universal conductance fluctuations are also a result of interference between electrons in a phase coherent sample. The total conductance of a sample is given by the interference of all electrons traversing the sample. Even though there is a statistical distribution of electron paths that leads to averaging where the interference contributions cancel each other, this averaging will not be complete in a sufficiently small sample. As a result a modulation of the conductance of the sample is seen when the phase differences between the contributing paths are changed. Changing the Fermi energy of the sample, the magnetic field or the impurity distribution will therefore all result in UCF.

In contrast to WL and WAL, UCF are not affected by the subtle interplay between intravalley and intervalley scattering. Theoretically no special behaviour is expected for UCF in graphene, as in other two-dimensional systems they are expected to be universal and ergodic, i.e independent of the mechanism of phase randomization [88]. However, a previous study of UCF in single and bilayer graphene by Ojeda et al. found a difference in the density dependence of gate voltage dependent UCF and magnetic field dependent

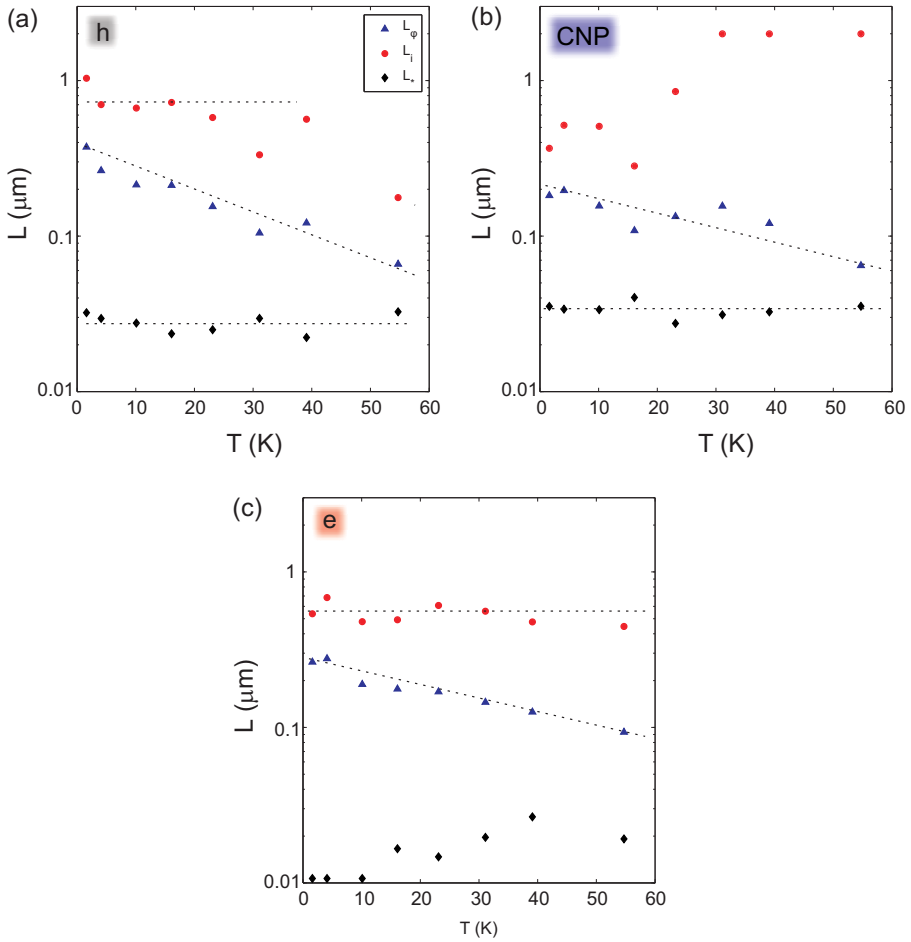

Fig. 7.4 — L_ϕ (blue triangles), L_i (red dots) and L_* (black diamonds) as a function of temperature in (a) the hole regime, (b) near the charge neutrality point and (c) in the electron regime. The dashed lines are guides to the eye.

UCF [88]. While the B dependent UCF were almost independent of charge carrier density, the gate voltage dependent UCF were largest close to the CNP. Another previous study of bilayer and trilayer graphene by Staley et al. also see a density dependence of the UCF amplitudes, however, the complete opposite trend as Ojeda et al. [93]. They see a suppression of the UCF amplitude close to the CNP. In both cases the authors speculate that the observed behaviour is due to the presence of random "puddles" of electrons and holes near the CNP. Additional studies are therefore needed to confirm if any of these density dependences of the UCF amplitudes are universal or simply sample dependent.

7.2.1 Density dependence

In the following UCF in a three-terminal junction is studied as a function of gate voltage and magnetic field. A symmetric bias of 250 μV is applied between the left and the right terminal while the center terminal floats (see Fig. 7.5) and the current flowing between

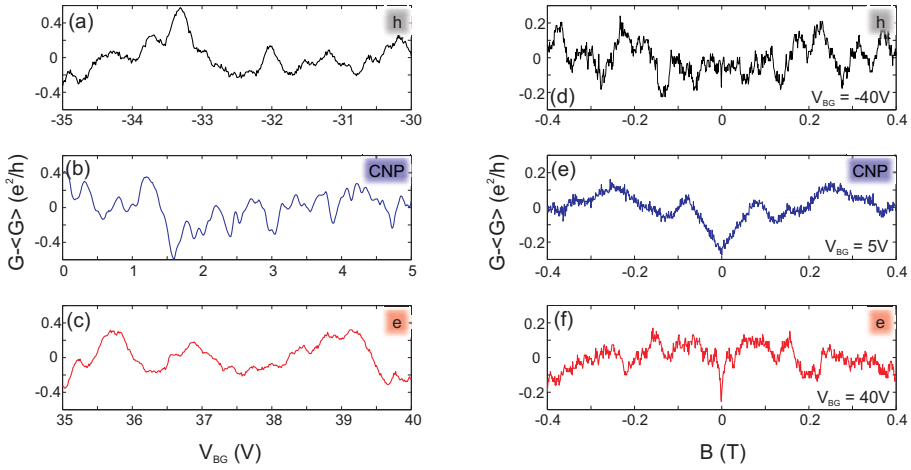

Fig. 7.5 — UCFs as a function of V_{BG} (a)-(c) and as a function of B (d)-(f). in the hole regime (a), close to the CNP (b) and in the electron regime (c). UCFs as a function of B in the hole regime (d), close to the CNP (e) and in the hole regime (f). The black curves, (a) and (d), are measured in the hole regime. The blue curves, (b) and (e), are measured close to the CNP. And the red curves, (c) and (f), are measured in the electron regime. The amplitude of the fluctuations are similar in all density regimes, while the period of the oscillations varies. For the gate dependent fluctuations a smoothed background is subtracted and for the B dependent oscillations a constant background is subtracted.

the left and the right terminal is measured. Fig. 7.5 shows nicely reproducible UCF as a function of gate voltage (a)-(c) and magnetic field (d)-(f). For the gate voltage dependent UCF a smooth background has been subtracted, while for the B dependent UCF a constant background is subtracted. For the analysis of the B dependent UCF the magnetic field is kept below 0.4 T in order to avoid any contributions from Shubnikov de Haas oscillations.

UCF for three different density regimes are shown, the hole hole regime (a) and (d), near the CNP (b) and (e) and in the electron regime (c) and (f). From the raw data it can already be seen that the amplitude of the gate dependent UCF are generally larger than the amplitude of the B dependent amplitudes. However, no clear density dependent difference in amplitude is seen for either type of oscillations. As expected the period of the oscillations are density dependent. The gate dependent oscillations have short periods for low densities, while the B dependent oscillations have short periods for high densities.

As a measure of the amplitude of the UCF we extract the root-mean-square magnitude of the fluctuations $\delta G_{V_{\mathrm{BG}},B} = [\mathrm{Var}(G)]^{1/2} = [\langle (G - \langle G \rangle_{V_{\mathrm{BG}},B})^2 \rangle_{V_{\mathrm{BG}},B}]^{1/2}$. Fig.7.6 (a) shows conductance as a function of V_{BG} from -40 to 40 V. The corresponding resistance as a function of V_{BG} is plotted in (b), while the gate dependence of δG for both gate dependent and B dependent oscillations is shown in (c). Already from the conductance plotted in Fig. 7.6(a) it is evident that there are no large differences in oscillation amplitude between high and low densities. This is also confirmed in (c) where there is no systematic evolution of δG with increasing or decreasing carrier density. There are only small, random variations which are within the uncertainty of the measurements. This is in contradiction to previous observations [88, 93] and suggests that such dependencies are indeed sample dependent and most likely linked to the disorder potential of the specific samples.

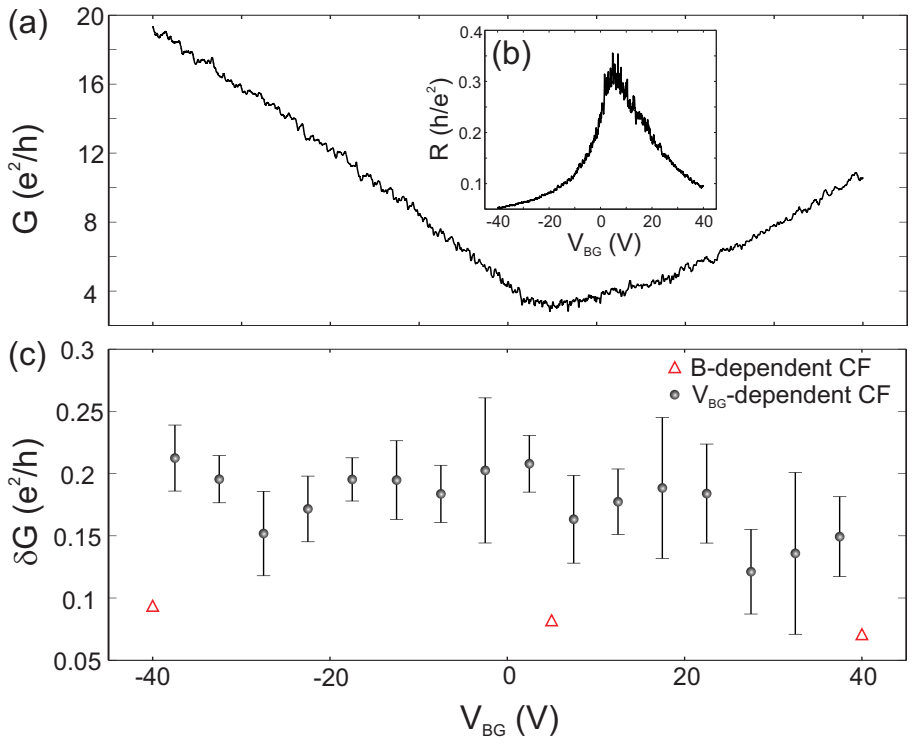

Fig. 7.6 — (a) G as a function of V_{BG} where it can be seen that the amplitudes of the UCFs are similar in all charge carrier density regimes. (b) Corresponding R as a function of V_{BG}. (c) Amplitude of the backgate dependent (black circles) and magnetic field dependent (red triangles) UCFs δG. The error on the backgate dependent amplitude is the standard deviation of three different measurements.

For the B dependent fluctuations we only have three measurement to evaluate (as shown in Fig. 7.5 (d)-(f)). Plotting these three values for δG_B together with the values for δG_{BG} it can be seen that δG_B is generally smaller than $\delta G_{V_{\mathrm{BG}}}$, but also density independent. At finite magnetic field time-reversal symmetry breaks down, resulting in a reduced oscillation amplitude [83]. This is consistent with previous measurements on B-field dependent UCFs [88].

7.2.2 Temperature dependence

To complete this study of UCF in graphene we investigate the temperature dependence of the fluctuations. In Fig. 7.7(a) the temperature dependence of the conductance through the junction for a large V_{BG} range from 1.6 to 140 K is shown. The curves are offset by e^2/h for better visibility and the arrow indicates increasing temperature. As expected the UCF amplitude decreases with higher temperature and for the highest temperatures no fluctuations are visible anymore. We extract the temperature dependence of δG in three different density regimes as indicated by the the three grey bars in Fig. 7.7(a). In each regime we average over 10 V in backgate. The resulting temperature dependence of δG for holes, close to the charge neutrality point and for electrons are shown in Fig. 7.7(b). The

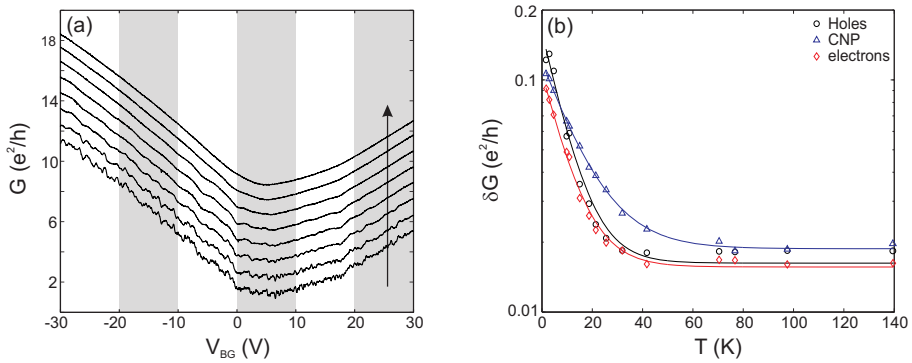

Fig. 7.7 — Temperature dependence of the UCFs. (a) Large backgate sweeps showing how the UCFs are increasingly washed out for higher temperatures. The arrow indicates increasing temperature. The curves are offset by e^2/h for better visibility. (b) The amplitude of the UCFs δG as a function of temperature plotted for three different density regimes. Black circles corresponds to the hole regime, blue triangle to the CNP and red diamonds to the electron regime. Each point is obtained by averaging over 10 V in backgate as indicated by the 3 grey regions in (a).

oscillation amplitude is found to decrease exponentially with increasing temperature before it saturates. (The solid lines are fit to a saturating exponential decay.) The saturation is not due to UCF remaining at high temperature, but due to the fact that the conductance curve is never completely smooth, but contains small kinks. Therefore the saturation value is higher close to the Dirac point where there are more pronounced kinks than at higher densities where the curve is smoother. Close to the CNP δG decrease slightly slower with increasing temperature than at higher densities. However, this might also be due to the relatively large kinks close to the Dirac point that are difficult to exclude from the analysis, rather than real UCF.

From theory for thin metals δG is expected to decay following an inverse power law [94, 95], which has also been experimentally observed in a mesoscopic graphite wire [40]. The exponential decay of δG observed here has also previously been observed in graphene [96], however, no theoretical explaination has been provided so far.

7.3 Disorder potential

In the previous two sections general magnetoresistance properties of graphene, which can be measured in any bulk graphene structure, were investigated. In this section we want to again take advantage of our special three-terminal structure and use this to probe the bulk disorder potential of graphene. The general idea is straight forward. In a simple picture the three-terminal junction can be understood as a basic voltage divider. When a push-pull bias is applied between the left and the right lead (See Fig. 7.8(a)) the voltage measured at the center lead V_c will reflect the difference in resistance between the left and the right part of the device. Thus, any changes observed in V_c as a function of gate voltage are results of changes in the relationship between the resistance of the left and the right part of the device. Bulk graphene is known to have a disorder potential creating electron

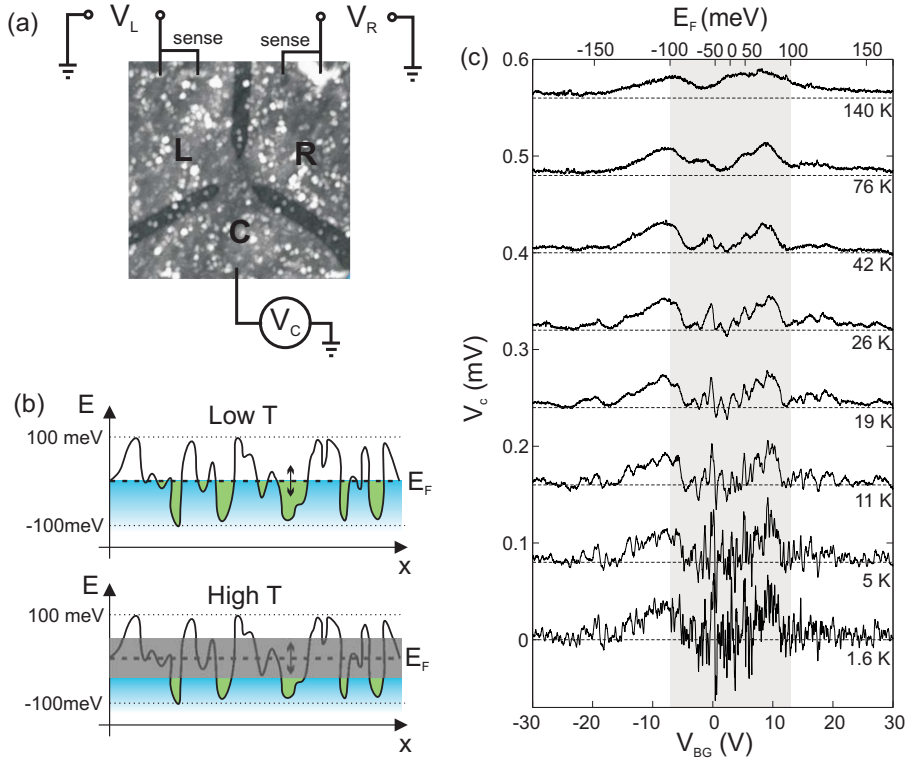

Fig. 7.8 — (a) Measurement setup. A 500 μV symmetric push-pull bias is applied to the left and the right branches. The sense function ensure that the complete bias voltage drops over the junction and contact effects are avoided. At the center branch the voltage V_c is measured. (b) An illustration of the bulk disorder potential in graphene leading to puddles of electrons and holes. The charge carriers are filled up to the Fermi energy (indicated by a dashed line) which is varied by tuning the backgate (indicated by the arrow). For low temperatures (upper figure) all puddles can be resolved, while for higher temperatures (lower figure) smearing around the Fermi energy (grey area) will only allow the probing of some puddles. (c) Measurement of V_c as a function of V_{BG} for increasing temperature between 1.6 K and 140 K. The curves are offset by 80 μV for better visibility. On the upper horizontal axis the Fermi energy calculated from V_{BG} by assuming a density of states linear in energy is plotted. The grey shaded area highlights the gate voltage range corresponding to the expected disorder potential.

and hole puddles of the order of 100 meV [82, 97] as illustrated in Fig. 7.8. Even though Klein tunneling is expected to suppress the influence of the disorder potential by allowing perfect tunneling between electron and hole puddles, this effect will not be perfect and the disorder potential will still influence transport, even in the absence of a confinement gap.

By changing the backgate voltage and thus the overall Fermi energy of the device the puddle configuration within the device will be changed. Generally, with increasing Fermi energy more and more small puddles will merge to larger puddles until the Fermi energy reaches the extension of the disorder potential. The random changes in the puddle configuration of the device should lead to subtle changes in the resistances of the two parts of the junction which should be measurable as switches in the center voltage. Large changes in the resistance between the left and the right part of the junction that change

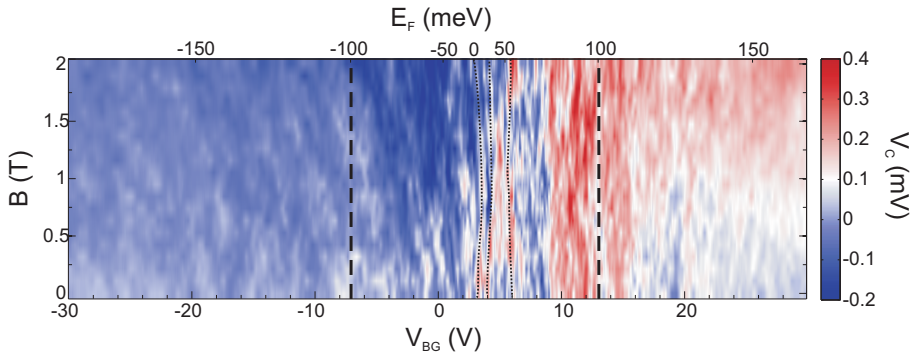

Fig. 7.9 — V_C as a function of V_{BG} and B. The Fermi energy corresponding to the backgate voltage is indicated on the upper horizontal axis and the expected range of the disorder potential is marked with thick dashed black lines. Examples of features that seems to be independent of B are marked with narrow dotted lines. The push-pull bias applied to the device is 2 mV.

the relative magnitude of the resistance of the two junctions will switch the sign of V_c, while smaller changes that just change the relative resistance, something which will only switch V_c slightly without changing the sign.

In Fig. 7.8(c) V_c is shown as a function of V_{BG} for different temperatures between 1.6 K (lowest trace) and 140 K (uppermost trace). In the lowest trace measured at 1.6 K V_c fluctuates rapidly over the whole backgate voltage range. Here both switching events that change the sign of V_c and switching events that do not change the sign of V_c can be seen. Two different gate voltage regimes can be identified. For high charge carrier density the amplitude of the fluctuations is small, while for a region of ± 10 V around the CNP (highlighted in grey in Fig. 7.8(c)) the amplitude of the fluctuations is significantly larger. As stated above, this backgate voltage range corresponds to the expected extension of the bulk disorder potential. Thus, signatures of puddles are are expected only in this range and not for higher charge carrier densities. We interpret the fluctuations at higher densities as a result of universal conductance fluctuations. At low temperatures, changing the Fermi level will change the interference of the different charge carrier paths contributing to the current and thus changing the resistance of the device. This leads to fast fluctuations in V_c that are present for all charge carrier densities and are superimposed on top of any fluctuations due to the disorder potential.

In the previous section the temperature dependence of UCF was investigated. It was shown that their amplitude decays exponentially with increasing temperature until about 40 K where no UCF are visible anymore. In Fig. 7.8(c) V_c vs V_{BG} is plotted for increasing temperatures up to 140 K. It can be clearly seen how the small fluctuations at high densities continuously fade out for increasing temperature, while close to the CNP some larger fluctuations persist to higher temperatures. Already at 26 K only few fluctuations due to UCF are present, while at 42 K no fluctuations are seen anymore at high densities. At this point one can count 5 to 7 changes in V_C which are not present at 76 K. This should then in a simple picture correspond to 5 to 7 puddles present in the junction area at 42 K. This gives a puddles size of 50 to 60 nm, which is comparable to puddle sized of about 100 nm reported for etched graphene nanoribbons on SiO_2 [98].

In order to access the disorder potential at low temperatures where the UCF are dominant we measure V_C as a function of both V_{BG} and magnetic field as shown in Fig. 7.9. Fluctuations due to UCF should change with magnetic field when the magnetic field is changed over a larger range than the correlation field which has been determined to be $\approx 0.5\,\mathrm{T}$. Features due to the disorder potential, however, are expected to be independent of magnetic field for this field range. In Fig. 7.9 the expected range of the disorder potential in backgate voltage is marked with two thick black vertical lines. Within this region we search for features which are independent of B. This turnes out to not be trivial. Many features are definitely not independent of B, and there are some features that might be considered as independent of B (three possible candidates are marked with black dotted lines), however, a clear quantitative statement supporting the interpretation of the measurements in Fig. 7.8(c) can unfortunately not be made.

In further attempts to analyze this data set we also tried to average the V_C vs V_{BG} for a magnetic field range larger than the correlation field. But, this also did not lead to a clear conclusion. Furthermore, statistical analysis to determine the correlation energy of the fluctuations were tried. However, all statistical analysis were only successful in the low temperature regime where the number of fluctuations were large due to UCF. For higher temperatures there were not enough fluctuations for a meaningful statistical analysis.

7.4 Summary

A device originally designed to show a novel voltage rectification at room temperature has been used to gain further knowledge about fundamental properties of transport in diffusive and phase coherent graphene devices. Pronounced weak localization, with a possible transition to weak antilocalization, has been observed and found to generally agree with previous reports. Furthermore, the amplitude of universal conductance fluctuations has been investigated as a function of gate voltage and magnetic field where no gate voltage dependence is found and the amplitude is found to decay exponentially with increasing temperature. Finally an attempt to study the disorder potential of graphene was made. The general range of the disorder potential are in agreement with previous studies and the expected number of puddles extracted from the measurements are also reasonable. However, a good quantitative analysis was not possible.

Part III

Transport in three-terminal graphene quantum dots

Chapter 8

Multi-level transport in a three-terminal quantum dot

Graphene quantum dots (QDs) have attracted a lot of attention during the last couple of years. This is especially due to their predicted long spin life times which makes them promising candidates for spin qubits [99]. Even though important progress towards smaller, better controlled and better understood devices has been made during the last couple of years, research on graphene quantum dots is still in its infancy compared to quantum dots defined in conventional 2DEGs.

The first challenge when creating a graphene quantum dot is to actually confine the charge carriers. As a consequence of the gapless band structure charge carriers cannot be electrostatically confined. However, by cutting graphene into narrow ribbons a so-called transport gap is opened where the current is suppressed around the charge neutrality point [98, 100–104]. By using short and narrow constrictions as tunnel barriers graphene quantum dots have been successfully created. Even though these tunnel barriers are difficult to tune in a systematic manner there has been an impressing development of such quantum dots. Excited states have been observed in single [105] and double quantum dots [106–108], spin states have been investigated [109] and the electron-hole crossover has been studied [110]. Even though the modulation of transport through graphene quantum dots due to localized states in the constrictions have been investigated in several studies [111–113], there are open questions concerning the detailed influence of constriction localizations on transport on small energy scales.

In this chapter transport in a three-terminal graphene quantum dot in the multi-level transport regime is investigated. The advantage of a three-terminal quantum dot compared to a two-terminal quantum dot is that the three-terminal structure allows for the determination of individual conductances between the dot and each lead [114]. As a result one gains further insight into the role of localized states in the constrictions for transport through the dot. In addition, being in the multi-level regime gives a unique chance to experimentally observe how different leads couple with different strengths to different dot states.

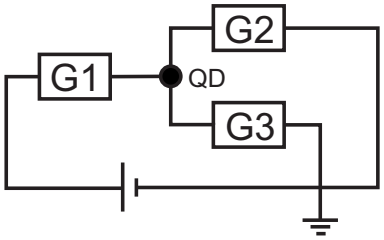

Fig. 8.1 — Schematic drawing of a classical resistor network corresponding to a three-terminal quantum dot. $G1$, $G2$ and $G3$ are the individual conductances of the three different leads.

8.1 Three-terminal quantum dots

For a standard two-terminal quantum dot in the weak coupling regime ($h\Gamma << k_{\mathrm{B}}T$) and the regime of single-level transport ($k_{\mathrm{B}}T << \Delta$) a conductance resonance can be described by [30]

$$G = \frac{e^2}{4k_{\mathrm{B}}T}\frac{\Gamma_{\mathrm{S}}\Gamma_{\mathrm{D}}}{\Gamma_{\mathrm{S}}+\Gamma_{\mathrm{D}}}\cosh^{-2}\left(\frac{\alpha_{\mathrm{g}}(V_{\mathrm{g}}-V_{\mathrm{res}})}{2k_{\mathrm{B}}T}\right) \tag{8.1}$$

where Γ_{S} and Γ_{D} are the tunneling rates from the dot to the source and the drain respectively and α_{g} is the lever arm of the gate. Thus, the maximum of a resonance is directly related to the tunneling rates between the dot and the two leads. However, such an experiment does not allow for the determination of the individual tunneling rates between the dot and each lead. However, as we will see in the following, in the case where three or more terminals are connected to the dot, the individual tunnel couplings between the dot and each lead can actually be determined by measuring the complete conductance matrix of the system [114].

The coupling strength between the dot and one lead is a measure of the tunneling rate between the dot and this specific lead and is given by the overlap of the dot wavefunction and the lead wavefunction. For a conventional QD confined in a 2DEG the coupling strength is expected to be given by two contributions, a monotonically changing contribution from the lead wave function and a randomly fluctuating contribution from the dot wavefunction. Thus, measurements of the individual coupling strengths between the dot and the single leads offers a possibility to study the spatial fluctuations of the dot wavefunction. For a graphene quantum dot the situation is slightly different. The tunnel barriers in graphene QDs are formed by short and narrow graphene ribbons where the current is suppressed by the formation of localizations. Thus, these tunnel barriers are complex systems in themselves and one does not necessarily expect the contribution to the coupling strengths between the dot and one lead from the tunneling barrier to be monotonic as for a GaAs QD.

The conductance matrix **G** of a three-terminal system is given by

$$\begin{pmatrix} I_1 \\ I_2 \\ I_3 \end{pmatrix} = \begin{pmatrix} G_{11} & G_{12} & G_{13} \\ G_{21} & G_{22} & G_{23} \\ G_{31} & G_{32} & G_{33} \end{pmatrix} \begin{pmatrix} V_1 \\ V_2 \\ V_3 \end{pmatrix} = \mathbf{G} \begin{pmatrix} V_1 \\ V_2 \\ V_3 \end{pmatrix}. \tag{8.2}$$

From the conductance matrix the currents through the dot for each possible bias voltage configuration is fully determined. There are two sum-rules that should be obeyed by the conductance matrix. First, due to current conservation $\Sigma_{i=1}^{3} G_{ij} = 0$ for all j. (In the following this will be reffered to as the current sum rule.) Second, if the same voltage is applied to all leads no current should flow, $\Sigma_{j=1}^{3} G_{ij} = 0$ for all i. (In the following this will be referred to as the voltage sum rule.) In addition, at zero magnetic field **G** should be symmetric, $G_{ij} = G_{ji}$. As a result there are only three independent conductance matrix elements, from which the complete matrix can be deduced.

For single-level transport in the weak coupling regime the individual tunnel couplings, Γ, between the dot and each lead can be determined from the conductance matrix using the following expression [83]

$$\mathbf{G} = \frac{e^2}{4k_B T} \frac{1}{\Gamma_1 + \Gamma_2 + \Gamma_3} \begin{pmatrix} \Gamma_1(\Gamma_2 + \Gamma_3) & -\Gamma_1\Gamma_2 & -\Gamma_1\Gamma_3 \\ -\Gamma_2\Gamma_1 & \Gamma_2(\Gamma_1 + \Gamma_3) & -\Gamma_2\Gamma_3 \\ -\Gamma_3\Gamma_1 & -\Gamma_3\Gamma_2 & \Gamma_3(\Gamma_1 + \Gamma_2) \end{pmatrix}. \tag{8.3}$$

In the multilevel regime more than one QD level contribute to transport. In this case the conductance through each QD level is given by the tunnel coupling between this specific level and the leads. Therefore, to find the total conductance in one leads one has to sum up the contributions from all QD states. Thus, in the multilevel regime the individual tunnel coupling strengths from the dot to each lead cannot be extracted directly from the conductance matrix.

However, if we consider the quantum dot as a classical star-shaped conductance network (see Fig. 8.1), we can extract the three individual conductances G_k connecting lead k to the dot from the relation

$$\mathbf{G} = \frac{1}{G_1 + G_2 + G_3} \begin{pmatrix} G_1(G_2 + G_3) & -G_1G_2 & -G_1G_3 \\ -G_2G_1 & G_2(G_1 + G_3) & -G_2G_3 \\ -G_3G_1 & -G_3G_2 & G_3(G_1 + G_2) \end{pmatrix}. \tag{8.4}$$

These individual conductances are not equivalent with individual couplings, however, they still allow for a quantitative understanding of the transmission through the individual tunnel barriers of the quantum dot.

8.2 Sample and experimental methods

A scanning force micrograph (SFM) image of the measured quantum dot is depicted in Fig. 8.2(b). The quantum dot is connected to three leads, labeled 1, 2 and 3, through narrow constrictions. From the SFM image the diameter of the dot is determined to be 110 nm and the width of the constrictions is found to be 40 nm. In addition to the global

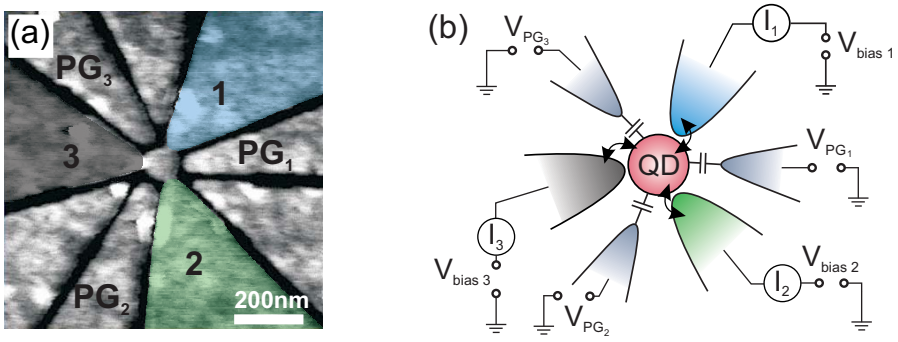

Fig. 8.2 — (a) Scanning force micrograph image of the measured quantum dot. Leads 1, 2 and 3 are highlighted in blue, green and black, respectively. Three plunger gates are used to tune the dot in addition to the global back gate. (b) The measurement setup. On each lead a bias can be applied and the current flowing can be measured.

silicon back gate (BG) three in-plane plunger gates, PG_1, PG_2 and PG_3, are used to tune the dot and the constrictions. The remaining three in-plane gates influence the transport through the dot only weakly and are therefore not used.

In Fig. 8.2(b) we additionally sketch the measurement setup. In all measurements presented in this chapter a DC bias voltage is applied to one of the three leads while the other two leads are grounded. The currents through the three leads are measured simultaneously using current-voltage converters. All measurements are performed at 1.7 K unless stated otherwise.

8.3 Measurements

8.3.1 Device characterization

Fig. 8.3(a) shows the currents through the dot for a large range in V_{BG}. Curves labeled I_1, I_2 and I_3 correspond to the current measured in lead 1, 2 and 3 respectively. For this measurement 1 mV bias is applied to lead 1, while leads 2 and 3 are grounded. We use the convention that negative currents flow from the leads into the quantum dot, while positive currents flow from the quantum dot into the leads.

Around the charge neutrality point a region of ≈ 12 V of suppressed current, corresponding to the transport gap [102], can be seen. Within this region Coulomb blockade is observed. From Coulomb diamond measurements we determine the charging energy of the quantum dot to be 8-15 meV (see Fig. 9.1 in the next chapter).

It can also be seen that constriction 2 is generally more closed than 1 and 3. For high charge carrier densities I_2 is less than 10% of I_1 (the total current). This asymmetry is also present in the regime of Coulomb blockade where the current flowing through constriction 2 is often too small to be measured and the quantum dot is effectively a two-terminal dot. Still, it is possible to find regimes where the current contributions from the three leads are

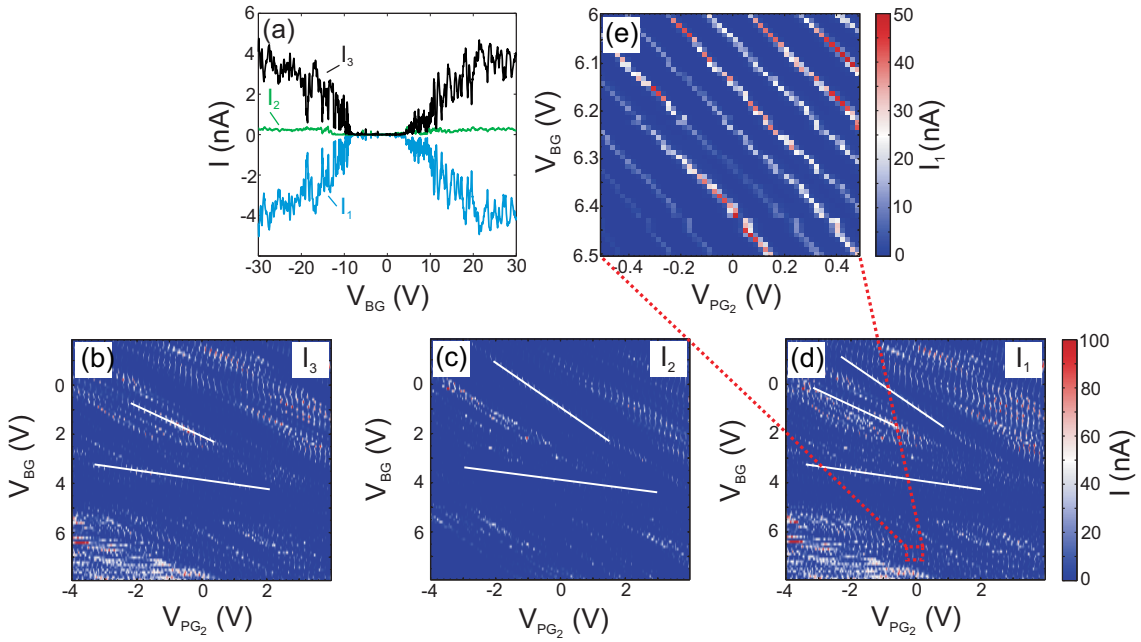

Fig. 8.3 — (a) Current through the three leads as a function of back gate voltage for a large backgate voltage range. A bias voltage of 1 mV is applied to lead 1, while leads 2 and 3 were grounded. A transport gap of ≈ 12 V in back gate can be seen. (b)-(d) I_3, I_2 and I_1 as a function of V_{BG} and V_{PG_1} for large gate voltage ranges. The broad diagonal lines are due to resonances in the constrictions. (e) A zoom of (d) where the narrow diagonal lines corresponds to Coulomb peaks.

Tab. 8.1 — Relative lever arms α_{PG}/α_{BG} for the in-plane gates with respect to the dot and the three constrictions.

	$\alpha_{PG}^{QD}/\alpha_{BG}^{QD}$	$\alpha_{PG}^{Constr.1}/\alpha_{BG}^{Constr.1}$	$\alpha_{PG}^{Constr.2}/\alpha_{BG}^{Constr.2}$	$\alpha_{PG}^{Constr.3}/\alpha_{BG}^{Constr.3}$
PG_1	0.59	1.15	0.68	0.25
PG_2	0.50	0.13	0.88	0.65
PG_3	0.58	0.65	0.13	1.15

comparable and in the following sections we will focus on one of these regimes.

In order to characterize the device further we measure the current through the three leads as a function of V_{BG} and each of the three plunger gates on both a small and a large voltage scale, and determine the plunger gate lever arms relative to the back gate lever arms α_{PG}/α_{BG} with respect to the dot and each of the three constrictions. As an example Fig. 8.3(b)-(d) shows I_1, I_2 and I_3 respectively, as a function of V_{BG} and V_{PG_2}. A voltage of 1 mV is applied to lead 1 and I_1, I_2 and I_3 are measured simultaneously. The gates are swept over a large voltage range and the broad diagonal lines that are visible are attributed to resonances in the constrictions [111]. In Fig. 8.3(d) three different slopes (marked by white lines) can be identified, while only two different slopes can be found in Fig. 8.3(b) and (c). Since lead 1 is biased all charge carriers flowing through the dot have to tunnel through constriction 1. As a result, resonances originating from localized states in constriction 1 are seen in all three currents. On the other hand, a resonant state in lead 2 or 3 will

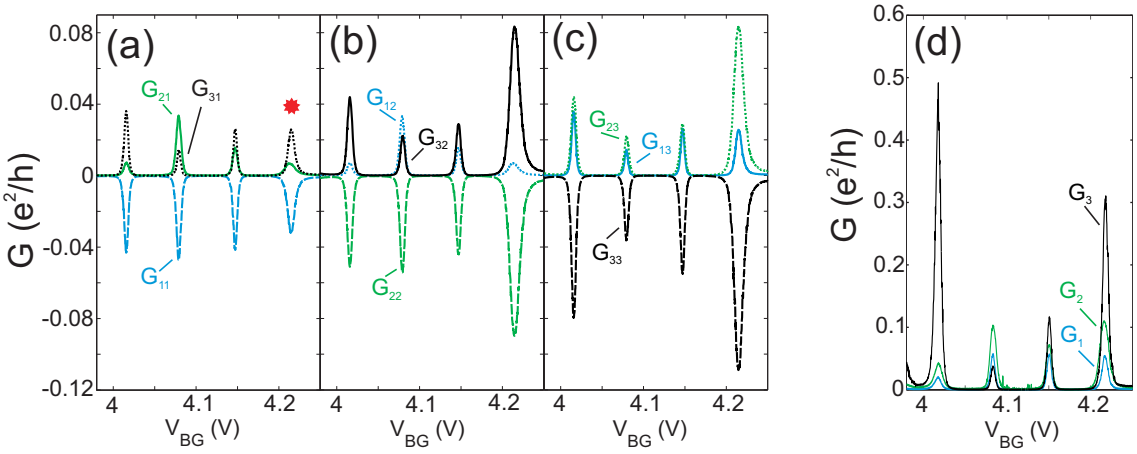

Fig. 8.4 — (a)-(c) Measurement of the complete conductance matrix for the system. The conductance in lead 1, 2 and 3 is plotted in red, orange and black respectively. The conductance in the biased lead is always plotted negative. (d) Corresponding individual conductances.

enhance the current only in this specific lead, with the consequence that only the current through this specific lead (and the biased lead) is enhanced. From this measurement we can therefore assign one slope to states in each constriction and subsequently determine $\alpha_{\mathrm{PG}_2}/\alpha_{\mathrm{BG}}$ for all three constrictions. Complementary measurements were done for the two other plunger gates and the complete set of $\alpha_{\mathrm{PG}}/\alpha_{\mathrm{BG}}$ is summarized in Table 8.1. These lever arms are consistent with the geometry of the sample (Fig. 8.2).

Fig. 8.3(e) shows a high resolution measurement corresponding to a zoom of Fig. 8.3(d) (see the red square in Fig 8.3(d)). The narrow diagonal lines correspond to single Coulomb resonances in the quantum dot and from the slope we determine $\alpha_{\mathrm{PG}}/\alpha_{\mathrm{BG}}$ for the dot. From corresponding measurements varying the other two in-plane gates the relative dot lever arms of all three plunger gates are extracted. These lever arms can also be found in Table 8.1.

From Table 8.1 it can be seen that the relative lever arms with respect to the dot $\alpha^{\mathrm{QD}}_{\mathrm{PG}}/\alpha^{\mathrm{QD}}_{\mathrm{BG}}$ are very similar for all three plunger gates. However, the lever arms with respect to the different constrictions vary significantly. In particular the lever arm of each plunger gate with respect to the constriction on the opposite side of the dot is much weaker than all other lever arms. Hence, the plunger gate dependence of transport through the dot can be used to identify if changes are due to alterations of the dot wave function or the constriction resonances.

8.3.2 Determination of individual conductances from the conductance matrix

The conductance matrix **G** of a three-terminal system is given by Eq. 8.2. In Fig. 8.4(a)-(c) the nine elements of the conductance matrix for four consecutive Coulomb resonances are shown, measured by applying a 100 uV bias to lead 1, 2, and 3 respectively. For these measurements the current sum rule is obeyed with a relative error less than 1 % of the

highest current level, while the voltage sum rule is obeyed with a relative error less than 10 % of the highest current level. In order to obtain such a small error the measurements are done very carefully. To minimize the influence of voltage offsets in the measurement setup, measurements for positive and negative bias were averaged. In addition, to avoid errors due to instabilities of the sample all nine elements of the conductance matrix for both positive and negative bias are measured before each BG step. In other words, all conductance matrix elements are measured within a single back gate sweep.

As mentioned above, for single-level transport individual tunnel couplings between the dot and each lead can be determined from the conductance matrix. In that transport regime the width of the Coulomb peaks is peak-independent for a given temperature. Looking at the Coulomb peaks in Fig. 8.4(a)-(c) it can be seen that in our measurements the width of the peaks varies (especially pronounced for the forth peak). This is a sign of multi-level transport. Here we can therefore only determine the individual conductances of the three leads using the expression given in Eq. 8.4. In Fig. 8.4(d), G_1, G_2 and G_3 obtained from the nine conductance matrix elements shown in Fig. 8.4(a)-(c), can be seen. The individual conductances fluctuate extensively from peak to peak demonstrating that the coupling strengths between the leads and the dot vary significantly from peak to peak. In a previous study of a three-terminal GaAs QD, the individual conductances were found to fluctuate randomly on a scale of about 0.02 e^2/h. Here fluctuations over a range of 0.5 e^2/h are observed. This suggests that from peak to peak the variations seen in the individual conductances may indeed not only be due to changes in the dot wavefunction, there might also be a significant nonmonotonic contribution from the lead wavefunction given by changes in the tunnel barriers.

8.3.3 Temperature dependence

In the previous section signs of multi-level transport were seen. To further support this, we present the temperature dependence of the Coulomb peaks shown in Fig. 8.4. This is depicted in Fig. 8.5 where all nine conductance matrix elements are plotted as a function of V_{BG} for seven different temperatures between 1.7 K and 10 K. The symmetry of the conductance matrix can be nicely seen, demonstrating the high quality of the measurements. Furthermore, it can generally be seen that all Coulomb peaks broaden with increasing temperature. By having a closer look at the three independent conductance matrix elements G_{21}, G_{31} and G_{32} it can be seen that for the first peak (from the left) and the third peak, the peak maxima increase for increasing temperature, which is a signature of multilevel transport [115]. However, for the second peak the peak maximum increases with increasing temperature for G_{31} and G_{32} while it decreases for G_{21}. A similar behaviour is seen for the fourth peak where the peak maximum increases with increasing temperature for G_{21} and G_{31} while it decreases for G_{32}. It should be noted that even though two peaks are seen to decrease in height, they do not show the $1/T$-dependence as expected for true single-level transport.

It is known that in the multi-level regime the temperature dependence of Coulomb peaks can vary from peak to peak due to variations in the couplings between the leads and the different dot states. [115] However, the measurement of different temperature dependences of conductances measured in different leads for the same Coulomb peaks is

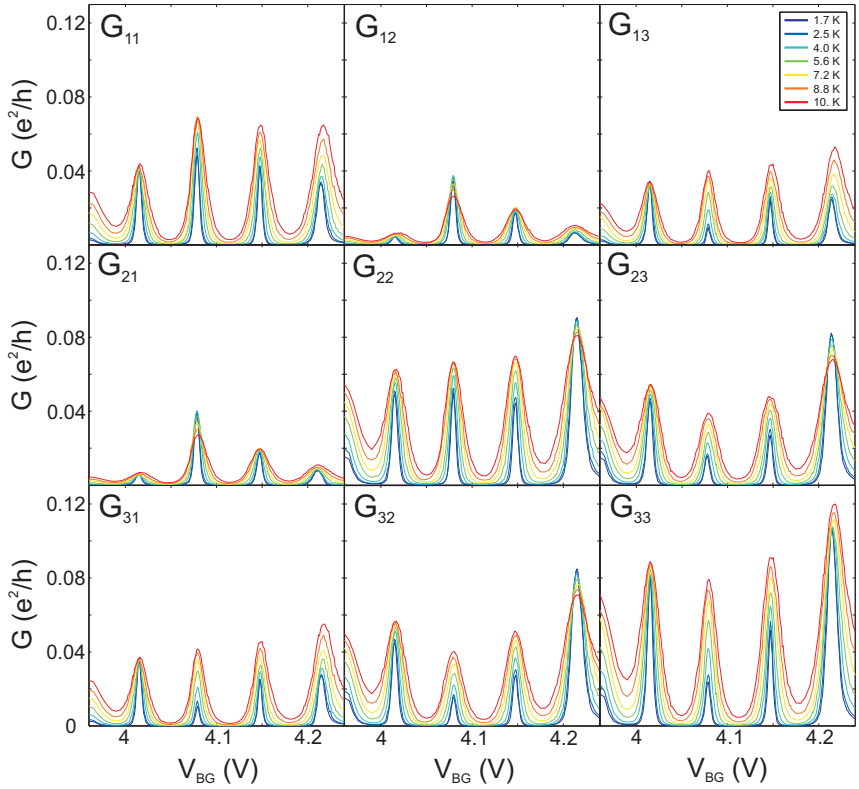

Fig. 8.5 — Temperature dependence of the four studied Coulomb peaks. All the nine conductance matrix elements are plotted. By looking at the three independent matrix elements G_{21}, G_{31} and G_{32} it can be seen that for the first and the third peak (from the left) the peak maxima increase with increasing temperature for all three conductance matrix elements. However, for the second peak the peak maxima increase with increasing temperature for G_{31} and G_{32} while it decreases for G_{21}. A similar behaviour with different temperature dependence for the different conductance matrix elements are seen for the fourth peak.

unique to a three or more terminal system and has to our knowledge not been measured before. Following the arguments of Ref. [115], our results suggest that the different leads couple with different strengths to the different dot states involved in transport. This is further supported by detailed measurements of single Coulomb peaks as discussed below.

8.3.4 Shift between Coulomb resonance positions due to coupling of different leads to different dot states

When studying single Coulomb peaks in detail we frequently observe that peaks corresponding to conductances in different leads have their maxima at slightly different positions in gate-voltage. An example of this is shown in Fig. 8.6(a) where G_{31} and G_{21} are plotted for the fourth peak in Fig. 8.4(a) (see red star). A 100 μV bias voltage is applied to lead 1, a voltage of 100 mV is applied to gate 1 while all other gates are grounded. The conductance G_{31} (black dotted curve) has its maximum at 4.217 V while G_{21} (orange solid curve)

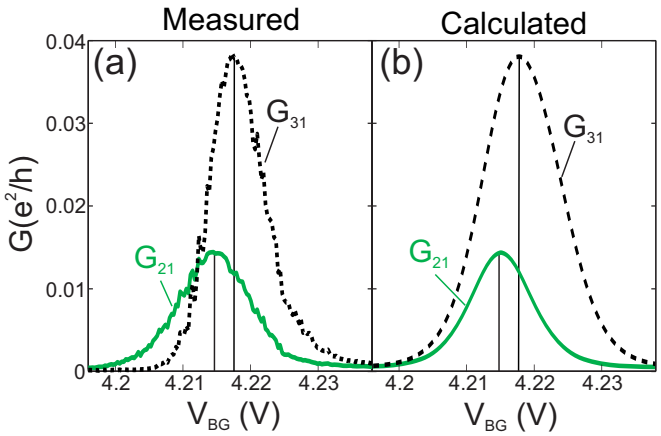

Fig. 8.6 — (a) Measurement of G_{21} and G_{31} as a function of V_{BG} for a single Coulomb peak. The maxima of the two peaks are shifted by 2 mV in back gate voltage corresponding to $0.9\,k_BT$ when assuming that the FWHM of the peaks are $\approx 4.4\,k_BT$. (b) Corresponding calculation with a two-level model where the three leads couple differently to the two dot levels.

has its maximum at 4.215 V. For multi-level transport the full width at half maximum (FWHM) of a Coulomb peak is $\approx 4.4\,k_BT$, where k_B is the Boltzmann constant and T is the temperature [83]. From the FWHM of the measured peaks we then estimate the shift between the maxima of G_{31} and G_{21} to be $0.9\,k_BT$.

It should be noted that the measurements shown in Fig. 8.6(a) are not averaged between conductances measured for positive and negative bias (unlike in Fig.8.4). The gating effect of the lead where the bias is applied shifts the Coulomb resonances in energy at finite bias voltages. For positive bias voltages the resonances are shifted to more positive back gate voltages, while for negative bias voltages they are shifted to more negative back gate voltages. Averaging would therefore result in a broad resonance with a maximum positioned between the maxima of the original resonances. By only considering the conductances measured with the bias voltage applied to the same lead (for positive or negative bias voltage), the gating effect of the source causes the same shift for all resonances. Hence, the shift of 2 mV between the maxima of G_{21} and G_{31} found above is not due to a gating effect of the source.

The shift between the maxima of the conductances of G_{21} and G_{31} can be understood in terms of multi-level transport where the leads couple with different strengths to the different dot states. In order to illustrate this effect qualitatively, we calculate G_{31} and G_{21} for the simplest possible multi-level system, a two level system. We use the rate equation approach introduced by Beenakker in Ref. [83] extended to a three-terminal dot with two levels contributing to the current.

In this model it can be shown that the current in each lead is the sum of two contributions, one current via the first level and one current via the second level. The shift between currents in two different leads is determined by three parameters, the single particle level spacing Δ and two parameters determining how the current in each lead is distributed between the two dot levels.

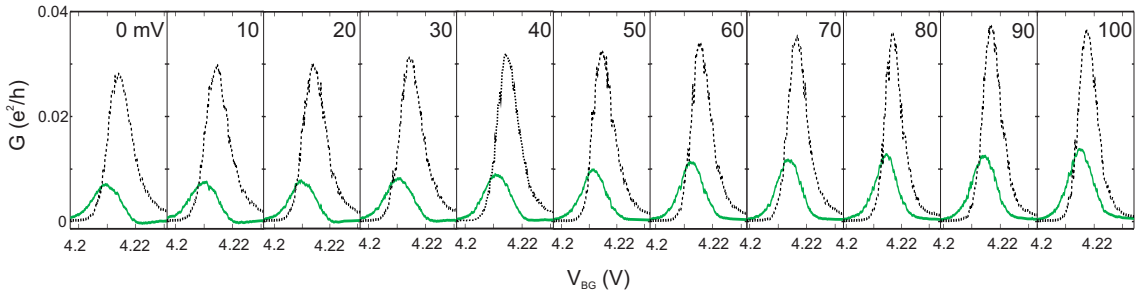

Fig. 8.7 — Measurement of G_{21} and G_{31} as a function of V_{BG} for different constant voltages between 0 and 100 mV applied to PG_1. The shift between the maxima of the two peaks are shrinks continuously with increasing plungergate voltage.

The measured shift can be qualitatively reproduced by the model for a large range of parameters. An example of a calculation showing good agreement with the experiment in Fig. 8.4(a) is depicted in Fig. 8.4(b). In order to put more constraints on the values of the parameters we also tried to reproduce the temperature dependence of the peaks. Unfortunately, with a two level model it is not possible to quantitatively reproduce the observed shift and the observed temperature dependence at the same time. Thus, we here most likely have more than two levels involved in transport. Still, we would like to emphasize that the simple two-level model does qualitatively reproduce the shift, supporting that it is indeed due to the different coupling of different leads to different dot states. This also agrees with the interpretation of the temperature dependence of the Coulomb peaks as discussed above.

8.3.5 Evolution of Coulomb resonance shift with in-plane gate voltages

From the above discussion we argue that the observed shift is due to different leads coupling with different strengths to different quantum dot states. However, it is still an open question if the localized states in the constrictions play an important role for small changes in the coupling strengths between the leads and the dot.

In Fig. 8.7 the evolution of G_{21} and G_{31} with increasing V_{PG_1} is shown. It can be seen that already for small plunger gate voltages the shift can be tuned significantly and systematically by an in-plane gate. This is further shown by plotting shifts from Fig. 8.7 relative to the average FWHM of the peaks as a function of V_{PG_1} (see Fig. 8.8(a)). Here the continuous decrease of the shift with increasing plungergate voltage is even more pronounced. Fig. 8.8(b) shows the evolution of the individual conductances G_k of the three leads with V_{PG_1}. Fig. 8.8(c) and (d) show the corresponding evolution of G_1, G_2 and G_3 for V_{PG_2} and V_{PG_3} respectively. If the changes in the coupling between the dot states and the lead states would be dominated by changes in the localizations in the constrictions we would expect a correlation between the evolution of the individual conductances and the relative lever arms of the plunger gates with respect to the constrictions (see Table 8.1). However, no correlation is found. G_3 is influenced the most by all three plunger gates. G_2 and G_1 are only changed slightly. We therefore conclude that the Coulomb blockade resonances and in particular the amplitudes of the current maxima investigated here are

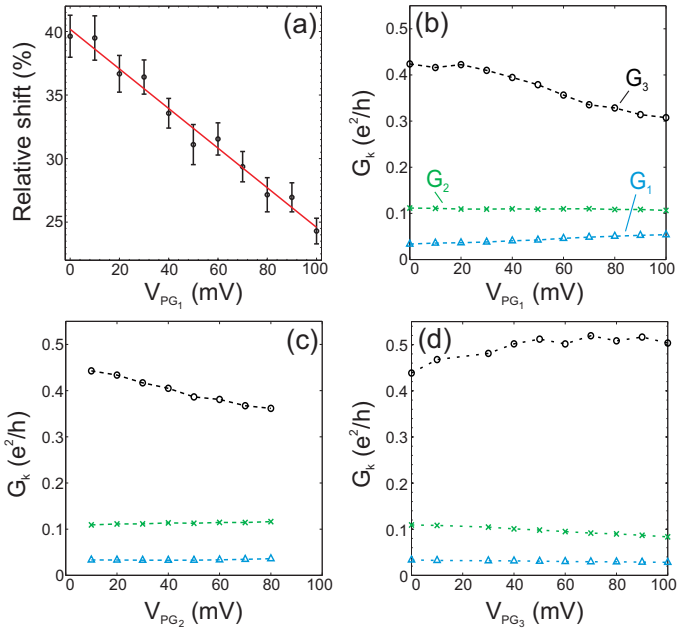

Fig. 8.8 — (a) Shift/FWHM as a function of V_{PG_1}. The red line is a linear fit to the data points. (b) Corresponding evolution of the individual conductances as a function of V_{PG_1}. G_2 hardly changes, G_1 changes only slightly, while G_3 changes significantly. For the evolution of the individual conductances as a function of V_{PG_2} (c) and V_{PG_3} (d) G_1 and G_2 again change only slightly while G_3 changes significantly.

mostly governed by the wave function in the dot and to a lesser extent by localization sites in the leads.

Furthermore, it can be seen that in general the effect of PG_3 is opposite to the effect of PG_2 and PG_1. This might indicate that it is indeed not random how the G's are changing and that such measurements could be used to obtain further qualitative understanding on how the dot wave function is distributed in the dot. The lack of any geometric correlation with the evolution of the G's also suggests that the plunger gates tune the dot wave function as a whole, rather than several independent puddles.

8.4 Summary

We have investigated a three-terminal graphene quantum dot in the multi-level Coulomb blockade regime. The dot was thoroughly characterized by both gate-gate sweeps where all relative lever arms could be extracted, and temperature dependent measurements. When investigating single Coulomb peaks in more detail a shift in peak maxima between conductances measured in the different leads were observed. This result can be qualitatively reproduced by a rate equation model where different leads couple differently strong to different dot states. The shift can be tuned by the plunger gates and by investigating the corresponding evolution of the individual conductances we find no correlation between this evolution and the relative lever arm determined. We therefore conclude that on small

energy scales the changes in coupling are due to changes in the dot wave function, which is rather a single wave function extended over the dot than several localized states. This is an important insight in view of the potential to use graphene quantum dots for spin qubits.

Chapter 9

Finite bias spectroscopy

Finite bias spectroscopy is a widely used and convenient method to probe excited states of quantum dots. However, the lines of enhanced conductance parallel to the Coulomb diamonds that are due to transport through excited states are often accompanied by other lines of which the origin is not completely understood [106, 110]. Possible origins that have been suggested are modulation of the tunnel couplings due to resonances in the constrictions [106, 110] and phonon-mediated transport [116].

In this chapter finite bias spectroscopy of the three-terminal quantum dot introduced in the previous chapter is performed. A rich spectra of lines of enhanced conductance are visible outside the Coulomb diamonds. By exploiting the extra information obtained from a three-terminal dot compared to a two-terminal dot we discuss the possible origins of these pronounced features. As in the previous chapter all measurements are performed in a cryostat at a temperature of 1.7 K.

9.1 Coulomb Diamonds

Fig. 9.1 shows Coulomb diamonds measured for the complete conductance matrix. A bias voltage is applied to one of the two leads while the two other leads are grounded. The first row corresponds to bias voltage applied to lead 1, the second row corresponds to bias voltage applied to lead two and the third row corresponds to bias voltage applied to lead 3. Similar, the current measured in lead 1, lead 2 and lead 3 are depicted in column 1, 2 and 3 respectively. The slight asymmetry of the diamonds is due to the asymmetric bias voltage. As expected for a single confined dot, the diamonds are well defined and do not overlap and the charging energy is determined to be 15 meV. This is the largest charging energy observed within this sample. For most well defined Coulomb diamonds the charging energy fluctuates between 8 and 15 meV. This is slightly higher than what is expected from Ref. [113], however, deviations due to different screening by the surrounding leads and gates are expected.

Looking at the different plots in Fig. 9.1 it is evident that a symmetry of the conductance matrix where $\log dI_i/dV_j = dI_j/dV_i$ (as seen in Fig. 8.5) is not present here. This might be partly due to the fact that the Coulomb diamonds were measured separately for each

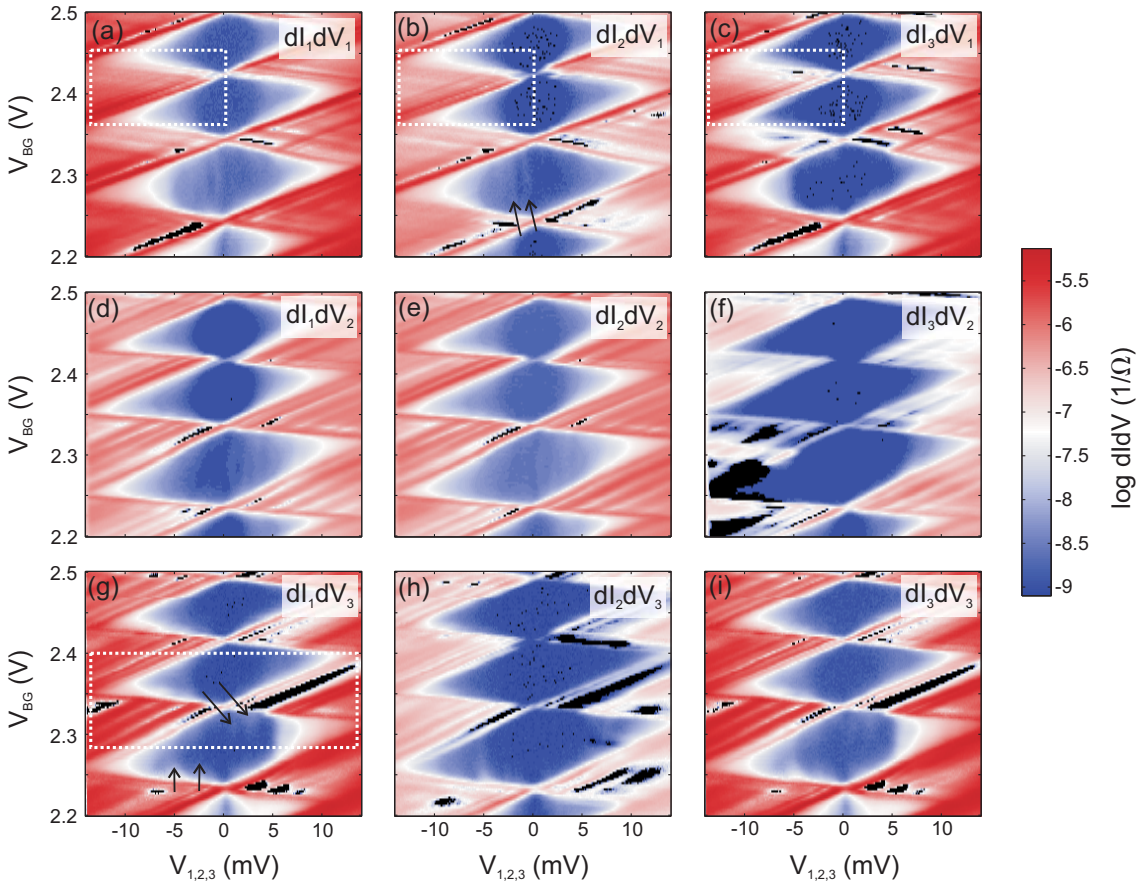

Fig. 9.1 — Coulomb diamonds. The differential conductance for all three leads and all three bias configurations (the complete conductance matrix) is shown. Outside the diamonds pronounced lines parallel to the diamond edges can be seen. In some plots faint vertical lines within the diamonds can be observed (marked with black arrows in (b) and (g)). Regions of negative differential conductance are marked in black.

bias configuration and not in one gate sweep as in the previous chapter, however, the main reason for this asymmetry can most likely be attributed to the non-linearity of the system at high bias voltages.

Outside the diamond regions of suppressed current a striking number of lines of enhanced differential conductance parallel to the edges of the diamonds can be seen. In addition there might also be some faint structures visible within the diamonds (as marked with black arrows in Fig. 9.1 (b) and (g)). The possible origin of these features will be discussed in the following.

9.2 Excited states?

Lines of enhanced differential conductance outside the diamonds running parallel to the edges of the diamonds are often attributed to conductance through excited states and their

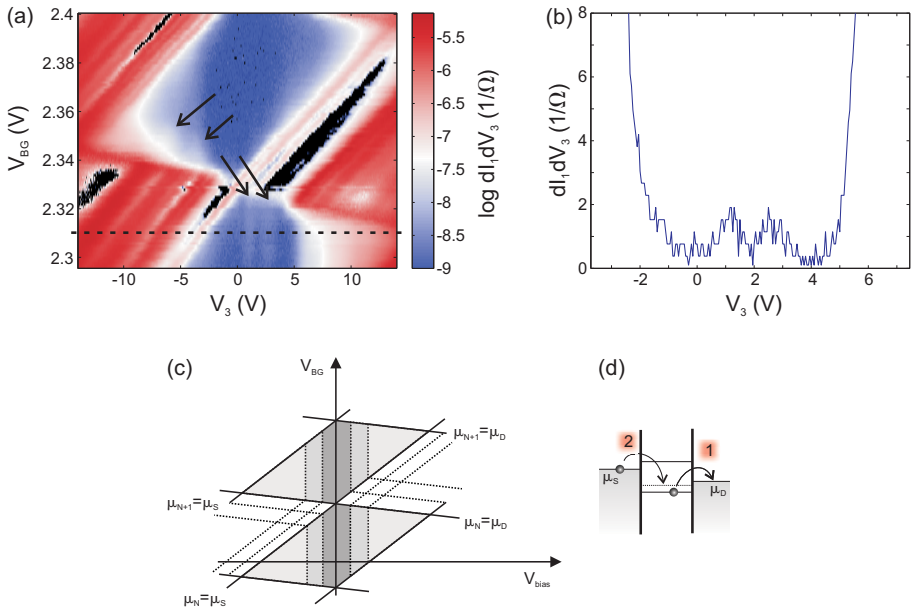

Fig. 9.2 — (a) Zoom of Coulomb diamonds corresponding to the white dotted box marked in Fig. 9.1(g). In the lower diamond one can clearly see two vertical lines (marked with black arrows) that are aligned with lines running parallel to the diamond edge outside the diamond. In the upper diamond similar feature (also marked with black arrows) might be faintly visible. As in Fig. 9.1 negative differential conductance is marked in black. (b) A cut through the lower diamond (as marked with the black dashed line in (a)). Two clear peaks in dI_1dV_3 inside the Coulomb blockaded area can be seen. (c) schematic drawing of the expected steps seen in dI/dV_{bias} within the Coulomb diamonds in the presence of inelastic co-tunneling processes as illustrated with the energy diagram in (d).

appearance can thus be used to determine the single particle level spacing of the quantum dot states. However, such lines can also have different origins such as a modulation of the density of states in the leads or states in the constrictions.

9.2.1 Inelastic cotunneling?

So far we have only considered transport through first order tunneling processes. However, the presence of inelastic cotunneling, a higher order tunneling process, is often used as the experimental fingerprint of excited states. Fig. 9.2(d) shows the energy diagram of an inelastic co-tunneling process where two electrons tunnel in a correlated fashion. First an electron from the dot ground state will tunnel from the dot to the drain (marked with 1), subsequently an electron from the source will tunnel into the dot excited state (process 2). The final state of the quantum dot is higher in energy, by a factor of Δ, than the initial state. This energy difference is provided by the bias voltage. As a result such a process can only occur for $eV_{\text{bias}} \geq \Delta$ and beyond this bias voltage the current increases linearly with V_{bias} [30]. Thus, when measuring dI/dV_{bias} as a function of V_{bias} a step in dI/dV_{bias} inside the diamonds which align with the excited state line outside the diamond is expected. This is illustrated in Fig. 9.2(c).

Fig. 9.2(a) shows a zoom of two diamonds from Fig. 9.1(g) (see the white dotted box in Fig. 9.1 (g)). In the lower diamond one can clearly see two quite broad vertical lines (as marked with the black arrows) of enhanced differential conductance. These two broad lines seems to align with lines outside the diamond running parallel to the edge of the upper diamond. In the upper diamond one might also faintly see similar vertical features on the left side of the diamond (also marked with black arrows).

To further investigate the features inside the lower diamond we plot the differential conductance dI_1/dV_3 as a function of bias voltage V_3 corresponding to a cut through Fig. 9.2(a) as marked with the dashed black line. In this measurement one clearly see two peaks in dI_1/dV_3 within the Coulomb blockaded region. For the inelastic co-tunneling process discussed above and illustrated in Fig. 9.2(c) and (d) one expect to see a step in the differential conductance that align with excited states outside the Coulomb blockaded region. Here, we don't see any steps, but oscillations. The expectation of steps in the differential conductance are based on the assumption that the current due to inelastic co-tunneling increases linearly with increasing bias voltage after the onset of the inelastic co-tunneling. However, if the current does not increase linearly, but stepwise, this would lead to peaks in the differential conductance. Such a situation might be possible with a strong modulation of the density of states in the leads. However, in the case of a strong modulation of the density of states in the leads it should be pointed out that elastic co-tunneling processes where no excited states are involved might also lead to oscillations within the Coulomb blockaded regime. Thus, at this point it is not clear if the features inside the diamonds are really due to inelastic co-tunneling and therefore can be seen as evidence for excited states.

9.2.2 Line positions

If we now consider a quantum dot with N-1 electrons. Then the lines of enhanced conductance appearing outside of the Coulomb diamonds due to transport through excited states of the Nth level μ_N^k ($k \geq 1$) will appear parallel to the diamond edge where $\mu_N = \mu_S$ for negative bias and $\mu_N = \mu_D$ for positive bias. Correspondingly transport through excited states of the N-1 level will appear parallel to $\mu_N = \mu_D$ for negative bias voltages and parallel to $\mu_N = \mu_S$ for positive bias voltages. This is depicted in Fig. 9.3(a) where the red lines corresponds to excited states of the Nth level while the blue lines corresponds to excited states of the N-1 level. For the situation where the tunnel coupling of the source Γ_S is equal to the tunnel coupling of the drain Γ_D, one expect to see excited states line parallel to both $\mu_N = \mu_S$ and $\mu_N = \mu_D$ for both positive and negative bias.

However, in an experimental situation it is not uncommon that the tunnel coupling of the source and the drain to the dot differs significantly. In this case the lines of enhanced conductance due to excited states will only occur parallel to either $\mu_N = \mu_S$ or $\mu_N = \mu_D$. Let us consider the situation depicted in the energy diagram of the lower part of Fig. 9.3(b) where the tunnel coupling to the between the source and the dot is much smaller than the tunnel coupling between the drain and the dot. For a negative applied bias (left diagram) it is very difficult for electrons to tunnel from the source and into the dot, however, when an electron has tunneled into the dot it can leave the dot very easily. In this case, an excited state entering the bias window will significantly increase the probability of tunneling into

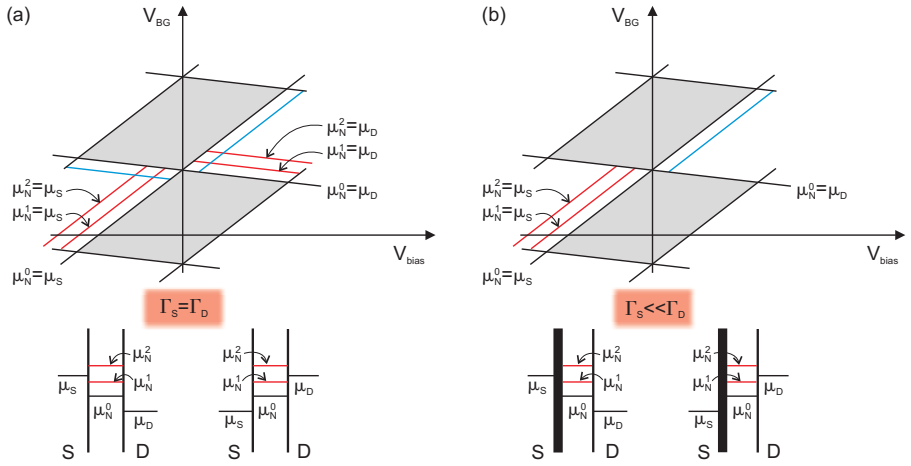

Fig. 9.3 — (a) Sketch of the expected appearance of excited states parallel to the diamond edges for equal coupling to source and drain. (b) Corresponding sketch of the expected appearance of excited states outside the Coulomb blockaded regime when the tunnel barrier to the source is much thicker than the tunnel barrier to the drain. The red lines correspond to excited states of the first empty dot state and the blue lines correspond to excited states of the last occupied dot state.

the dot, and thus enhanced current is expected. On the other hand, when a positive bias is applied to the dot electrons can very easily tunnel into the dot, however, it is difficult to tunnel out. In this case an electron that tunnel into the dot will be trapped there and as a result a new excited state entering the bias window will not change the current through the dot significantly and thus now excited state lines will appear outside the diamonds.

For the three-terminal quantum dot investigated here we consider the source to be where the bias is applied and the drain is the lead through which the current is measured. In Fig. 9.1(d) the differential conductance in lead 1 with respect to the bias applied to lead 2 (dI_1/dV_2) is plotted as a function of V_{BG} and V_2. Here mainly lines parallel to the steep edge of the diamonds where $\mu_N = \mu_S$ can be seen. From the discussion above this would then suggest that $\Gamma_2 < \Gamma_1$. In Fig. 9.1(b) the opposite configuration where the bias is applied to lead 1 and the current is measured in lead 2 is shown. For positive bias voltages one can indeed see mainly lines parallel to $\mu_N = \mu_D$, the opposite of the situation for dI_1/dV_2 and therefore still consistent with $\Gamma_2 < \Gamma_1$. For negative bias there are only few faint lines and it it difficult to make a clear statement. Now, if we consider dI_1/dV_3 as plotted in (g) mainly lines parallel to $\mu_N = \mu_S$ as in (d) can be seen. Following the arguments from before this then suggest that $\Gamma_3 < \Gamma_1$. In the opposite situation plotted in (c) lines in both directions can be observed, however, the lines are again not always easy to identify. In order to make a statement about the relationship between Γ_2 and Γ_3 we now consider dI_3/dV_2 ((f)) and dI_2/dV_3 ((h)). In the regimes where lines can be easily identified the lines outside the diamonds are mainly parallel to $\mu_N = \mu_S$ for both dI_2/dV_3 and dI_3/dV_2. This is not consistent with the picture of excited states observed only along

one diamond edge to to different tunnel couplings to source and drain.

From the differential conductance plots in Fig. 9.1 we deduce the qualitative relationship between the equivalent conductances of the tunnel barriers to be $G_1 > G_3 >> G2$. This is consistent with some of the observations from above based on the direction of the enhanced conductance lines. Thus, even though the direction of the lines are cannot be completely understood in this simple picture, they tend to follow the expected trend for excited states in the presence of different coupling strengths between the dot and the different leads.

9.2.3 Line spacings

From Fig. 9.1 the minimal separation between lines of enhanced conductance is determined to be 0.9 meV and the mean spacing is about 2 meV. This fits well with the reported single particle level spacing of 1.6 meV for a quantum dot with a diameter of 140 nm [105] and the expected single particle level spacing of 2 meV for a dot with a diameter of 110 nm [117]. However, in the previous chapter we argued to be in a few-level transport regime based on the temperature dependence and different widths of the Coulomb peaks. Thus the expected single particle level spacing Δ_{exp} is smaller than half of the thermal broadening, i.e $\Delta_{\text{exp}} < 300\mu eV$. This is three times smaller than the minimal spacing of the lines outside the diamonds here. This could be due to the fact that less than one out of three excited states significantly alter the current, however, this implies that the dot is weakly coupled to the leads. Thus, from the spacing of the lines it it can not be concluded weather these are due to excited states or not.

9.3 Lever arms

Lines of enhanced conductance appearing parallel to the diamond edges outside the Coulomb blockaded regime might also be due to a modulation of the density of states in the leads or caused by the localizations formed in the constrictions. In order to investigate this further we measure the evolution of the lines of enhanced differential conductance as a function of backgate voltage and plungergate voltages. In Fig. 9.4 (a)-(c) a bias of -12.5 mV is applied to lead 1 and in the main panels the differential conductance in all three leads are plotted as a function of V_{BG} and V_{PG2}. In the left narrow panels the current in the three leads are plotted as a function of backgate voltage at zero plungergate voltage to more easily identify the boundaries of the diamonds (marked with yellow diagonal lines in the main panels). In Fig. 9.4(d)-(f) the corresponding measurements as a function of V_{PG3} are shown. From the yellow diagonal lines the relative lever arms of the plunger gates $\alpha_{\text{PG}}/\alpha_{\text{BG}}$ to the dot are determined to be 0.50-0.52 which is consistent with the lever arms found in the previous chapter (see table 8.1).

It can be seen clearly from Fig. 9.4 that all diagonal lines visible are parallel to the boundaries of the diamonds within the uncertainty of the measurement. From table 8.1 we know the relative leverarms of the different plungergates with respect to localizations in the constrictions. These range from 0.13 to 1.15 and are significantly different from the dot lever arms. Hence, if the lines of enhanced conductance seen outside the diamonds in Fig. 9.1 were due to localizations situated in the constrictions lines with different slopes

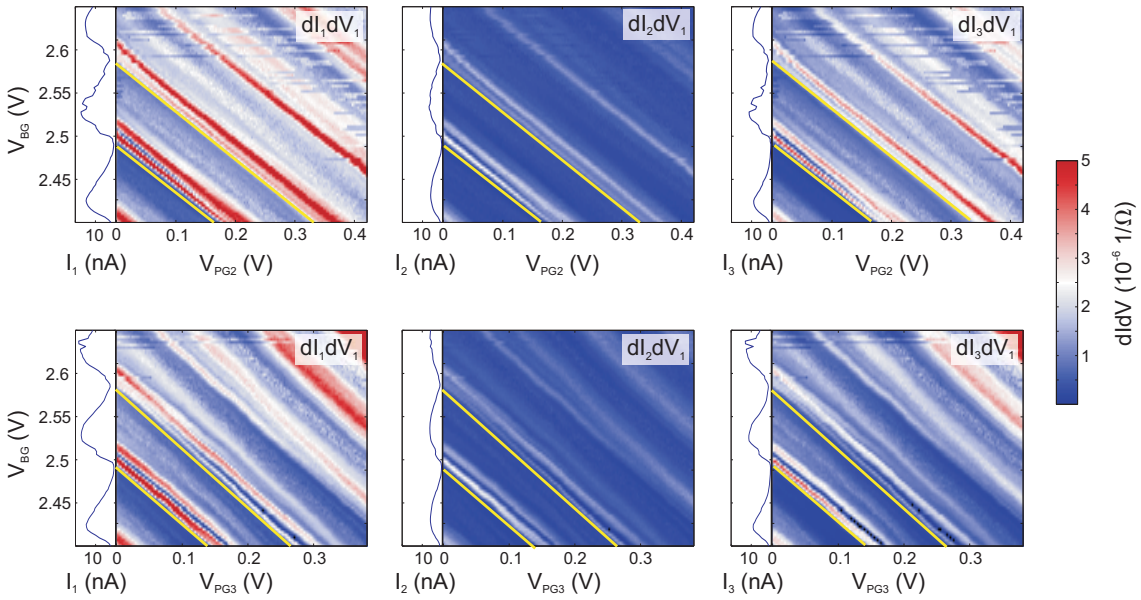

Fig. 9.4 — Cuts through the diamonds of Fig. 9.1(a)-(c) at a constant bias of -12.5 mV as a function of V_{PG2} (a)-(c) and V_{PG3} (d)-(f). On the left side of each plot the evolution of the current with backgate voltage for zero plungergate voltage is shown. The boundaries of the diamonds, corresponding to the minima of the currents in the left panels are marked with yellow diagonal lines.

corresponding to the slopes seen in Fig. 8.3 should be seen in Fig. 9.4. This is not the case and therefore the lines cannot be due to localizations in the constrictions.

The density of states in the leads is expected to be only very weakly tunable by the plunger gates due screening effects. Therefore, if the lines of enhanced conductance measured in Fig. 9.4 were due to a modulation of the density of states in the leads they should be almost horizontal, i.e only dependent on the backgate voltage and not on the plungergate voltage. This is also not observed, and thus we conclude that it is unlikely that the lines of enhanced conductance are due to a varying density of states in the leads.

9.4 Magnetic field dependence

In order to shed some more light on the features seen outside the Coulomb blockaded regime in Fig. 9.1 we measure the magnetic field dependence of the Coulomb diamonds. In Fig. 9.5 a zoom of the diamonds presented in Fig. 9.1 (a)-(c) (marked by the white dashed boxes) are measured for $B = 0\,T$ ((a)-(c)), $B = 2\,T$ ((d)-(f)) and $B = 4\,T$ ((g)-(i)). The first column ((a), (d) and (g)) shows the differential conductance measured in lead 1, the second column ((b), (e) and (h)) shows the differential conductance measured in lead 2 and in the third column ((c), (f) and (i)) the differential conductance measured in lead 3 can be seen. From 0 T to 2 T the lines of enhances conductance outside the Coulomb

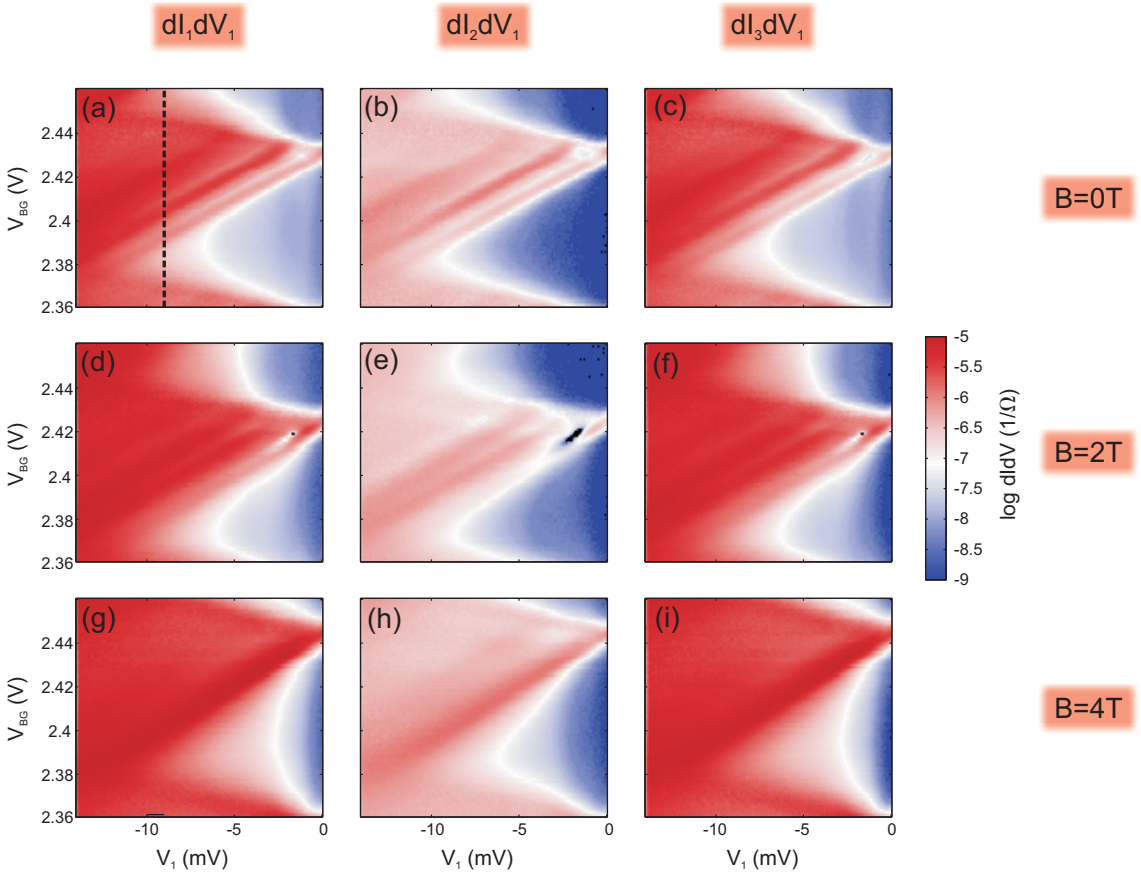

Fig. 9.5 — Magnetic field dependence of Coulomb diamonds. (a)-(c) B=0 T, (d)-(f) B=2 T and (g)-(i) B=4 T. The lines of enhanced differential conductance present at B=0 T are completely gone at B=4 T.

diamonds get smeared out and at 4 T no lines are visible anymore.

In Ref. [110] Coulomb diamonds in perpendicular magnetic field are investigated. There features outside the Coulomb blockaded region related to energy dependent fluctuations of the barrier transmissions disappear already at a magnetic field of 0.15 T, while features due to transport through excited states are well visible at 2 T. This corresponds well to our observations and might suggest that the features seen outside the Coulomb blockaded regime in Fig. 9.1 are indeed excited states.

9.4.1 Evolution of lines of enhanced conductance for small magnetic fields

In a very last study of these Coulomb diamonds we do accurate measurements of the evolution of the lines outside the Coulomb diamonds for small magnetic fields. In Fig. 9.6 the differential conductance through the dot as a function of V_{BG} and B at a constance bias voltage of -9 mV applied to lead 1 (corresponding to a cut through the diamonds in Fig. 9.5

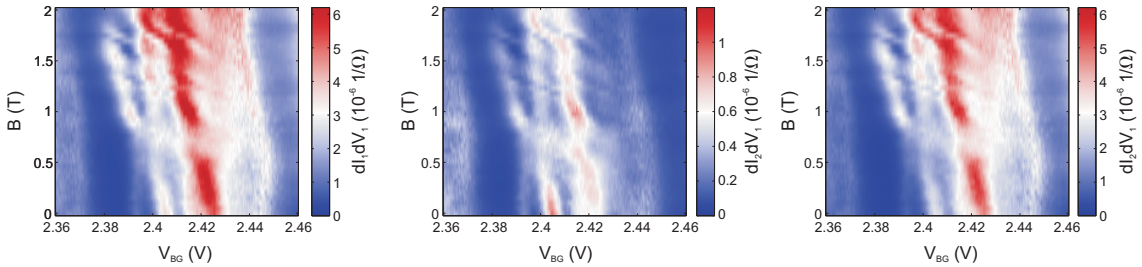

Fig. 9.6 — Evolution of the lines of enhanced differential conductance parallel to the diamond edges for small magnetic fields. A constant bias voltage of -9 mV is applied to lead 1 and the differential conductances measured in lead 1, 2 and 3 are shown.

as marked with the black dotted line in (a)) is shown. The main features are seen to just wiggle slightly in energy as a function of magnetic field, while oscillating in amplitude. In addition finer substructures that move horizontally to diagonally through the main features can be seen. The origin of these features are at the moment not understood.

9.5 Summary

We have investigated four consecutive Coulomb diamonds where pronounced lines of enhanced conductance parallel to the diamond edges where observed outside the Coulomb blockaded regions. From the plungergate dependence of these lines we conclude that they are not due to localizations in the constriction and most likely also not due to modulation of the density of states in the leads.

Are the lines then due to transport through exited states? From the measurement shown in this chapter we have seen that the spacing of the lines agree with what is expected for excited states for a dot of this size compared to previous reported excited states in the literature, however, the spacing is three times larger than what we would expect from being in a few-level regime as argued in the previous chapter. The co-tunneling features seen within the Coulomb diamonds are not a convincing experimental proof of excited states and and the alignment of the lines to the different diamond edges only partly agrees with an interpretation of excited states and a large difference in the tunnel barriers to source and drain. Therefore, at this point no clear conclusion about the origin of the lines of enhanced conductance parallel to the diamond edges can be made.

Conclusions

Chapter 10

Conclusion and outlook

The main goal of this thesis has been to increase the understanding of electronic transport in graphene nanostructures. A variety of experiments with different devices and different experimental methods has led to a diverse thesis. In the following we will sum up the main results of this thesis and discuss both the future of these specific projects and the more general future of transport in graphene nanostructures.

Chemical modification of graphene

Chemistry on graphene has a great potential which has only been briefly investigated so far. A conventional two-dimensional electron gas formed at the interface between two materials in a layered crystal is not accessible for chemistry. Graphene however, is not embedded into a crystal and therefore easily accessible by any kind of chemistry. However, as a result graphene is also directly exposed to the environment and therefore its quality can easily be degraded by "dirt".

In part I of this thesis chemical modification of graphene with diazonium ions has been investigated by Raman spectroscopy and electronic transport experiments. The diazonium ions are expected to covalently bond to the graphene lattice, thus creating defects. However, in the addition to the creation of defects the diazonium moieties oriented perpendicular to the graphene lattice also has a non-negligible doping effect. In chapter 4 it has been shown how sensitive the transport properties of graphene are towards any external doping and how important it is to develop methods to control this doping in order to be able to do a quantitative analysis of the doping induced by the desired chemical reaction. In this thesis a method to reach a "clean" starting point for the functionalization process where the samples are repeatedly cleaned in isopropanol followed by heating has been developed. With this process we didn't only achieve a good starting point for the functionalization procedure, we also reproducible obtained good quality graphene devices on SiO_2 substrate with mobilities above 10 000 cm^2/Vs.

The method developed in chapter 4 to avoid doping effects from the solvents used in the chemical reaction is implemented in chapter 5 where Hall bars are functionalized and thoroughly investigated. For the here functionlized Hall bars surprisingly few defects were

introduced to the graphene lattice and the main effect of the functionlization was doping. We speculate that a polymerization reaction is observed where only a few diazonium moieties are attached to the graphene lattice in the first functionlization steps and that these later acts as seeds for further polymerization.

There are several possible reasons for the low reactivity of graphene. In a previous Raman study of unprocessed graphene flakes that were functionalized by the same methods as described in this thesis a much higher reactivity of the graphene towards the diazonium chemistry was observed [45]. By contacting and patterning graphene structures the graphene lattice might loose some of its flexibility compared to an unpatterend flake and thus the reactivity is lowered.

In addition, processing the graphene flakes into nanostructures involves at least to electron beam lithography steps, thus the graphene is at least twice covered with resist. It is well known that removing such resist completely is not trivial. By conventional methods involving organic solvents there will most likely always be resist residues left on the devices. As a result only a limited amount of the graphene surface is accessible for chemical modification. Currently we believe this is the main reason for the low reactivity observed in this study.

In order to utilize chemical functionalization as an alternative to reactive ion etching for the patterning of nanostructures, the amount of defects induced to the graphene lattice has to be significantly increased. For this it would be desirable to have the cleanest possible graphene as a starting point. Furthermore, since graphene is highly hydrophobic there are studies showing that the addition of a surfactant to the reaction increases the reactivity of graphene significantly [11, 54].

Indeed, for all possible applications of chemistry that are interesting for electronic transport in graphene nanostructures, such as specific edge functionalization and band gap engineering, it is crucial to have a surface that is as clean as possible such that the reactive species have access to the complete graphene lattice. Otherwise the chemical reactions cannot be sufficiently controlled.

Graphene three-terminal junctions

In the search for fast electronic components, ballistic nanodevices with non-linear electrical properties have been developed. A typical example of such nanodevices are three-terminal junctions [64, 67]. Previous three-terminal junctions were fabricated only in n-type materials. For three-terminal junctions based on p-type materials similar non-linear electronic properties as for n-type junctions are expected, just with the opposite sign. In chapter 6 of this thesis we present the first realization of a three-terminal junction in graphene. In the non-linear transport regime intrinsic voltage rectification up to room temperature is observed. As expected, by tuning the device from hole transport to electron transport the sign of the rectified voltage is changed.

In this thesis we have presented a very simple model to explain the observed rectification. Basically the rectification can be understood as a direct result of the energy dependence of conductance. In other words the three-terminal junction works as a simple voltage divider where the resistances of the left and the right terminal are energy depen-

dent, thus producing a non-zero voltage at the center terminal. This model qualitatively explain the measurements presented here, however, it might be insufficient for a more detailed quantitative understanding of the rectification.

Although we could present tunable voltage rectification in a diffusive three-terminal junction for the first time, the efficiency of the rectification was only a few percent. Based on our simple model we propose to increase the rectification by making smaller devices where a transport gap is opened and operate the device partly in the gap and partly outside. However, it is not clear how the disorder related to such a transport gap will influence the rectification properties. Furthermore, our model suggests that increasing the mobility will not increase the efficiency of the rectification. This needs to be confirmed by future measurements.

Graphene quantum dots

Graphene single electron transistors and quantum dots have been extensively studied for a couple of years already [105, 106, 108–113, 118–120, 107, 121] and are thus already well understood. Still, there are open questions concerning the very detailed energy spectra and detailed interaction between dot states and lead states.

In part III of this thesis transport measurement of a three terminal dot are presented. For conventional measurement of the transport through a two-terminal dot the conductance is given by an interplay of the tunnel couplings of the dot to each lead, however the contribution from each single lead cannot be determined. With a three-terminal dot exactly such information can be obtained. The individual tunnel barriers between the dot and the different leads can be studied and properties of the individual leads can be probed. In this thesis we could not reach the single level transport regime and thus not investigate the individual coupling strengths between the dot and each lead. Still, by investigating the individual conductances of the different leads an indication about the different coupling strengths is obtained. Furthermore we exploit the multilevel regime to for the first time directly probe the coupling of different leads to different dot states. As an important result we could conclude that the graphene dot is a single well confined dot and not consisting of several puddles.

In chapter 9 finite bias spectroscopy measurements were performed. A rich spectrum of features were observed outside and to some extent inside Coulomb diamonds. Even though the three-terminal structure offers more information about the origin of these features than a conventional two-terminal dot, it was not possible to confirm the specific origin.

The main problems that we encountered during these experiments were the lack of tunability of the tunnel barriers created by the etched narrow constrictions and the strong modulation of transport due to resonances in the leads. As a result it was very difficult to find a good measurement regime. For most gate voltage configurations the current is completely suppressed in one of the three leads and the dot is effectively a two-terminal dot.

During the last part of this thesis a lot of effort was made to create smaller three-terminal quantum dots that would allow for single-level transport. However, even when managing to get to the single level regime it would be very difficult to study the develop-

ment of the tunneling couplings over more than four consecutive Coulomb peaks due to the problems described above. Therefore we also tried to open the leads in order to have more equal conductances from the dot to the different leads. The hope was to measure current in all three leads over large gate-voltage ranges. However, making the leads wider only increased the overall conductance, the regions of three-terminal dot behaviour did not increase. In addition the combination of decreasing the dot size and increasing the width of the leads led to poorly defined dot.

Final remarks

In this thesis transport experiments have been performed on a variety of different graphene nanostructures. The graphene flakes, exfoliated from natural graphite, are deposited on a Si/SiO_2 substrate and the nanostructures are patterned by reactive ion etching which has been the state of the art technology up to now. During the last couple of years the limits to this technology has become more and more evident. The bulk disorder induced to the graphene lattice due to the SiO_2 substrate has been limiting the charge carrier mobilities to below 20 000 cm^2/Vs. Therefore a lot of effort has made to avoid the SiO_2 substrate. By etching away the SiO_2 and suspending the devices mobilities up to 200 000 cm^2/Vs were observed for single layer at room temperature [122, 15]. Even though suspended devices allowed for the first measurements of the fractional quantum Hall effect [123, 124], these devices are fragile, difficult to gate and more complicated structures than ribbons can hardly be made. The latter problem has to some extent been solved by a suspending technique where graphene were deposited on top of a polymer stack which were later removed [125] However, in general the suspension of graphene structures has not proved itself as a adequate alternative to graphene on SiO_2.

Therefore it caused great excitement in the graphene community when recently researchers from Columbia University presented transport measurements of graphene on a hexagonal boron nitrate (h-BN) substrate with mobilities of 80 000 cm^2/Vs [126]. With this technique clean high-mobility graphene devices are obtained without sacrificing the stability of the devices. Clean high mobility graphene on h-BN would therefore be a good starting point for both further functionalization experiments and for all kind of graphene nanostructures.

For etched graphene nanostructures bulk disorder is not the only factor degrading the quality of the devices. Edge disorder might be limiting the quality even more. Therefore it would be desirable to reduce the influence of the edges. One promising approach is to create gate defined devices on bilayer graphene. For bilayer graphene on a SiO_2 substrate the bulk disorder limit the complete pinch off of the current, however, previous this year Coulomb blockade was demonstrated in gate defined quantum dots in high-quality suspended bilayer graphene [127]. Thus, it is expected that it should also be possible to create gate defined structures in bilayer graphene using h-BN as a substrate.

One could also imagine to develop devices with perfect edges. Unzipping carbon nanotubes is one possible method, however, the shape of the devices are then limited to ribbons. Another possibility would be to grow perfect structures starting from molecular precursors [128].

It is still not clear which of these technological approaches that will be the most suc-

cessful. Perhaps even something completely new has to be developed. However, the large interdisciplinary community working with graphene will for sure provide further developments during the next couple of years.

Appendices

A Characterization

As already discussed in chapter 3 there are mainly three techniques that are used to characterize graphene flakes. These are optical microscopy, Raman spectroscopy and scanning force micrography (SFM). In Fig A.1 a graphene flake with parts of different thicknesses are investigated by these three methods. In (a) a light microscopy image of the flake can be seen (a green filter is used to enhance the contrast [129]). Three regions corresponding to a thickness of 2, 3 and 4 layers can be identified. This is emphasized by the intensity profile shown in (b) (corresponding to the dashed in (a)) displaying clear steps when the number of layers are changing. A SFM image of the image with a corresponding height profile is shown in (c) and (d) respectively. In (e) and (f) a 2D Raman map of the integrated G line intensity and a line scan of the G line intensity are depicted. And finally a Raman 2D map of the full width at half maximum (FWHM) of the 2D line with a corresponding line scan is shown in (g) and (d). All methods show clear differences between areas of different thicknesses and allow for a relative statement about the number of layers. However, which are the best methods to determine absolute number of layers? As already discussed in chapter 3 SFM is not suitable due to a large variation in the absolute height of the flakes caused by water or other absorbents underneath the flake and possible resist residues on top of the flake. In addition different SFM tips and further scanning conditions might lead to different absolute heights. In the following we will therefore only compare light microscopy and Raman spectroscopy as tools to determine the number of graphene layers.

In this study we have investigated 111 graphene regions (a flake typically has two regions which are only a few layers thick) where the majority has a thickness of 1 to 4 layers. We define the optical contrast C as [129]

$$C = \frac{I_{\text{substrate}} - I_{\text{flake}}}{I_{\text{substrate}}} \tag{11.1}$$

where I_{flake} is the reflected light in the presence of graphene and $I_{\text{substrate}}$ is the reflected light of the bare substrate. The optical microscope is calibrated by measuring the contrast of a known single layer flake and keeping all microscope parameters such as the filter, the light intensity and all software settings constant for all further measurement. It is crucial to have a calibrated microscope in order to do a quantitative analysis based on the optical contrast of the flakes.

In Fig. A.2 (a) the optical contrast of the investigated graphene regions are plotted.

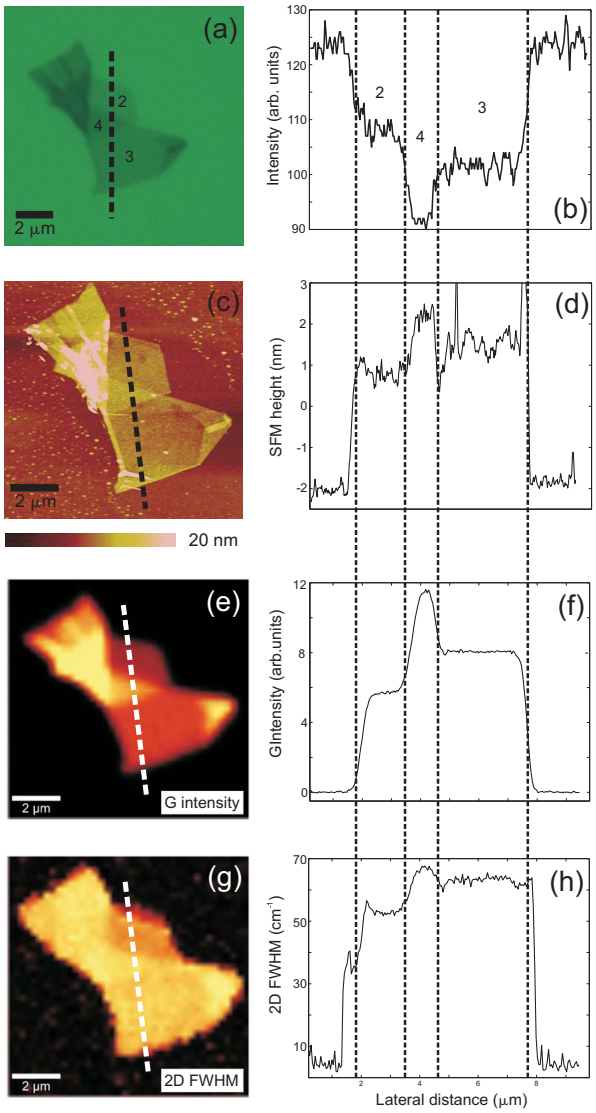

Fig. A.1 — (a) Light microscope image of a graphene flake with parts being 2, 3 and 4 layers thick as indicated. (b) Intensity profile corresponding to dashed line in (a). (c) SFM image of the same flake. (d) Height profile along the dashed line in (c). (e) Raman map showing the integrated intensity of the G line. (f) G line intensity along the dashed line in (e). (g) Raman map showing the full width at half maximum (FWHM) of the 2D line. (h) FWHM of the 2D line along the dashed line in (g).

Each region is given a number from 1 to 111 in order to later be able to compare the different measurement techniques. Clear quantized steps corresponding to 1, 2, 3, 4, and 5 layers can be identified. For more than 5 layers the statistic is not good enough to make a clear statement. In Fig.A.2 (b) the corresponding FWHM of the 2D peak from the Raman spectroscopy analysis is plotted. The FWHM of the 2D line of single layer graphene varies between 29 and 37 cm^{-1} and is clearly distinguishable from flakes with more layers. The FWHM of the 2D of bilayer graphene varies 54 and 60 cm^{-1} and is

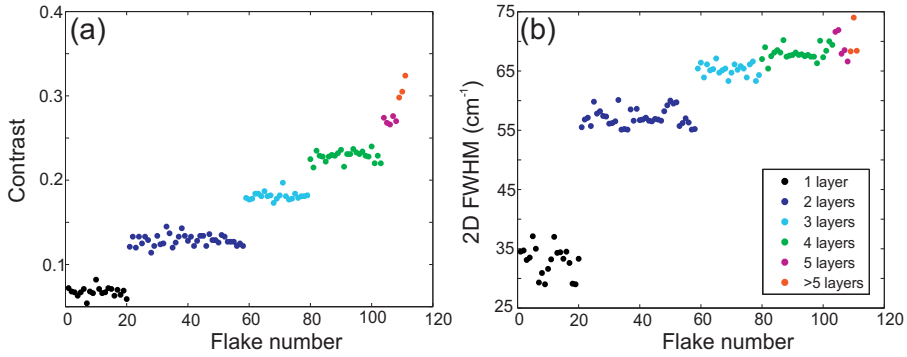

Fig. A.2 — (a) The optical contrast of 116 flakes plotted for an increasing number of layers. (b) Corresponding plot of the FWHM of the 2D line from Raman spectroscopy measurements.

also distinguishable from flakes with more layers. For more than two layers a general continuous increase of the FWHM of the 2D peak can be seen, however, the number of layers cannot be unambiguously determined anymore. Thus, Raman spectroscopy is a suitable tool to identify single and bilayer graphene (and is in many cases the preferred tool since no calibration is needed), however, if one wants to identify graphene flakes with 3 or more layers optical contrast should be used.

In the following we complete this characterization study of graphene by looking at different additional Raman spectroscopy parameters that are also used as indications of the number of layers. In Fig. A.3(a) the ratio of the integrated intensities of the G and the 2D line I_G/I_{2D} is plotted as a function of flake number. As expected an almost linear increase of I_G/I_{2D} can be seen for an increasing number of layers [40]. Since the intensity of the 2D line changes only slightly the observed change is attributed to the change in the intensity of the G line (see also Fig. A.1) [40]. The 2D peak position is expected to shift to higher wave numbers for an increasing number of layers [130]. This general tendency is confirmed in Fig. A.3. In Fig. A.3 (c) we plot the G peak position as a function of flake number. Previously it has been reported that a shift of about $4\,\mathrm{cm}^{-1}$ to lower wave numbers is observed between single and bilayer graphene and for a further increase of the number of layers the G peak position hardly changes anymore [40, 39]. This is consistent with the measurement of the G peak position as a function of flake number shown here in Fig. A.3(c). However, it should be noted that the G peak position is very sensitive to doping, as emphasized by the large scattering of peak positions for the single layer flakes, and thus not reliable for determining the number of layers [48, 47, 40].

As explained in chapter 3 the 2D peak of single layer graphene can be modeled with a single Lorentzian peak, the bilayer 2D peak is a convolution of 4 Lorentzian peakes, while all other thicknesses can be modeled with 2 Lorentzian peaks. For two and more layers we therefore plot the distance between the inner two Lorentzain peaks $2D_{A1}$ and $2D_{A2}$ [39] as a function of flake number. As expected the distance increases for increasing number of layers [130, 40] and bilayer flakes are clearly distinguishable from flakes with more than two layers.

In summary it has been shown that the FWHM of the 2D peak from Raman spec-

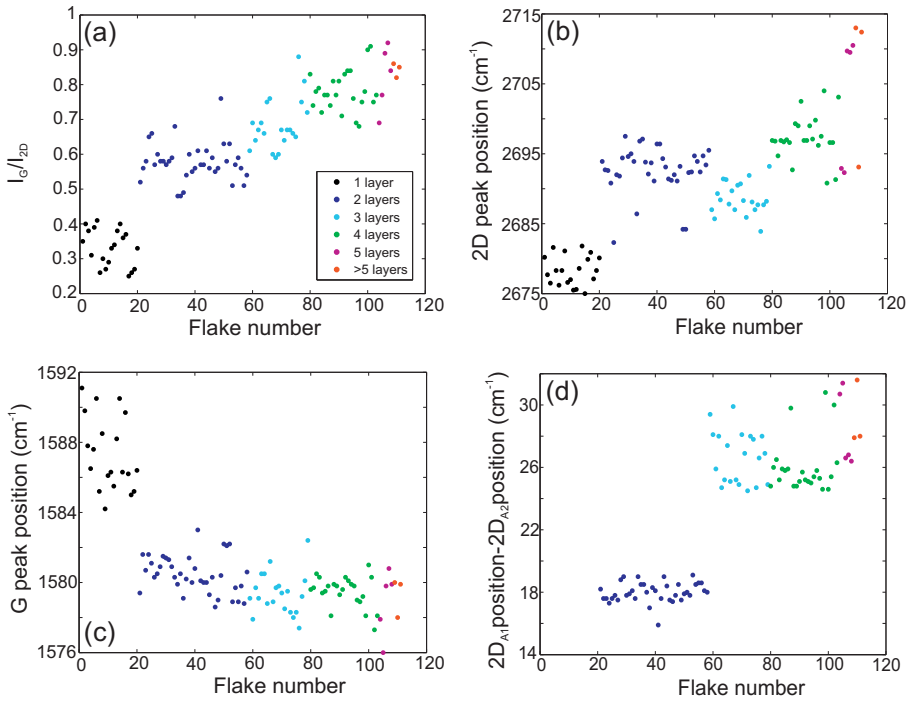

Fig. A.3 — (a) I_G/I_{2D} plotted for an increasing number of layers. (b)-(d) Corresponding plots of the 2D peak position, the G peak position and the difference between the $2D_{A1}$ and the $2D_{A2}$ peak positions respectively.

troscopy can be used to unambiguously identify single and bilayer graphene. However, to determine the number of layers for flakes with more than two layers optical contrast has to be used. And the optical microscope used for such an analysis has to be carefully calibrated. The intensity ratio of the G and the 2D line, the 2D peak position and the G-peak position follows the trends expected from previous experiments and to some extent these parameters can be used to identify single layer graphene, however, for more than 1 layer no clear statement can be made. Finally, bilayer graphene can be well identified by the relative distance between the two inner peaks of the four peaks creating adding up to the 2D peak.

B List of samples

name	picture	device info	measurement
F7	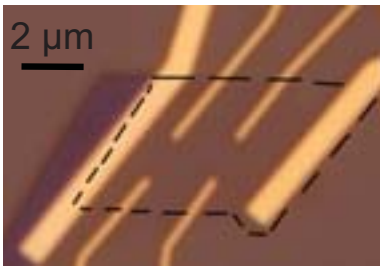	Single layer flake Unpatterend W_{flake}=2.5 μm L_{flake}=6 μm	First functionalization experiments Chapter 4
F25	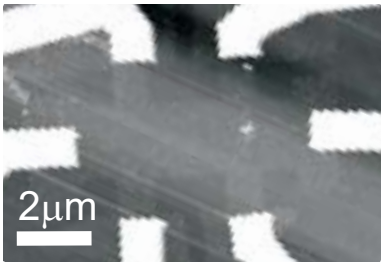	Single layer flake Hall bar structure W=2 μm L=3 μm	How clean can it get? Chapter 4
F51	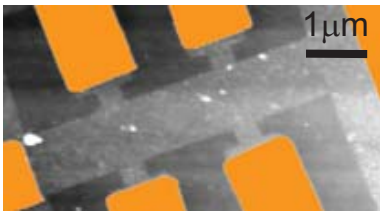	Single layer flake Hall bar structure W=1 μm L=2 μm	Isopropanol influence Chapter 4
F70	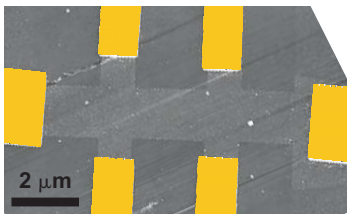	Single layer flake Hall bar structure W=0.5 μm L=3 μm	Functionalization Chapter 5

name	picture	device info	measurement
AJ54	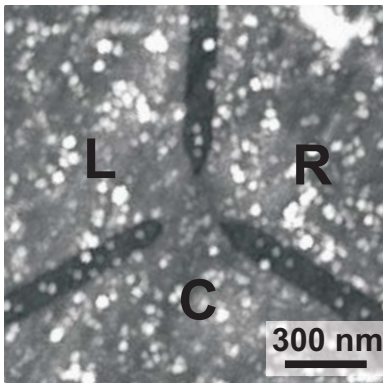	Single layer flake Three terminal junction $W_{constr.}$=200 nm	Tunable voltage rectification Chapter 6 Universal conductance fluctuations Weak localization Disorder potential Chapter 7
AJ87	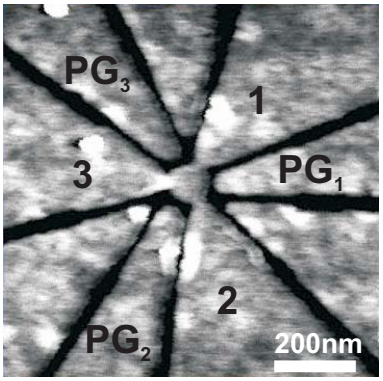	Single layer flake Three terminal dot D_{dot}=110 nm $W_{constr.}$=40 nm	Energy dependence of Coulomb peak positions Chapter 8 Finite bias spectroscopy Chapter 7

C Processing of graphene samples on SiO_2

Process		Description of process steps
Photolithography on wafer (bond pads and markers)	1. HMDS Coating	(a) 2-5 droplets on paper in glassware (not on glass) (b) Put wafer (oxide facing up) on a glass grid in the glassware.
	2. Spinning	(a) Resist: ma-N 1405 (cover at least 1/3 of the wafer) (b) 3000 rpm/2/40 s (c) soft bake: 100°C for 60 s
	3. Exposure	(a) MA6 maskaligner, channel 1 (365 nm). If problem use CP (b) Lamp test with correct sensor (365 nm) (c) Intensity 350 mJ/cm^2 (around 50-70 s)
	4. Development	(a) ma-D 533s, 60-70 s gentle agilitating (b) Rinse in water (2 min, frequently tilting sidewards to exchange water)
Evaporation wafer	1. Plasma asher	30 s at 200 W
	2. Metal evaporation	5 nm Ti (or Cr), 45 nm Au.
	3. Lift off	Leave around 10 min in 50°C acetone. Blow the gold off using a pipette or ultrasound (up to power 9).
	4. Clean wafer	(a) 2 min in acetone at US power 9. (b) 2 min in isopropanol at US power 9. (c) Blow dry with N_2.
Dicing wafer	1. Protecting resist	Spin Shiplez 1805 60 s with 5000 rpm. Hard bake 2 min at 115°C.
	2. Dicing	7.1 x7.1 mm^2 chips
Graphene deposition	1. Clean chips (x2)	(a) 2 min in acetone at US power 9. (b) 2 min in isopropanol at US power 9. (c) Blow dry with N_2.
	2. Graphene exfoliation (in Grey room)	(a) Cut pieces of blue or scotch tape (b) Press a large piece of graphite gently onto the tape and remove it. Fold the tape 2-3 times. Press a new tape gently onto the old tape and exfoliate. Fold the new tape 2-3 times. Continue the folding and changing of tape until there is a thin homogenious layer of graphite across the tape. Press a chip gently onto the tape (from the top)
	3. Clean chips	(a) Short US pulse (power 1) in acetone to remove flakes that does not stick well. (b) Leave the chips in acetone at 50°C for at least 30 min to remove glue remainings (no more US). (c) 2 min isopropanol. (d) Blow dry with N_2.
Making contacts	1. Clean samples	(a) 2 min in acetone. (b) 2 min in isopropanol. (c) Blow dry with N_2
	2. Spinner	(a) Soft bake 2 min at 120°C. (b) PMMA 50K CB 4% (pure), 1000 rpm/1/1 s, 5000 rpm/4/45,s. Bake 5 min at 180°C. (c) PMMA 950K 1:1 EL, 1000 rpm/1/1 s, 5000 rpm/4/45,s. Bake 5 min at 180°C.
	3. EBL	
	4. Development	(a) MIBK:IPA 1:3, 60 s (no stirring). (b) Isopropanol, 60 s (slow stirring the last 15 s). (c) Blow dry with N_2.
	5. Metal evaporation	5 nm Ti (or Cr), 40 nm Au.
	6. Lift off	(a) Leave in 50°C acetone for about 10 min. (b) Blow with a pipette to remove the gold. If parts of the gold cannot be removed by the pipette, use US for some min (up to power 6 with, tissue under the glass, 40 kHz).

Etching	1. Clean samples	(a) 2 min in acetone. (b) 2 min in isopropanol. (c) Blow dry with N_2
	2. Spinner	(a) Soft bake 2 min at 120°C. (b1) Multilayer etch: PMMA 950K 1:1 CB. 2000 rpm/2/2 s,5000 rpm/4/45 s. Bake 5 min at 180°C. (b2) SPL etch: PMMA 950K 2:5 CB. 2000 rpm/2/2 s, 6000 rpm/4/45 s. Bake 5 min at 180°C.
	3. EBL	
	4. Development	(a) MIBK:IPA 1:3, 60 s (no stirring). (b) Isopropanol, 60 s (slow stirring the last 15 s). (c) Blow dry with N_2.
	5. Etching RIE80	(a) Clean. Recipe: Graphene clean (b1) Etching multilayer: Recipe: "graphene etch thick" (b2) Etching SPL: Recipe: "graphene etch thin"
Clue sample to chip carrier	1. Mix conductive glue	H20E A + B (1:1).
	2. Glue sample to chip carrier	Place a small droplet of glue in the middle of the carrier. Press the chip gently into the carrier. Leave place to bond the backgate at one end of the carrier. Put an droplet of glue between the side of the chip and the bottom of the carrier (to be sure that the backgate is contacted.)
	3. Bake	15 min at 150°C in vacuum.

Bibliography

[1] A. K. Geim and K. S. Novoselov, Nature materials **6**, 183 (2007), ISSN 1476-1122.

[2] K. S. Novoselov, A. K. Geim, S. V. Morozov, D. Jiang, Y. Zhang, S. V. Dubonos, I. V. Grigorieva, and A. A. Firsov, Science (New York, N.Y.) **306**, 666 (2004), ISSN 1095-9203.

[3] C. Lee, X. Wei, J. W. Kysar, and J. Hone, Science (New York, N.Y.) **321**, 385 (2008), ISSN 1095-9203.

[4] A. K. Geim, Science (New York, N.Y.) **324**, 1530 (2009), ISSN 1095-9203.

[5] J. S. Bunch, S. S. Verbridge, J. S. Alden, A. M. V. D. Zande, J. M. Parpia, H. G. Craighead, and P. L. Mceuen, Nano letters **8**, 2458 (2008).

[6] R. R. Nair, P. Blake, A. N. Grigorenko, K. S. Novoselov, T. J. Booth, T. Stauber, N. M. R. Peres, and A. K. Geim, Science (New York, N.Y.) **320**, 1308 (2008), ISSN 1095-9203.

[7] F. Bonaccorso, Z. Sun, T. Hasan, and A. C. Ferrari, Nature Photonics **4**, 611 (2010), ISSN 1749-4885.

[8] Y. Zhu, S. Murali, M. D. Stoller, K. J. Ganesh, W. Cai, P. J. Ferreira, A. Pirkle, R. M. Wallace, K. A. Cychosz, M. Thommes, et al., Science (New York, N.Y.) **332**, 1537 (2011), ISSN 1095-9203.

[9] R. Balog, B. Jø rgensen, L. Nilsson, M. Andersen, E. Rienks, M. Bianchi, M. Fanetti, E. Laegsgaard, A. Baraldi, S. Lizzit, et al., Nature materials **9**, 315 (2010), ISSN 1476-1122.

[10] K. P. Loh, Q. Bao, P. K. Ang, and J. Yang, Journal of Materials Chemistry **20**, 2277 (2010), ISSN 0959-9428.

[11] R. Sharma, J. H. Baik, C. J. Perera, and M. S. Strano, Nano letters **10**, 398 (2010), ISSN 1530-6992.

[12] X. Hong, S.-H. Cheng, C. Herding, and J. Zhu, Physical Review B **83** (2011), ISSN 1098-0121.

[13] F. Withers, M. Dubois, and A. Savchenko, Physical Review B **82**, 1 (2010), ISSN 1098-0121.

[14] J. Moser, H. Tao, S. Roche, F. Alzina, C. M. Sotomayor Torres, and A. Bachtold, Physical Review B **81**, 2 (2010), ISSN 1098-0121.

[15] K. Bolotin, K. Sikes, Z. Jiang, M. Klima, G. Fudenberg, J. Hone, P. Kim, and H. Stormer, Solid State Communications **146**, 351 (2008), ISSN 00381098.

[16] A. H. Castro Neto, N. M. R. Peres, K. S. Novoselov, and A. K. Geim, Reviews of Modern Physics **81**, 109 (2009), ISSN 0034-6861.

[17] P. R. Wallace, Physical Review **71**, 622 (1947).

[18] T. Ihn, J. Güttinger, F. Molitor, S. Schnez, E. Schurtenberger, A. Jacobsen, S. Hellmüller, T. Frey, S. Dröscher, and C. Stampfer, Materials Today **13**, 44 (2010), ISSN 13697021.

[19] K. S. Novoselov, A. K. Geim, S. V. Morozov, D. Jiang, M. I. Katsnelson, I. V. Grigorieva, S. V. Dubonos, and A. A. Firsov, Nature **438**, 197 (2005), ISSN 1476-4687.

[20] M. I. Katsnelson, K. S. Novoselov, and A. K. Geim, Nature Physics **2**, 620 (2006), ISSN 1745-2473.

[21] T. Ando and T. Nakanishi, Journal of the Physical Society of Japan **67**, 1704 (1998).

[22] N. Stander, B. Huard, and D. Goldhaber-Gordon, Physical Review Letters **102**, 1 (2009), ISSN 0031-9007.

[23] A. F. Young and P. Kim, Nature Physics **5**, 222 (2009), ISSN 1745-2473.

[24] T. Ando, Journal of the Physics Society Japan **75**, 074716 (2006), ISSN 0031-9015.

[25] J.-H. Chen, C. Jang, S. Adam, M. S. Fuhrer, E. D. Williams, and M. Ishigami, Nature Physics **4**, 377 (2008), ISSN 1745-2473.

[26] J.-H. Chen, C. Jang, M. Ishigami, S. Xiao, W. Cullen, E. Williams, and M. Fuhrer, Solid State Communications **149**, 1080 (2009), ISSN 00381098.

[27] J.-H. Chen, W. Cullen, C. Jang, M. Fuhrer, and E. Williams, Physical Review Letters **102**, 1 (2009), ISSN 0031-9007.

[28] S. Datta, *Electronic transport in mesoscopic systems* (Cambridge University Press, 1995), 1st ed.

[29] Y. Zhang, Y.-W. Tan, H. L. Stormer, and P. Kim, Nature **438**, 201 (2005), ISSN 1476-4687.

[30] T. Ihn, *Semiconductor Nanostructures*, vol. 35 (Oxford Universtiy Press, 2010), 1st ed.

[31] L. E. O. P. Kouwenhoven, C. M. Marcus, P. L. Mceuen, S. Tarucha, and M. Robert, in *Mesoscopic Electron Tranpsort* (Springer, 1997), Kluwer, pp. 105–214.

[32] M. S. Dresselhaus and G. Dresselhaus, Advances in Physics **30**, 139 (1981).

[33] H. Shioyama, Journal of Materials Science Letters **20**, 499 (2001).

[34] L. M. Viculis, J. J. Mack, and R. B. Kaner, Science **299**, 90095 (2003).

[35] Y. Zhang, J. P. Small, W. V. Pontius, and P. Kim, Applied Physics Letters **86**, 073104 (2005), ISSN 00036951.

[36] X. Lu, M. Yu, H. Huang, and R. S. Ruoff, Nanotechnology **10**, 269 (1999).

[37] A. Luican, G. Li, and E. Andrei, Physical Review B **83**, 1 (2011), ISSN 1098-0121.

[38] L. Malard, M. Pimenta, G. Dresselhaus, and M. Dresselhaus, Physics Reports **473**, 51 (2009), ISSN 03701573.

[39] A. C. Ferrari, J. C. Meyer, V. Scardaci, C. Casiraghi, M. Lazzeri, F. Mauri, S. Piscanec, D. Jiang, K. S. Novoselov, S. Roth, et al., Physical Review Letters **97**, 1 (2006), ISSN 0031-9007.

[40] D. Graf, F. Molitor, K. Ensslin, C. Stampfer, A. Jungen, C. Hierold, and L. Wirtz, Nano letters **7**, 238 (2007), ISSN 1530-6984.

[41] J. Maultzsch, S. Reich, and C. Thomsen, Physical Review B **70**, 1 (2004), ISSN 1098-0121.

[42] L. G. Cancado, K. Takai, T. Enoki, M. Endo, Y. a. Kim, H. Mizusaki, a. Jorio, L. N. Coelho, R. Magalhaes-Paniago, and M. a. Pimenta, Applied Physics Letters **88**, 163106 (2006), ISSN 00036951.

[43] D. C. Elias, R. R. Nair, T. M. G. Mohiuddin, S. V. Morozov, P. Blake, M. P. Halsall, A. C. Ferrari, D. W. Boukhvalov, M. I. Katsnelson, A. K. Geim, et al., Science (New York, N.Y.) **323**, 610 (2009), ISSN 1095-9203.

[44] M. Lucchese, F. Stavale, E. M. Ferreira, C. Vilani, M. Moutinho, R. B. Capaz, C. Achete, and A. Jorio, Carbon **48**, 1592 (2010), ISSN 00086223.

[45] F. M. Koehler, A. Jacobsen, K. Ensslin, C. Stampfer, and W. J. Stark, Small (Weinheim an der Bergstrasse, Germany) **6**, 1125 (2010), ISSN 1613-6829.

[46] L. G. Cançado, A. Jorio, E. H. M. Ferreira, F. Stavale, C. A. Achete, R. B. Capaz, M. Moutinho, A. Lombardo, T. S. Kulmala, and A. C. Ferrari, Nano letters **11**, 3190 (2011), ISSN 1530-6992.

[47] C. Casiraghi, S. Pisana, K. S. Novoselov, A. K. Geim, and A. C. Ferrari, Applied Physics Letters **91**, 233108 (2007), ISSN 00036951.

[48] C. Stampfer, F. Molitor, D. Graf, K. Ensslin, A. Jungen, C. Hierold, and L. Wirtz, Applied Physics Letters **91**, 241907 (2007), ISSN 00036951.

[49] Y.-c. Liu and R. L. Mccreery, Journal of the American Chemical Society **117**, 11254 (1995).

[50] M. Delamar, R. Hitmi, J. Pinson, and J. M. Saveant, Journal of the American Chemical Society **114**, 5883 (1992).

[51] J. L. Bahr, J. Yang, D. V. Kosynkin, M. J. Bronikowski, R. E. Smalley, and J. M. Tour, Journal of the American Chemical Society **123**, 6536 (2001), ISSN 0002-7863.

[52] B. K. Price, J. L. Hudson, and J. M. Tour, Journal of the American Chemical Society **127**, 14867 (2005), ISSN 0002-7863.

[53] E. Bekyarova, M. E. Itkis, P. Ramesh, C. Berger, M. Sprinkle, W. A. de Heer, and R. C. Haddon, Journal of the American Chemical Society **131**, 1336 (2009), ISSN 1520-5126.

[54] H. Zhang, E. Bekyarova, J.-W. Huang, Z. Zhao, W. Bao, F. Wang, R. C. Haddon, and C. N. Lau, Nano letters **11**, 4047 (2011).

[55] D. B. Farmer, R. Golizadeh-Mojarad, V. Perebeinos, Y.-M. Lin, G. S. Tulevski, J. C. Tsang, and P. Avouris, Nano letters **9**, 388 (2009).

[56] F. M. Koehler, N. A. Luechinger, D. Ziegler, E. K. Athanassiou, R. N. Grass, A. Rossi, C. Hierold, A. Stemmer, and W. J. Stark, Angewandte Chemie (International ed. in English) **48**, 224 (2009), ISSN 1521-3773.

[57] E. Bekyarova, M. E. Itkis, P. Ramesh, and R. C. Haddon, physica status solidi (RRL) - Rapid Research Letters **3**, 184 (2009), ISSN 18626254.

[58] M. Z. Hossain, M. A. Walsh, and M. C. Hersam, Journal of the American Chemical Society **132**, 15399 (2010), ISSN 1520-5126.

[59] T. Ando, A. B. Fowler, and F. Stern, Reviews of Modern Physics **54**, 437 (1982).

[60] M. Monteverde, C. Ojeda-Aristizabal, R. Weil, K. Bennaceur, M. Ferrier, S. Guéron, C. Glattli, H. Bouchiat, J. N. Fuchs, and D. L. Maslov, Physical Review Letters **104**, 2 (2010), ISSN 0031-9007.

[61] E. Hwang and S. Das Sarma, Physical Review Letters **101**, 2 (2008), ISSN 0031-9007.

[62] X. Hong, K. Zou, and J. Zhu, Physical Review B **80**, 1 (2009), ISSN 1098-0121.

[63] E. H. Hwang and S. Das Sarma, Physical Review B **77**, 1 (2008), ISSN 1098-0121.

[64] H. Q. Xu, Applied Physics Letters **78**, 2064 (2001), ISSN 00036951.

[65] L. Worschech, H. Q. Xu, A. Forchel, and L. Samuelson, Applied Physics Letters **79**, 3287 (2001), ISSN 00036951.

[66] H. Q. Xu, Applied Physics Letters **80**, 853 (2002), ISSN 00036951.

[67] I. Shorubalko, H. Q. Xu, I. Maximov, P. Omling, L. Samuelson, and W. Seifert, Applied Physics Letters **79**, 1384 (2001), ISSN 00036951.

[68] I. Shorubalko, H. Q. Xu, P. Omling, and L. Samuelson, Applied Physics Letters **83**, 2369 (2003), ISSN 00036951.

[69] D. B. Suyatin, J. Sun, A. Fuhrer, D. Wallin, L. E. Fröberg, L. S. Karlsson, I. Maximov, L. R. Wallenberg, L. Samuelson, and H. Q. Xu, Nano letters **8**, 1100 (2008).

[70] C. Papadopoulos, A. Rakitin, J. Li, A. Vedeneev, and J. Xu, Physical review letters **85**, 3476 (2000), ISSN 1079-7114.

[71] I. Shorubalko, H. Q. Xu, I. Maximov, D. Nilsson, P. Omling, L. Samuelson, and W. Seifert, IEEE Electron Device Letters **23**, 377 (2002).

[72] H. Q. Xu, I. Shorubalko, D. Wallin, I. Maximov, P. Omling, L. Samuelson, and W. Seifert, IEEE Electron Device Letters **25**, 164 (2004).

[73] C. R. Müller, S. Member, L. Worschech, P. Höpfner, S. Höfling, and A. Forchel, IEEE Electron Device Letters **28**, 859 (2007).

[74] J. Sun, D. Wallin, I. Maximov, and H. Q. Xu, IEEE Electron Device Letters **29**, 540 (2008).

[75] S. Reitzenstein, L. Worschech, and A. Forchel, IEEE Electron Device Letters **25**, 462 (2004).

[76] B. Lau, D. Hartmann, L. Worschech, and A. Forchel, IEEE Electron Device Letters **53**, 1107 (2006).

[77] J. Mateos, B. G. Vasallo, D. Pardo, and T. Gonz, Nanotechnology **14**, 117 (2003).

[78] F. Schedin, A. K. Geim, S. V. Morozov, E. W. Hill, P. Blake, M. I. Katsnelson, and K. S. Novoselov, Nature materials **6**, 652 (2007), ISSN 1476-1122.

[79] W. J. Yu, U. J. Kim, B. R. Kang, I. H. Lee, E.-H. Lee, and Y. H. Lee, Nano Letters **9**, 1401 (2009), ISSN 1530-6984.

[80] D. A. Areshkin and C. T. White, Nano Letters **7**, 3253 (2007), ISSN 1530-6984.

[81] D. Csontos and H. Xu, Physical Review B **67**, 1 (2003), ISSN 0163-1829.

[82] J. Martin, N. Akerman, G. Ulbricht, T. Lohmann, J. H. Smet, K. von Klitzing, and A. Yacoby, Nature Physics **4**, 144 (2007), ISSN 1745-2473.

[83] C. W. J. Beenakker and H. V. Houten, Solid State Physics **44**, 1 (1991).

[84] S. V. Morozov, K. S. Novoselov, M. I. Katsnelson, F. Schedin, L. A. Ponomarenko, D. Jiang, and A. K. Geim, Physical Review Letters **97**, 7 (2006), ISSN 0031-9007.

[85] X. Wu, X. Li, Z. Song, C. Berger, and W. A. de Heer, Physical Review Letters **98**, 2 (2007), ISSN 0031-9007.

[86] F. V. Tikhonenko, D. W. Horsell, R. V. Gorbachev, and A. K. Savchenko, Physical Review Letters **100**, 8 (2008), ISSN 0031-9007.

[87] Y.-F. Chen, M.-H. Bae, C. Chialvo, T. Dirks, A. Bezryadin, and N. Mason, Journal of physics. Condensed matter : an Institute of Physics journal **22**, 205301 (2010), ISSN 1361-648X.

[88] C. Ojeda-Aristizabal, M. Monteverde, R. Weil, M. Ferrier, S. Guéron, and H. Bouchiat, Physical Review Letters **104**, 1 (2010), ISSN 0031-9007.

[89] E. McCann, K. Kechedzhi, V. I. Falko, H. Suzuura, T. Ando, and B. L. Altshuler, Physical Review Letters **97**, 14 (2006), ISSN 0031-9007.

[90] F. V. Tikhonenko, A. A. Kozikov, A. K. Savchenko, and R. V. Gorbachev, Physical Review Letters **103**, 1 (2009), ISSN 0031-9007.

[91] J. B. Miller, D. M. Zumbühl, C. M. Marcus, Y. B. Lyanda-Geller, D. Goldhaber-Gordon, K. Campman, and A. C. Gossard, Physical Review Letters **90**, 3 (2003), ISSN 0031-9007.

[92] J. Nitta and T. Koga, Journal of Superconductivity **16**, 689 (2003).

[93] N. Staley, C. Puls, and Y. Liu, Physical Review B **77**, 1 (2008), ISSN 1098-0121.

[94] P. A. Lee and A. D. Stone, Physical Review Letters **55**, 1622 (1985).

[95] P. A. Lee, A. D. Stone, and H. Fukuyama, Physical Review B **35**, 1039 (1987).

[96] V. Skákalová, A. Kaiser, J. Yoo, D. Obergfell, and S. Roth, Physical Review B **80**, 3 (2009), ISSN 1098-0121.

[97] S. Droscher, P. Roulleau, F. Molitor, P. Studerus, C. Stampfer, K. Ensslin, and T. Ihn, Applied Physics Letters **96**, 152104 (2010), ISSN 00036951.

[98] S. Dröscher, H. Knowles, Y. Meir, K. Ensslin, and T. Ihn, Physical Review B **84**, 1 (2011), ISSN 1098-0121.

[99] B. Trauzettel, D. V. Bulaev, D. Loss, and G. Burkard, Nature Physics **3**, 192 (2007), ISSN 1745-2473.

[100] M. Han, B. Özyilmaz, Y. Zhang, and P. Kim, Physical Review Letters **98**, 1 (2007), ISSN 0031-9007.

[101] Z. Chen, Y.-M. Lin, M. J. Rooks, and P. Avouris, Physica E: Low-dimensional Systems and Nanostructures **40**, 228 (2007), ISSN 13869477.

[102] C. Stampfer, J. Güttinger, S. Hellmüller, F. Molitor, K. Ensslin, and T. Ihn, Physical Review Letters **102**, 1 (2009), ISSN 0031-9007.

[103] F. Molitor, A. Jacobsen, C. Stampfer, J. Güttinger, T. Ihn, and K. Ensslin, Physical Review B **79**, 1 (2009), ISSN 1098-0121.

[104] M. Y. Han, J. C. Brant, and P. Kim, Physical Review Letters **104**, 2 (2010), ISSN 0031-9007.

[105] S. Schnez, F. Molitor, C. Stampfer, J. Guttinger, I. Shorubalko, T. Ihn, and K. Ensslin, Applied Physics Letters **94**, 012107 (2009), ISSN 00036951.

[106] F. Molitor, H. Knowles, S. Dröscher, U. Gasser, T. Choi, P. Roulleau, J. Güttinger, A. Jacobsen, C. Stampfer, K. Ensslin, et al., EPL (Europhysics Letters) **89**, 67005 (2010), ISSN 0295-5075.

[107] X. L. Liu, D. Hug, and L. M. K. Vandersypen, Nano letters **10**, 1623 (2010), ISSN 1530-6992.

[108] C. Volk, S. Fringes, B. Terrés, J. Dauber, S. Engels, S. Trellenkamp, and C. Stampfer, Nano letters **11**, 3581 (2011), ISSN 1530-6992.

[109] J. Güttinger, T. Frey, C. Stampfer, T. Ihn, and K. Ensslin, Physical Review Letters **105**, 1 (2010), ISSN 0031-9007.

[110] J. Güttinger, C. Stampfer, T. Frey, T. Ihn, and K. Ensslin, Physica Status Solidi (B) **246**, 2553 (2009), ISSN 03701972.

[111] C. Stampfer, E. Schurtenberger, F. Molitor, J. Güttinger, T. Ihn, and K. Ensslin, Nano letters **8**, 2378 (2008), ISSN 1530-6984.

[112] S. Schnez, J. Güttinger, M. Huefner, C. Stampfer, K. Ensslin, and T. Ihn, Physical Review B **82**, 1 (2010), ISSN 1098-0121.

[113] J. Güttinger, J. Seif, C. Stampfer, A. Capelli, K. Ensslin, and T. Ihn, Physical Review B **83**, 1 (2011), ISSN 1098-0121.

[114] R. Leturcq, D. Graf, T. Ihn, K. Ensslin, D. D. Driscoll, and A. C. Gossard, Europhysics Letters (EPL) **67**, 439 (2004), ISSN 0295-5075.

[115] Y. Meir, N. S. Wingreen, and P. A. Lee, Physical Review Letters **66**, 3048 (1991).

[116] P. Roulleau, S. Baer, T. Choi, F. Molitor, J. Güttinger, T. Müller, S. Dröscher, K. Ensslin, and T. Ihn, Nature communications **2**, 239 (2011), ISSN 2041-1723.

[117] J. Güttinger, C. Stampfer, T. Frey, T. Ihn, and K. Ensslin, Nanoscale research letters **6**, 253 (2011), ISSN 1556-276X.

[118] J. Guttinger, C. Stampfer, S. Hellmuller, F. Molitor, T. Ihn, and K. Ensslin, Applied Physics Letters **93**, 212102 (2008), ISSN 00036951.

[119] J. Güttinger, C. Stampfer, F. Libisch, T. Frey, J. Burgdörfer, T. Ihn, and K. Ensslin, Physical Review Letters **103**, 1 (2009), ISSN 0031-9007.

[120] F. Molitor, S. Droscher, J. Guttinger, A. Jacobsen, C. Stampfer, T. Ihn, and K. Ensslin, Applied Physics Letters **94**, 222107 (2009), ISSN 00036951.

[121] S. Fringes, C. Volk, C. Norda, B. Terrés, J. Dauber, S. Engels, S. Trellenkamp, and C. Stampfer, Physica Status Solidi (B) **248**, 2684 (2011), ISSN 03701972.

[122] X. Du, I. Skachko, A. Barker, and E. Y. Andrei, Nature nanotechnology **3**, 491 (2008), ISSN 1748-3395.

[123] X. Du, I. Skachko, F. Duerr, A. Luican, and E. Y. Andrei, Nature **462**, 192 (2009), ISSN 1476-4687.

[124] K. I. Bolotin, F. Ghahari, M. D. Shulman, H. L. Stormer, and P. Kim, Nature **462**, 196 (2009), ISSN 1476-4687.

[125] N. Tombros, A. Veligura, J. Junesch, J. Jasper van den Berg, P. J. Zomer, M. Wojtaszek, I. J. Vera Marun, H. T. Jonkman, and B. J. van Wees, Journal of Applied Physics **109**, 093702 (2011), ISSN 00218979.

[126] C. R. Dean, A. F. Young, I. Meric, C. Lee, L. Wang, S. Sorgenfrei, K. Watanabe, T. Taniguchi, P. Kim, K. L. Shepard, et al., Nature nanotechnology **5**, 722 (2010), ISSN 1748-3395.

[127] M. T. Allen, J. Martin, and A. Yacoby, arXiv:1202.0820v1 (2012).

[128] J. Cai, P. Ruffieux, R. Jaafar, M. Bieri, T. Braun, S. Blankenburg, R. Fasel, M. Muoth, A. P. Seitsonen, M. Saleh, et al., Nature **466**, 470 (2010), ISSN 1476-4687.

[129] P. Blake, E. W. Hill, A. H. Castro Neto, K. S. Novoselov, D. Jiang, R. Yang, T. J. Booth, and A. K. Geim, Applied Physics Letters **91**, 063124 (2007), ISSN 00036951.

[130] A. C. Ferrari, Solid State Communications **143**, 47 (2007), ISSN 00381098.

Publications

Chemical modification of graphene characterized by Raman and transport experiments
F. M. Koehler[1], *A. Jacobsen*[1], *T. Ihn, K. Ensslin and W. J. Stark*
To appear in Nanoscale

Transport in a three-terminal graphene quantum dot
A. Jacobsen, P. Simonet, K. Ensslin and T. Ihn
N. J. of Phys. **14**, 023052, (2012)

Transport in graphene nanostructures
C. Stampfer, S. Fringes, J. Güttinger, F. Molitor, C. Volk, B. Terres, J. Dauber, S. Engels, S. Schnez, A. Jacobsen, S. Dröscher, T. Ihn and K. Ensslin
Frontiers of Physics **6**, 271 (2011)

Electronic properties of graphene nanostructures
F. Molitor, J. Güttinger, C. Stampfer, S. Dröscher, A. Jacobsen, T. Ihn and K. Ensslin
Topical Review, J. Phys. C **23**, 243201 (2011)

Towards electron transport measurements in chemically modified graphene: The effect of a solvent
A. Jacobsen[1], *F. M. Koehler*[1], *W. J. Stark and K. Ensslin*
N. J. of Phys. **12**, 125007 (2010)

Rectification in three-terminal graphene junctions
A. Jacobsen, I. Shorubalko, L. Maag, U. Sennhauser and K. Ensslin
Appl. Phys. Lett. **97**, 032110 (2010)

Selective Chemical Modification of Graphene Surfaces: Distinction Between Single- and Bilayer Graphene
F. M. Koehler, A. Jacobsen, K. Ensslin, C. Stampfer and W. J. Stark
Small **6**, 1125 (2010)

[1]Both authors have contributed equally to this work.

The AharonovBohm effect in a side-gated graphene ring
M. Huefner, F. Molitor, *A. Jacobsen, A. Pioda, C. Stampfer, K. Ensslin and T. Ihn*
N. J. of Phys. **12**, 043054 (2010)

Observation of excited states in a graphene double quantum dot
F. Molitor, H. Knowles, S. Dröscher, U. Gasser, T. Choi, P. Roulleau, J. Güttinger, *A. Jacobsen, C. Stampfer, K. Ensslin and T. Ihn*
Europhys. Lett. **89**, 67005 (2010)

Graphene single-electron transistors
T. Ihn, J. Güttinger, F. Molitor, S. Schnez, E. Schurtenberger, *A. Jacobsen, S. Hellmüller, T. Frey, S. Dröscher, C. Stampfer and K. Ensslin*
Materials Today **13**, 44 (2010)

Energy and Transport Gaps in etched Graphene Nanoribbons
F. Molitor, C. Stampfer, J. Güttinger, *A. Jacobsen, T. Ihn and K. Ensslin*
Semicond. Sci. Technol. **25**, 034002 (2010)

Investigation of the Aharonov Bohm effect in a gated graphene ring
M. Heufner, F. Molitor, *A. Jacobsen, A. Pioda, C. Stampfer, K. Ensslin and T. Ihn*
Phys. Status Solidi **246**, 2756 (2009)

Transport through graphene double dots
F. Molitor, S. Dröscher, J. Güttinger, *A. Jacobsen, C. Stampfer, T. Ihn and K. Ensslin*
Appl. Phys. Lett. **94**, 222107 (2009)

Transport gap in side-gated graphene constrictions
F. Molitor, *A. Jacobsen, C. Stampfer, J. Güttinger, T. Ihn and K. Ensslin*
Phys. Rev. B **79**, 075426 (2009)

Acknowledgements

The work presented in this thesis would not have been possible without the help and support of many people.

First of all I would like to thank Klaus Ensslin for giving me the opportunity to do my PhD work in his group. His constant optimism, curiosity and interest in physics has been very inspiring and has continued to push me forward whenever I have felt stuck. In addition I am very grateful for all the support and goodwill during my pregnancy and after the birth of Henrik. Thanks a lot! I would also like to thank Thomas Ihn for all his support during this thesis. His great knowledge about details of measurement setups, measurement techniques, data analysis and of course his never ending patience has been extremely helpful. Many thanks also goes to Wendelin Stark for co-examining my thesis and for the nice collaboration about functionalization of graphene.

A very special thanks goes to Fabian Köhler with whom I shared all the functionalization experiments. Even though some of our procedures were cumbersome, it was a lot of fun to work with you. I also feel very lucky that I was given the opportunity to work together with Ivan Schorubalko who initiated the three-terminal junction project. A better collaborator and teacher is not easy to find.

I would also like to thank Paul Studerus and Cecil Barengo for their help in the lab. Their great knowledge about electronics and measurement setups and their innovative ideas were very important for the progress of new experiments. Without you this thesis would have taken twice the time. Also many thanks to Claudia Vinzens for making the administration run smoothly and for the nice chats in your office.

Furthermore, I would like to thank the FIRST staff for all their support with equipment and discussion about processing recipes. In addition I am grateful to the numerous of other FIRST users for help, fun and nice chats in the clean room.

I greatly enjoyed the time in the nanophysics group. During the years some people have left and new people have joined, however, the nice atmosphere has stayed the same. Thanks to everyone! Especially thank to the previous and present members of the graphene team, Françoise, Christoph, Johannes, Susanne, Dominik, Clément, Anastasia and Pauline, for sharing frustrations and break throughs in the graphene world. Additionally I would like to thank Theo, Sarah, Stefan, Simon (who continued to patiently answer my LabView questions also after he left the group), Bruno, Thomas and Miklos for always having time to answer a question. And particularly I want to thank Yashar, who has answered way more questions than anybody else and supported me from the beginning to the end of this thesis. Also a very special thanks to my two diploma students, Leo and Pauline, who

both contributed a lot to this work.

In order to enjoy four years of working in the lab, it is important to also have fun outside the lab. And I am really grateful to all my friends who has kept reminding me about this. Especially i want to thank Astrid-Sofie, Nora, Marte & Martin, Trygve & Leiry, Erik & Catalina, Christer and Knut & Hanna Maja for all the cabin trips. Hopefully they will continue until we are old and grey.

Finally, I would like to thank the people that never stop supporting me and believing in me, my family. Thanks to mamma, pappa, Kari and Bjørn Atle for always putting things into perspective. And most of all, thanks to Lukas for having shared all the ups and downs of thesis with me. I couldn't have done this without you! Til slutt: Takk Henrik, for at du er den du er.

Curriculum Vitae

Name:	Arnhild Jacobsen
born:	March 4, 1983 in Bergen (Norway) citizen of Norway

2000-2002	International Baccalaureate, Bergen Katedralskole, Norway
2002-2003	Elverum folkehøgskule, Elverum, Norway
2003-2008	Studies in physics at the Norwegian University of Science and Technology (NTNU), Trondheim, Norway
2006-2007	Exchange year, ERASMUS at the Swiss Federal Institute of Technology (ETH), Zürich, Switzerland
2008	Diploma thesis in the group of Prof. Klaus Ensslin at the Laboratory of Solid State Physics, ETH Zürich, Switzerland: "Transport in graphene nanostructures"
2008-2012	Ph. D in the group of Prof. Klaus Ensslin at the Laboratory of Solid State Physics, ETH Zürich, Switzerland